Challenge Journal of

CONCRETE RESEARCH LETTERS

Vol.16 No.4 (2025)

acoustic emission aerated concrete artificial neural network compressive strength corrosion cracking ductility durability energy absorption ferrocement flexural strength fly ash fracture mechanics mechanical properties mortar nanoparticle reinforced concrete self-compacting concrete steam curing strengthening superplasticizer tensile strength workability waste disposal water absorption

ISSN 2548-0928

TULPAR ACADEMIC PUBLISHING

Challenge Journal of Concrete Research Letters

E-mail: *cjcrl@challengejournal.com*

Web page: *cjcrl.challengejournal.com*

Tulpar Academic Publishing
www.tulparpublishing.com

Challenge Journal of Concrete Research Letters

CONTENTS

TULPAR ACADEMIC PUBLISHING

Challenge Journal of Concrete Research Letters

Research Article

Compressive strength and fire resistance of mortar containing spent garnet as partial sand replacement

Wee Phadee Wee Chit [a], Ahmed Mokhtar Albshir Budiea [a,*], Hamidun Mohd Noh [b], Khairunisa Muthusamy [a], Saleh Omar Bamaga [c]

[a] *Faculty of Civil Engineering Technology, Universiti Malaysia Pahang Al-Sultan Abdullah, 26300 Kuantan, Pahang, Malaysia*
[b] *Faculty of Technology Management and Business, Universiti Tun Hussein Onn Malaysia, 86400 Parit Raja, Batu Pahat, Johor, Malaysia*
[c] *Department of Civil Engineering, College of Engineering, University of Bisha, 61922 Bisha, Saudi Arabia*

ABSTRACT

The increasing demand for sand in construction, driven by rapid urbanization, has led to unsustainable sand mining and significant environmental degradation. This study addresses the urgent need for sustainable alternatives by investigating the use of spent garnet, a waste by-product from abrasive blasting, as a partial replacement for fine aggregate in mortar. Despite its widespread disposal in landfills, spent garnet has potential as a viable substitute due to its high bulk density and angular particle structure. This research explores the effects of substituting sand with spent garnet at 10%, 20%, 30%, and 40% replacement levels. The novelty of this study lies in its integrated evaluation of workability, mechanical strength, and thermal resistance of mortar incorporating spent garnet. Results from flow table tests showed a progressive increase in flowability, with the 40% garnet mix achieving a maximum flow of 142%, compared to 68.3% for the control mix. Density increased from 4958 kg/m^3 (0% garnet) to 5180 kg/m^3 (40% garnet), enhancing packing efficiency. The highest compressive strength was recorded in the 20% replacement mix, with values of 37.95 MPa at 7 days and 50.99 MPa at 28 days, an increase of 12.5% and 42.3%, respectively, over the control mix. Thermal analysis revealed the lowest mass loss in 10% and 20% replacement mixes, with the 20% mix also showing improved fire resistance. These findings indicate that a 20% spent garnet replacement offers the optimal balance between workability, mechanical performance, and thermal stability. This approach not only enhances mortar properties but also promotes sustainable waste management and reduces reliance on natural river sand.

ARTICLE INFO

Article history:
Received – April 9, 2025
Revision requested – May 6, 2025
Revision received – June 9, 2025
Accepted – June 24, 2025

Keywords:
Spent garnet
Sand replacement
Environmentally friendly mortar
Compressive strength
Fire resistance

Citation: Wee Chit WP, Budiea AMA, Mohd Noh H, Muthusamy K, Bamaga SO (2025). Compressive strength and fire resistance of mortar containing spent garnet as partial sand replacement. *Challenge Journal of Concrete Research Letters*, 16(4), 164–172.

1. Introduction

Construction has been one of the key industrial sectors driving economic growth and development in every country (Alaluo et al. 2021). While concrete is widely recognized as a fundamental building material, mortar–produced by blending cement, sand, and water also serves as a key component in building and infrastructure projects. As an adhesive substance, it fills gaps between units and is frequently used for plastering and joining building blocks. The increasing use of mortar in construction projects has led to higher consumption of river sand. According to Shitima and Suykens (2023), the rapid growth of urbanization has significantly increased the demand for sand. Allied Market Research reports that the construction aggregates industry, valued at $375.3 billion in 2021, is projected to grow to $621.1 billion by 2031, with a CAGR of 5.05% from 2022 to 2031

* *Corresponding author*. Tel.: +60-9-431-5014 ; E-mail address: ahmedbudieea@umpsa.edu.my (A. M. A. Budiea)
ISSN: 2548-0928 / DOI: https://doi.org/10.20528/cjcrl.2025.04.001

(Digvijay and Onkar 2022). Sand, a non-renewable resource, is the most mined material in the world due to its broad use in constructing roads, buildings, and infrastructure, as well as in industries such as glass manufacturing and nuclear energy (Whiting 2019; Ludacer 2018). Excessive sand mining, however, has caused significant environmental issues including riverbank erosion, freshwater contamination, damage to aquatic ecosystems, and riverbed alterations (Sherry and Philippe 2022; Dinh et al. 2022; Muellegger et al. 2013). To address these problems, it is important to consider alternative waste materials as substitutes for sand in construction.

One such material is spent garnet, an industrial by-product produced from abrasive blasting, water jet cutting, and water filtration processes. In industries such as ship maintenance and repair, spent garnet has limited reuse and is often discarded after a few cycles, resulting in substantial waste generation (Muttashar et al. 2018). This waste is typically sent to landfills, contributing to environmental pollution. The negative environmental impact of spent garnet disposal has been highlighted by researchers such as Mokhatar et al. (2022) and Jamaludin et al. (2022a). In support of sustainability, the use of processed spent garnet at suitable replacement levels has been shown to enhance the strength of concrete when used as a cement substitute (Jamaludin et al. 2024). Several studies have focused on using spent garnet as a sand replacement in concrete (Huseien et al. 2019; Muttashar et al. 2018; Muthusamy et al. 2022; Jaafar et al. 2024; Ruslan et al. 2024). However, limited studies have explored the application of spent garnet in mortar, especially in relation to its fire resistance and mechanical performance compared to its role in concrete.

This study investigates the performance of mortar blended with processed spent garnet as a sand replacement. The aim is to assess its suitability and effectiveness in promoting sustainable construction while reducing landfill waste and conserving natural sand. This research addresses the gap in existing studies, which have primarily focused on concrete, by emphasizing mortar-specific properties and behavior.

2. Methodology

This study used ordinary portland cement, river sand, spent garnet, and tap water to produce mortar samples. Spent garnet was collected from a sandblasting industry in West Malaysia, then oven-dried and sieved to remove debris. Six mortar mixes were prepared: one control mix (100% river sand) and five mixes with 10–40% spent garnet replacing sand. Materials were mixed in a clean tray, cast into greased cube molds in layers, compacted, and left to set overnight. After demolding, specimens were cured in water for 7 and 28 days.

2.1. Materials

This study used cement, sand, spent garnet, and water as the primary materials. Ordinary portland cement was used as the sole binder. Tap water was utilized for preparation of the mortar mix and the curing process. The fine aggregate used is river sand with fineness modulus and water absorption is 3.94 and 3.12 respectively. The particle size distribution and microstructure of sand is illustrated in Figs. 1 and 2 correspondingly. Spent garnet was collected from the sandblasting-related industry in West Malaysia and transported by lorry to the laboratory. Upon arrival, the gunny bags full of spent garnet were placed in a closed container. At the laboratory, the spent garnet waste was placed in the oven and dried for 24 hours to ensure it was in an oven-dry condition. Then, it was sieved through a 600 μm sieve to remove debris. Fig. 3 illustrates the spent garnet: (a) as received, freshly/ raw material of spent garnet waste, and (b) after the drying and sieving process. The fineness modulus and water absorption of spent garnet is 2.91 and 6.18 respectively. The particle size distribution of spent garnet and SEM microstructure is illustrated in Figs. 4 and 5. The chemical composition of spent garnet is tabulated in Table 1.

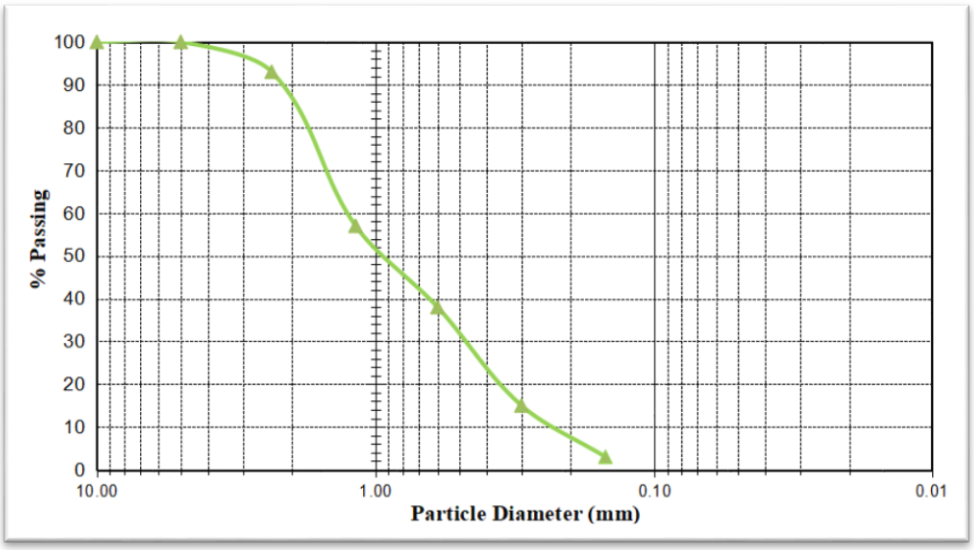

Fig. 1. Particle size distribution of sand.

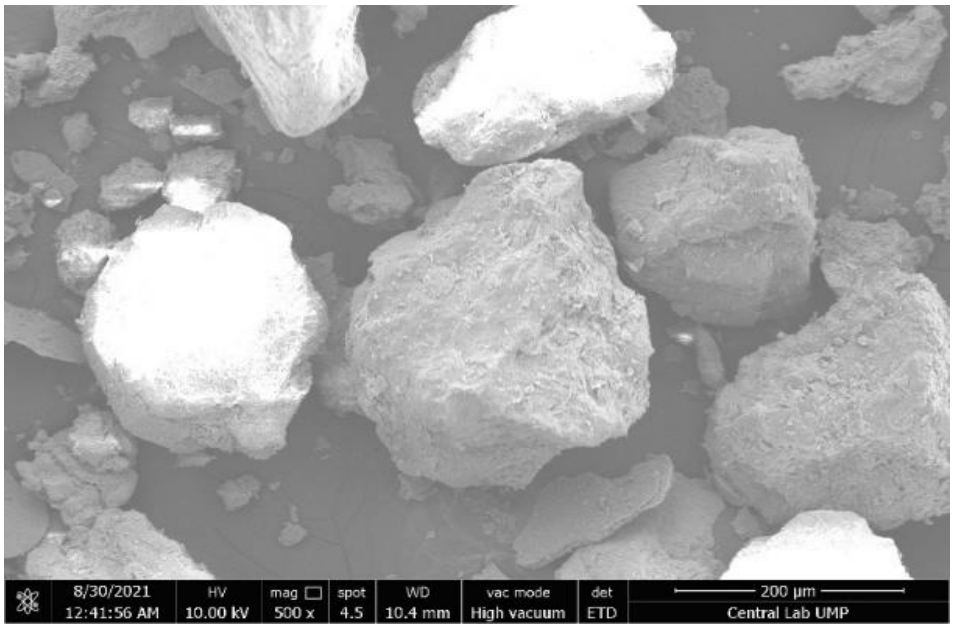

Fig. 2. Image of sand at magnification of 500x.

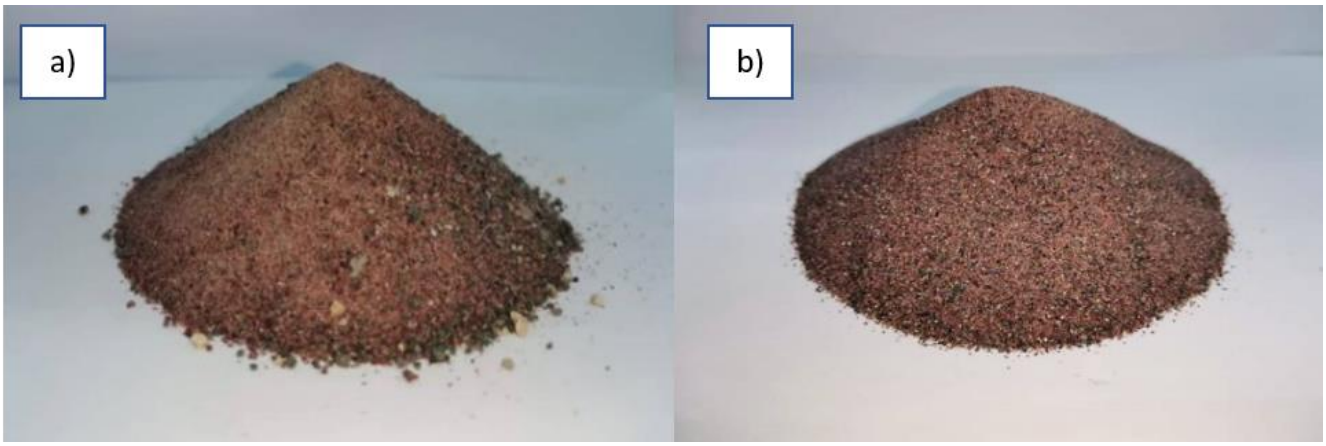

Fig. 3. Spent garnet: (a) As received, freshly/ raw material of spent garnet waste; (b) After the drying and sieving process.

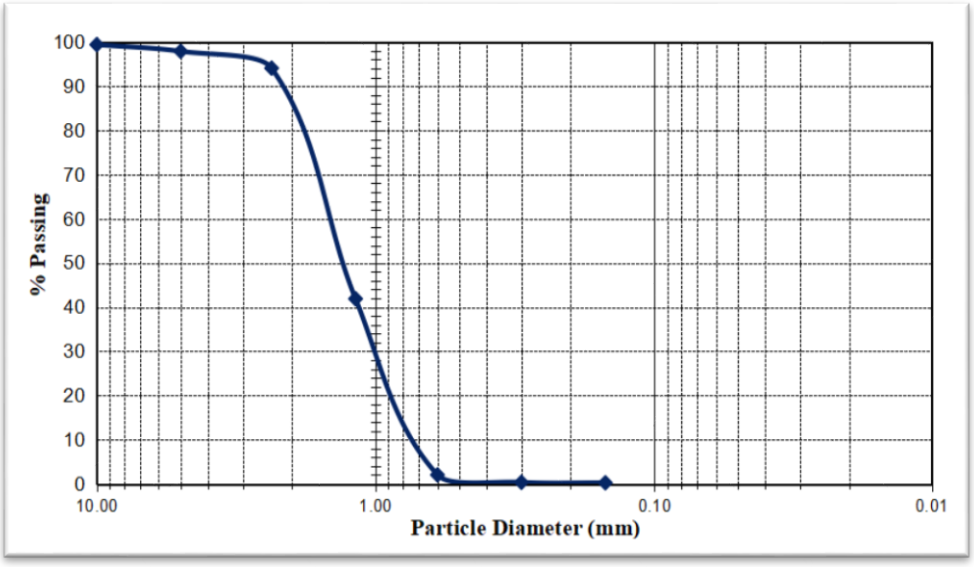

Fig. 4. Particle size distribution for spent garnet.

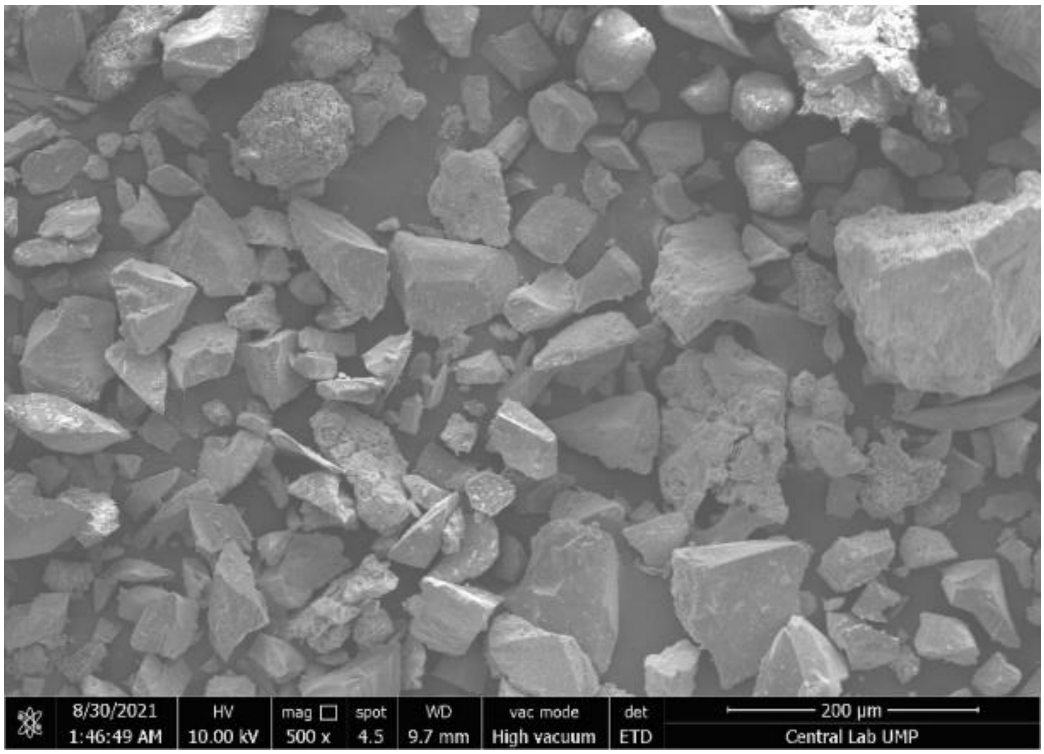

Fig. 5. Image of spent garnet at magnification of 500x.

Table 1. Chemical composition of spent garnet.

Chemical composition	Spent garnet (%)
Silicon dioxide (SiO^2)	39.04
Aluminium oxide (Al_2O_3)	13.40
Iron oxide (Fe_2O_3)	40.23
Magnesium oxide (MgO)	4.08
Sulfur trioxide (SO_3)	0.38
Potassium oxide (K_2O)	0.32
Manganese (II) oxide (MnO)	1.03
Titanium (IV) dioxide (TiO_2)	1.53

2.2. Mix proportion and specimen preparation

Six mortar mixes were utilized in the experimental work, which was conducted at the concrete laboratory. The mortar with 100% river sand acting as fine aggregate was used as the control specimen. The other mixtures contained various percentages of spent garnet: 10%, 20%, 30%, and 40%. The mixture design for this research is presented in Table 2. Before mortar casting, molds were ensured to be in good condition without any defects or cracks in the inner part of it to prevent leakage of mortar mixture during the casting process. Then, the chosen mold was prepared by removing any dirt or hardened mortar pieces from its surface. Subsequently, a thin coating of grease was applied to the interior surface of the mold. The cement, sand, spent garnet, and water were weighed carefully. All materials were placed in a clean tray, beginning with the mixing of the dry components: cement, followed by sand, spent garnet, and finally water. The materials were thoroughly mixed and cast into cube molds in layers. After placing the first layer, it was compacted on a vibrating table, and the process was repeated for the next two layers. The mold was then placed on a storage rack and left overnight for the hardening process. After 24 hours, all cubes were demolded and labelled clearly for easier identification. Finally, the cubes were immersed in a curing tank filled with tap water for 7 and 28 days. During the experimental work, the humidity of the environment is between 80%–84% with temperature 27 °C to 30 °C. Fig. 6 presents the mortar specimens preparation process.

2.3. Testing

Four tests were conducted in this research: the flow table test, compressive strength test, density test, and fire resistance test. The workability of the mortar was assessed by conducting a flow table test immediately after mixing. The testing were conducted by adhering to the procedure in ASTM C1437-07 (2007). The compressive strength test was conducted to determine the mortar's ability to withstand load per unit area. The test was conducted using a compression testing machine on specimens that had undergone water curing for 7 and 28 days. Testing was conducted in accordance to ASTM C109M-20 (2020). The fire resistance test was carried out on 28 days water cured specimens. This test was performed to assess the performance of mortar with spent garnet as a partial replacement for fine aggregate under high temperatures. The specimens were exposed to temperatures of 200 °C, 400 °C, 600 °C, and 800 °C for two hours following the experimental method of past researcher Arioz (2007). Main apparatus used for the testing in this research work are illustrated in Fig. 7.

Table 2. Mix proportion (kg/m^3).

Mix	Cement (kg/m^3)	River Sand (kg/m^3)	Sieved spent garnet (kg/m^3)	Water content (kg/m^3)
A (0%)	260	600	0	160
B (10%)	260	540	60	160
C (20%)	260	480	120	160
D (30%)	260	420	180	160
E (40%)	260	360	240	160

Fig. 6. Mortar specimen preparation process.

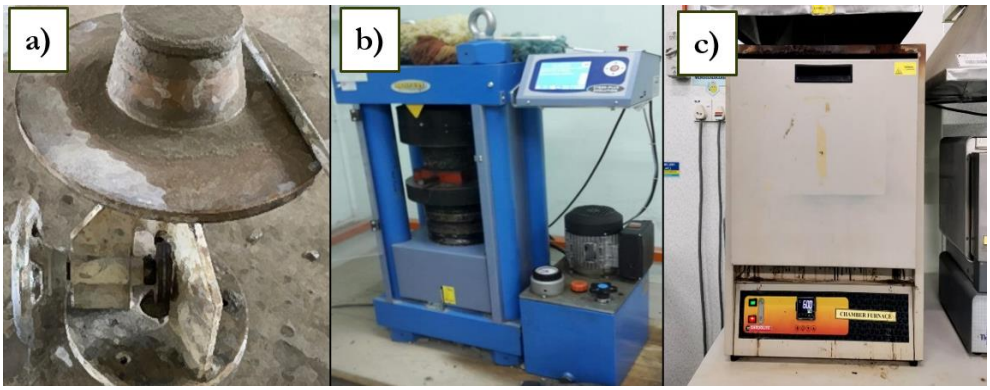

Fig. 7. Testing apparatus used: (a) Flow table; (b) Compression machine; (c) Electric furnace.

3. Results and Discussion

3.1. Flowability

Fig. 8 demonstrates the impact of varying percentages of spent garnet used as a partial replacement for fine aggregate on the flowability of the mortar. The results show an increase in mortar flow as the percentage of spent garnet replacement increases. The flow percentages for mortar with 0%, 10%, 20%, 30%, and 40% spent garnet are 68.3%, 92%, 101%, 127.3%, and 142%, respectively. The mortar with 0% spent garnet exhibits the lowest flowability, whereas mix with 40% spent garnet replacement exhibits the highest flowability. Fig. 9 illustrates the variation in the flowability of mix with 0% spent garnet and 40% spent garnet. The increment in the flowability in the mixture consisting higher content of spent garnet is attributed to its higher bulk density (2,740 kg/m^3) in comparison to sand (1,935 kg/m^3). Similar trend in workability improvement upon blending of spent garnet as a replacement for sand in concrete has also been reported by Budiea et al. (2021) and Jamaludin et al. (2022b). However, excessive replacement levels may lead to a segregation risk, potentially affecting cohesion and uniformity in fresh mortar. While increased flowability is advantageous for workability and ease of placement, its impact on hardened properties, particularly compressive strength, must be carefully assessed.

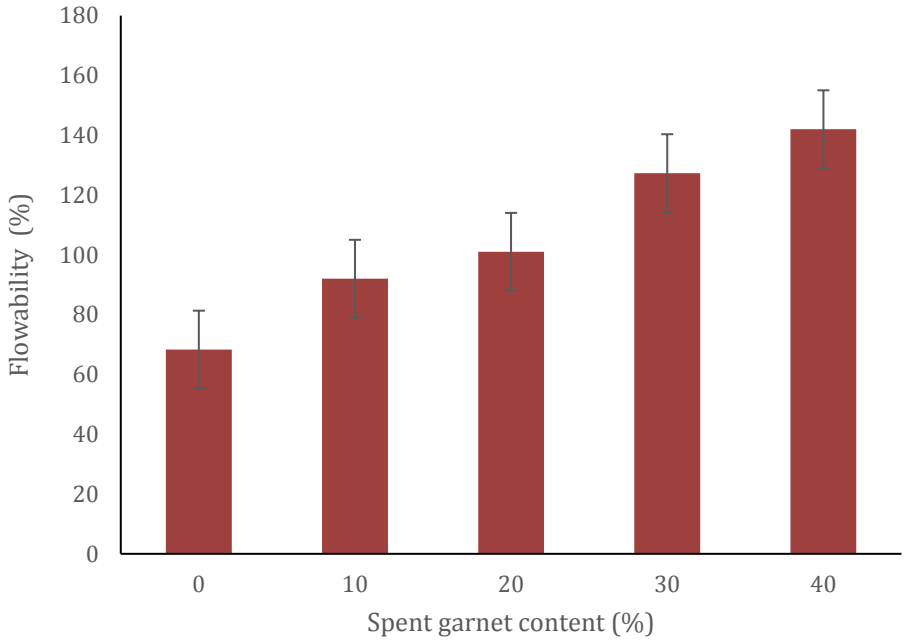

Fig. 8. Flowability test result.

Fig. 9. Flow of control mix and mortar with 40% spent garnet.

3.2. Density

The chart in Fig. 10 illustrates the effect of partially replacing fine aggregate with spent garnet on mortar density. Results indicate a consistent increase in density with higher replacement levels. Mortar incorporating 0%, 10%, 20%, 30%, and 40% spent garnet showed density values of 4,958 kg/m^3, 5,024 kg/m^3, 5,028 kg/m^3, 5,066 kg/m^3, and 5,180 kg/m^3, respectively. The 40% replacement mix exhibited the highest density, attributed to the higher bulk density of spent garnet (2,740 kg/m^3) compared to river sand, as well as its pore-filling effect, which enhances matrix compaction. Higher mortar density is generally linked to improved durability, reduced permeability, and increased resistance to environmental degradation, as supported by previous studies (Neville 2011; Li et al. 2019). Therefore, while 40% replacement yields the greatest density gain, practical applications should consider an optimal balance between increased density and mechanical or workability performance.

3.3. Compressive strength

Table 3 and Fig. 11 illustrate the compressive strength of mortar incorporating varying percentages of spent garnet as a partial replacement for fine aggregate. In general, all mixes, whether containing spent garnet or not–show increased strength over time due to continued C-S-H gel formation from uninterrupted hydration. The control mix (0% garnet) recorded the lowest strength, rising from 33.73 MPa at 7 days to 35.82 MPa at 28 days. The mix with 20% replacement achieved the highest strength at both ages, reaching 37.95 MPa and 50.99 MPa, respectively. This enhancement is likely due to finer size of spent garnet that acts as filler material contributing towards more compact internal structure of mortar mix. Other than that, the rough, angular texture of spent garnet could also be one of the factor that contribute towards improvement of bonding at the cement–aggregate interface. Replacements up to 40% also demonstrated strength gains over the control, possibly influenced by the higher density of the garnet particles.

However, higher replacement levels may introduce workability issues or reduced long-term durability, which should be considered in future applications. Similar findings have been reported in high-strength lightweight concrete by Muthusamy et al. (2022) and Jaafar et al. (2024).

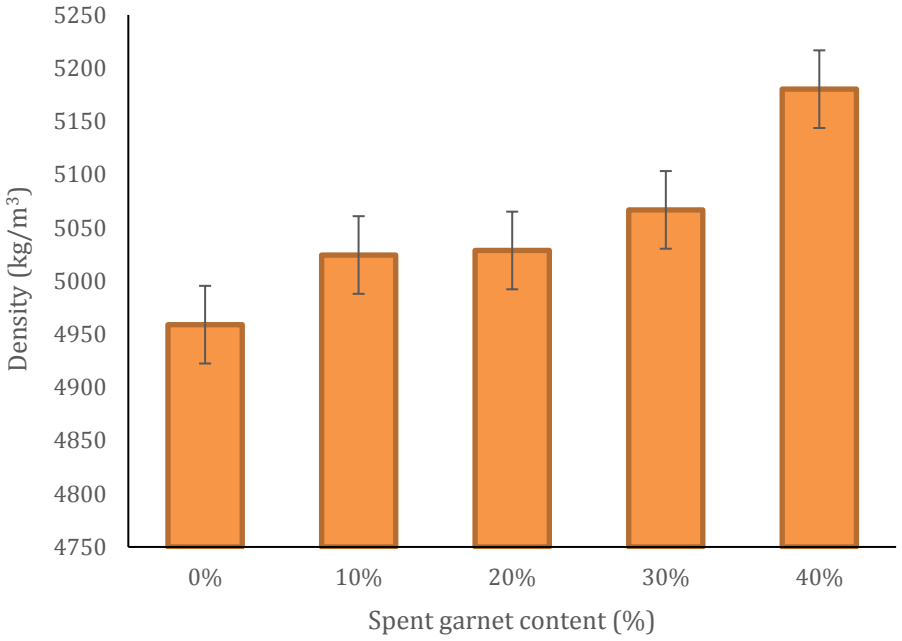

Fig. 10. Effect of spent garnet content on the density of mortar.

Table 3. Compressive strength of mortar with varying percentages of spent garnet.

Spent garnet content	Compressive strength (MPa) 7 days	Compressive strength (MPa) 28 days
0%	33.73	35.18
10%	36.97	40.90
20%	37.95	50.99
30%	33.15	49.65
40%	31.83	41.51

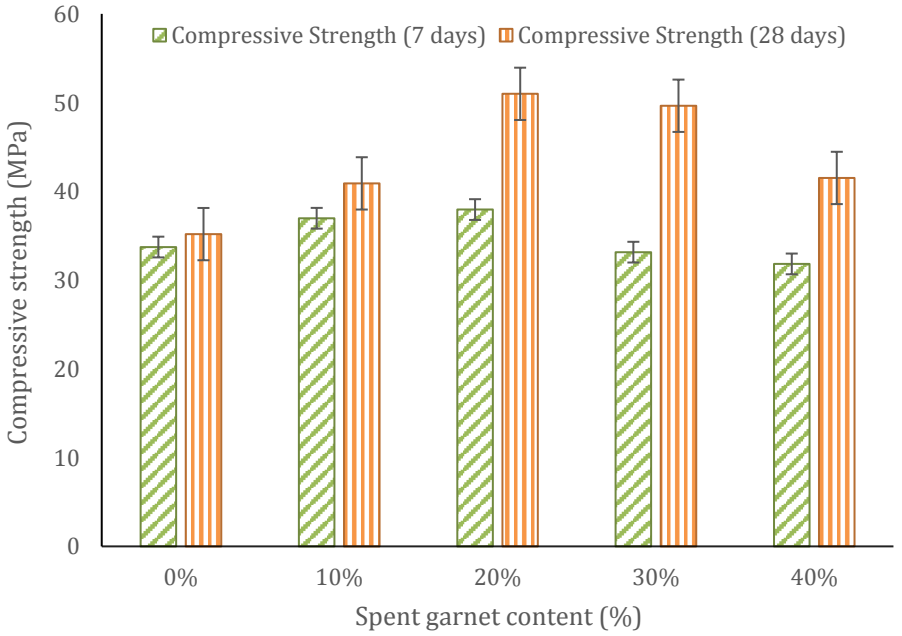

Fig. 11. Effect of spent garnet on compressive strength of mortar.

3.4. Fire resistance

Table 4 and Fig. 12 illustrate the percentage of mass loss in mortar when using different proportions of spent garnet. The chart indicates that the percentage of spent garnet replacement as sand is directly proportional to the mass loss of the mortar.

The mass loss for mortar with 10% spent garnet replacement at 200 °C, 400 °C, 600 °C, and 800 °C was 8.87%, 12.1%, 13.18%, and 14.12%, respectively. The mortar with 40% spent garnet exhibited the highest mass loss at 400 °C and 800 °C, with values of 12.23% and 14.33%, respectively. As expected, mass loss increased with rising temperatures. Similar observations have been noted by previous researchers, Nayel et al. (2020) and Jaafar et al. (2024). Among the different replacement levels, mortar containing 10% and 20% spent garnet showed the least mass loss. This occurred because spent garnet helps fill pores, making the mortar denser. However, excessive garnet replacement can lead to increased mass loss, as it enlarges voids within the mortar specimen.

Table 4. Percentage of mass loss in mortar when using different proportions of spent garnet.

Spent garnet content	Mass loss (%) 200	Mass loss (%) 400	Mass loss (%) 600	Mass loss (%) 800
0%	9.36	12.22	13.47	13.94
10%	8.87	12.10	13.18	14.12
20%	9.04	11.99	13.61	14.03
30%	8.99	12.20	13.81	13.93
40%	9.35	12.23	13.30	14.33

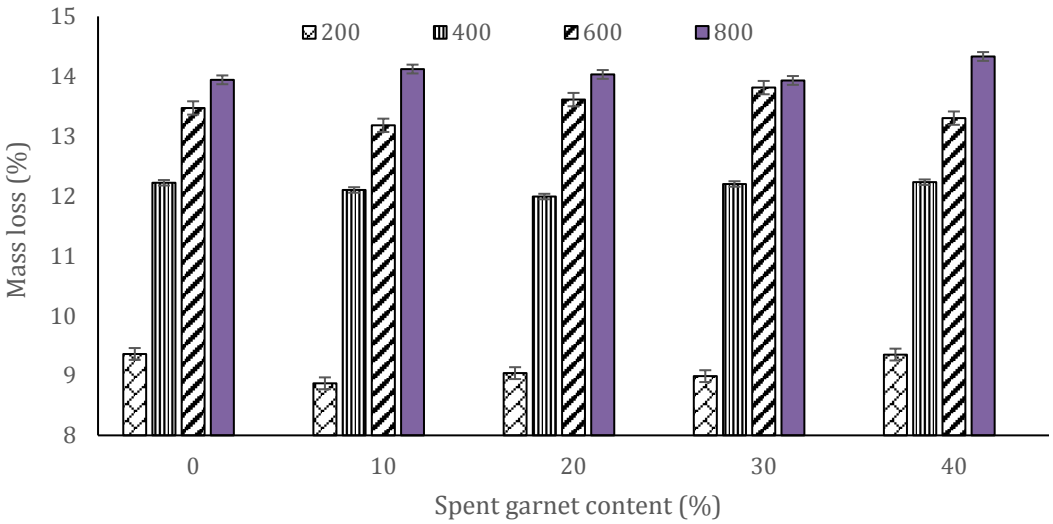

Fig. 12. Mass loss of mortar containing different spent garnet contents when subjected to diverse high temperatures.

4. Conclusions

The study explores the effects of using spent garnet as a partial replacement for fine aggregate in mortar, examining flowability, density, compressive strength, and thermal resistance. Flowability increased with higher garnet content, from 68.3% at 0% replacement to 142% at 40%, due to the higher bulk density of garnet (2,740 kg/m^3) compared to sand (1,935 kg/m^3). The 40% replacement mix showed the greatest workability. However, excessive replacement could cause segregation, affecting the mixture's cohesion. Density also improved with increased garnet content, rising from 4,958 kg/m^3 at 0% replacement to 5,180 kg/m^3 at 40%. This is due to garnet's higher density and pore-filling properties, leading to better matrix packing and potentially greater durability.

Compressive strength increased across all mixes with curing time. The 20% spent garnet mix exhibited the highest compressive strength (37.95 MPa at 7 days and 50.99 MPa at 28 days), attributed to garnet's rough texture, which enhances bonding with cement. Although the control mix had the lowest strength, mortars with 0% and 10% garnet showed relatively high strength in comparison to other mixes. Thermal analysis showed that mass loss increased with temperature and garnet content. Mortars with 10% and 20% replacement exhibited the lowest mass loss, suggesting an optimal balance between garnet and cement, which improved thermal stability. In contrast, excessive garnet increased porosity, weakening the matrix under high heat. Based on the overall results, the optimum spent garnet replacement for enhanced mortar performance, balancing workability, strength, and thermal resistance, is 20%.

Acknowledgements

None declared.

Funding

This research was supported by Universiti Malaysia Pahang Al-Sultan Abdullah from under grant number RDU223006.

Conflict of Interest

The authors declared no potential conflicts of interest with respect to the research, authorship, and/or publication of this manuscript.

Author Contributions

All of the authors made substantial contributions to conception and design, or acquisition of data, or analysis and interpretation of data; were involved in drafting the manuscript or revising it critically for important intellectual content; and gave final approval of the version to be published.

Data Availability

The datasets created and/or analyzed during the current study are not publicly available, but are available from the corresponding author upon reasonable request.

REFERENCES

Alaloul WS, Liew MS, Zawawi NAWA, Mohammed BS (2021). Construction sector contribution to economic stability: Malaysian GDP distribution. *Sustainability*, 13(9), 5012.

Arioz O (2007). Effects of elevated temperatures on properties of concrete. *Fire Safety Journal*, 42, 516–522.

Budiea AMA, Sek WZ, Mokhatar SN, Muthusamy K, Yusoff ARM (2021). Structural performance assessment of high strength concrete containing spent garnet under three point bending test. *IOP Conference Series: Materials Science and Engineering*, 1144(1), 012018.

ASTM C109M-20 (2020). Standard Test Method for Compressive Strength of Hydraulic Cement Mortars (Using 2-in. or [50 mm] Cube Specimens). ASTM International, West Conshohocken, PA.

ASTM C1437-07 (2007). Standard Test Method for Flow of Hydraulic Cement Mortar. ASTM International, West Conshohocken, PA.

Digvijay S, Onkar S (2022). Global construction aggregates market to reach $621.1 billion by 2031: Allied Market Research. *Construction Times,* Online Article. https://www.globenewswire.com/news-release/2022/7/20/2482402/0/en/Global-Construction-Aggregates-Market-Is-Expected-to-Reach-621-1-Billion-by-2031-Allied-Market-Research.html [accessed 01-06-2025].

Dinh HL, Liu J, Ong DEL, Doh JH (2022). A sustainable solution to excessive river sand mining by utilizing by-products in concrete manufacturing: A state-of-the-art review. *Cleaner Materials*, 6, 100140.

Huseien GF, Sam ARM, Shah KW, Budiea AMA, Mirza J (2019). Utilizing spend garnets as sand replacement in alkali-activated mortars containing fly ash and GBFS. *Construction and Building Materials*, 225, 132–145.

Jaafar MF, Muthusamy K, Jamaludin NFA, Jasni SA, Zulkarnain F (2024). Fire resistance of lightweight aggregate concrete containing spent garnet as partial fine aggregate replacement. *Open Construction Building Technology Journal*, 18, e18748368294704.

Jamaludin NFA, Muthusamy K, Isa NN, Md Jaafar MF, Ghazali N (2022a). Use of spent garnet in industry: A review. *Materials Today: Proceedings*, 48, 728–733.

Jamaludin NFA, Muthusamy K, Md Jaafar MF, Putra Jaya R, Ismail MA (2022b). Performance of palm oil clinker lightweight aggregate concrete comprising spent garnet as fine aggregate replacement. *Advances in Civil Engineering*, 2022, Article ID 9674096.

Jamaludin NFA, Muthusamy K, Md Jaafar MF, Ali Z, Abdul Majid Z, Ismail MA (2024). Preliminary investigation on spent garnet as a novel supplementary cementitious material. *Construction and Building Materials*, 451, 138789.

Li X, Chen Y, Zhang M, Wang Y (2019). Influence of density on durability performance of high-performance concrete. *Construction and Building Materials*, 211, 324–331.

Ludacer R (2018). The world is running out of sand – and there's a black market for it now. *Business Insider India,* Online Article. https://www.afr.com/companies/mining/the-world-is-running-out-of-sand--and-theres-a-black-market-for-it-now-20180612-h11953 [accessed 01-06-2025].

Mokhatar SN, Yusoff ARM, Budiea AMA, Hakim SJS (2022). A review: Study on spent garnet as construction material. *International Journal of Integrated Engineering*, 14(5), 73–80.

Muellegger C, Weilhartner A, Battin TJ, Hofmann T (2013). Positive and negative impacts of five Austrian gravel pit lakes on groundwater quality. *Science of the Total Environment*, 443, 14–23.

Muthusamy K, Jamaludin NFA, Zainuddin AZ, Md Jaafar MF, Mehmet Serkan K (2022). Effect of spent garnet waste as partial fine aggregate replacement on properties of high strength lightweight aggregate concrete. *Key Engineering Materials*, 912, 17–23.

Muttashar HL, Ali N, Ariffin MA, Hussin MW (2018). Microstructures and physical properties of waste garnets as a promising construction materials. *Case Studies in Construction Materials*, 8, 87–96.

Muttashar HL, Ariffin MAM, Hussein MN, Hussin MW, Ishaq S (2018). Self-compacting geopolymer concrete with spend garnet as sand replacement. *Journal of Building Engineering*, 15, 85–94.

Nayel IH, Nasr MS, Abdulridha SQ (2020). Impact of elevated temperature on the mechanical properties of cement mortar reinforced with rope waste fibres. *IOP Conference Series: Materials Science and Engineering*, 671(1), 012080.

Neville AM (2011). *Properties of Concrete* (5th ed.). Pearson Education Limited, Essex.

Ruslan HN, Muthusamy K, Muzafar Shah MH, Mat Yahaya F, Zulkarnain F (2024). Properties of concrete containing spent garnet as fine aggregate replacement. *IOP Conference Series: Earth and Environmental Science*, 1369(1), 012039.

Sherry E, Philippe C (2025). A review of river sand mining: Methods, impacts, and implications. *Next Research*, 2(1), 100149.

Shitima C, Suykens B (2023). Formalization of sand mining in Dar es Salaam, Tanzania. *Resources Policy*, 82, 103589.

Whiting K (2019). Sand mining: How it impacts the environment and solutions. *World Economic Forum,* Online Article. https://www.weforum.org/stories/2023/09/global-sand-mining-demand-impacting-environment/ (updated in 2023) [accessed 01-06-2025].

Challenge Journal of Concrete Research Letters

Research Article

Predicting compressive strength of heavyweight concrete using deep neural networks and Box–Behnken design

Amir Hossein Derakhshan Nezhad [a], Seayf Allah Hemati [a,*], Omid Rezaifar [a]

[a] *Department of Civil Engineering, Semnan University, 35131-19111 Semnan, Iran*

ABSTRACT

This study investigates the prediction and evaluation of compressive strength in heavyweight concrete incorporating magnetite and steel slag, using two advanced modeling techniques: Deep Artificial Neural Networks (DANN) and Box-Behnken Response Surface Methodology (BBRSM). A total of 324 concrete specimens were prepared based on 36 unique mix designs. Non-destructive testing methods ultrasonic pulse velocity (UPV) and Schmidt rebound hammer (SRH) were employed to characterize material properties. The 28-day compressive strength of each sample was determined following ASTM C39 standards. Data from UPV and SRH tests, along with mix parameters such as the water-cement ratio, were used as inputs for both models. The DANN model, developed using a hybrid architecture combining Convolutional Neural Network (CNN) and Long Short-Term Memory (LSTM), achieved superior predictive performance, with a coefficient of determination (R^2) of 0.9951 and a root mean square error (RMSE) of 0.0314 MPa. This corresponds to a coefficient of variation of just 0.045%, with a standard deviation error of 0.02% relative to the mean compressive strength of approximately 70 MPa. In contrast, the BBRSM model, employing a sixth-degree polynomial equation, yielded an R^2 of 0.9628 and a standard deviation of residuals of 1.36 MPa (about 1.94% of the average strength). The findings highlight the enhanced accuracy and efficiency of the Hybrid DANN model over the BBRSM approach. While both techniques offer practical, cost-effective alternatives to experimental testing, the DANN model is particularly well-suited for capturing complex nonlinear behaviors, whereas BBRSM remains valuable for optimization-oriented analysis.

ARTICLE INFO

Article history:
Received – April 30, 2025
Revision requested – July 5, 2025
Revision received – July 11, 2025
Accepted – July 28, 2025

Keywords:
Heavyweight concrete
Deep artificial neural network
Box-Behnken response surface analysis
Non-destructive techniques
Modeling

Citation: Derakhshan Nezhad AH, Hemati SA, Rezaifar O (2025). Predicting compressive strength of heavyweight concrete using deep neural networks and Box–Behnken design. *Challenge Journal of Concrete Research Letters*, 16(4), 173–202.

1. Introduction

Artificial Neural Networks (ANNs) have emerged as potent instruments for forecasting concrete's compressive strength, owing to their capacity to assimilate knowledge from intricate datasets, discern concealed patterns, and model complex, nonlinear, multivariate relationships (Abbass et al. 2023; Angiulli et al. 2024a, 2024b). These models, distinguished by their multi-layered architectures, advanced optimization paradigms, and resilience to data noise, have markedly im-proved prediction precision compared to conventional empirical models (Ansari et al. 2024; Asteris et al. 2016; Asri et al. 2022). Concurrently, Response Surface Methodology (RSM), recognized as an exceptionally efficient tool for experimental design, facilitates the examination of variable interactions and the elucidation of complex correlations with a reduced number of experiments (Asteris et al. 2021; Benaicha 2024). The synergy of RSM with artificial neural networks not only curtails laboratory expenditures but also assists in refining predictive models and elevating the fidelity of mechanical property simula-

* *Corresponding author*. E-mail address: shemati@semnan.ac.ir (S. A. Hemati)
ISSN: 2548-0928 / DOI: https://doi.org/10.20528/cjcrl.2025.04.002

tions for concrete. Heavyweight concrete, a sophisticated material in structural engineering, occupies a pivotal role in demanding applications such as radiation shielding in nuclear power facilities, radiotherapy departments in hospitals, blast-resistant constructions, and robust industrial foundations (Boccacci et al. 2024; Lai et al. 2022; Wardenier et al. 2010). This concrete variant is typically formulated with dense aggregates like barite, hematite, magnetite, or serpentine, which contribute to its elevated density and influence its microstructural and dynamic characteristics (Iqbal et al. 2020; Mirzaie Aliabadi et al. 2024; Shahidzadeh et al. 2024a, 2024b). The intricate composition, internal heterogeneities, and inherent nonlinear properties of heavyweight concrete present considerable challenges to the precise assessment of its mechanical attributes, particularly its compressive strength (Moura et al. 2023; Pal et al. 2023; Reddy et al. 2024). Compressive strength, being the paramount performance indicator for concrete, is contingent upon numerous factors, including the water-to-cement ratio, aggregate type and grading, final density, curing conditions, and internal microstructure (Pazouki et al. 2023; Sathiparan et al. 2024; Yousef et al. 2024). For heavyweight concrete, direct evaluation of compressive strength is compounded by difficulties in execution, potentially leading to inaccuracies or specimen damage, largely due to wave scattering, energy attenuation by dense aggregates, and nonlinear material behavior (Sadowski et al. 2020; Silva et al. 2021; Yang et al. 2019). In such contexts, non-destructive testing (NDT) methodologies, specifically Ultrasonic Pulse Velocity (UPV) and Schmidt Rebound Hammer (SRH) tests, have garnered significant attention as dependable, swift, and cost-effective means for both qualitative and quantitative assessment of concrete characteristics (Sayyar-Roudsari et al. 2024; Wang et al. 2024; Zhang et al. 2021a). The UPV technique gauges parameters such as density, homogeneity, the presence of internal flaws or voids, and the dynamic modulus of elasticity by measuring the propagation time of ultrasonic waves through the concrete (Sathiparan et al. 2023; Zheng et al. 2024; Zhu et al. 2023). Similarly, the SRH method estimates compressive strength by evaluating the concrete's surface hardness (Jibril et al. 2023; Kouddane et al. 2023; Murty et al. 2024). Nevertheless, within heavyweight concrete, the direct interpretation of NDT results frequently entails substantial error due to structural complexities and energy absorption within dense aggregates, and conventional linear regression models prove inadequate in accurately correlating with experimental data (Chou et al. 2015; Feng et al. 2020; Zhang et al. 2021b). Recent strides in artificial intelligence paradigms and advanced statistical modeling have broadened horizons for analyzing the behavior of nonlinear concrete systems (Asteris et al. 2021; Ramkumar et al. 2020). For instance, (Sathiparan et al. 2024) employed non-destructive measurements, including ultrasonic pulse velocity and electrical resistivity, to forecast the attributes of permeable concrete, directly endorsing the non-destructive appraisal of mechanical properties. (Ramkumar et al. 2020) incorporated artificial neural networks to predict concrete performance by exploring the impact of mineral admixtures and steel fibers in self-compacting concrete (SCC), emphasizing the capacity of machine learning for optimizing SCC's mechanical char-acteristics. (Astris et al. 2021) successfully predicted concrete compressive strength using soft computing and non-destructive approaches, validating the utility of ultrasonic pulse velocity in performance evaluation. (Angioli et al. 2024) illustrated that integrating ultrasonic techniques and artificial intelligence in concrete monitoring facilitates early anomaly detection, yielding up to a 25% enhancement in localization accuracy and up to a 40% reduction in maintenance expenses. Furthermore, (Benaisha et al. 2024) formulated an AI-driven model, achieving a determination coefficient of 0.99 with ultrasonic pulse velocity to predict self-compacting concrete's compressive strength, presenting it as a non-destructive, rapid, and sustainable alternative to conventional methods.

Prior investigations have indicated that response surface methods and traditional artificial intelligence algorithms frequently face issues such as escalating nonlinear errors, computational intensity, and multifaceted regression scenarios, which adversely impact analytical accuracy and efficiency. Despite extensive research on estimating concrete strength using non-destructive methods and machine learning techniques (Sadowski et al. 2020; Silva et al. 2021; Zhang et al. 2021a), the synergistic application of Box-Behnken Response Surface Methodology and Deep Artificial Neural Networks (DANN) for predicting the compressive strength of heavyweight concrete remains largely unexplored. Thus, the present investigation leverages deep artificial neural network models and the Box-Behnken response surface method to enhance existing methodologies for forecasting concrete compressive strength (Fig. 1). These approaches, along with the derived results, will be elucidated in subsequent sections. This study also contributes to simplifying predictive equations through the rigorous application of standard deviation, relative errors, root mean square error, and determination coefficient, thereby enabling the attainment of analytical findings that exhibit higher concordance with experimental data and superior accuracy.

2. Materials and Methods

This research was conducted in four key stages, which are schematically illustrated in Fig. 2:

- Formulation of the descriptive statement
- Implementation of the experimental program
- Modeling using the Box-Behnken response surface methodology and deep artificial neural networks
- Analysis of results

In the first stage, the descriptive statement was formulated, during which a comprehensive review of the existing literature was conducted and research innovations were identified. In the second stage, the mix design was determined, the specimens were prepared and tested, and the dataset was compiled through an experimental program. In the third stage, modeling was developed utilizing the Box-Behnken response surface methodology and deep artificial neural networks. During the fourth phase, a thorough assessment of the models developed was conducted, leading to the recommendation of suitable optimization strategies derived from the resultant data.

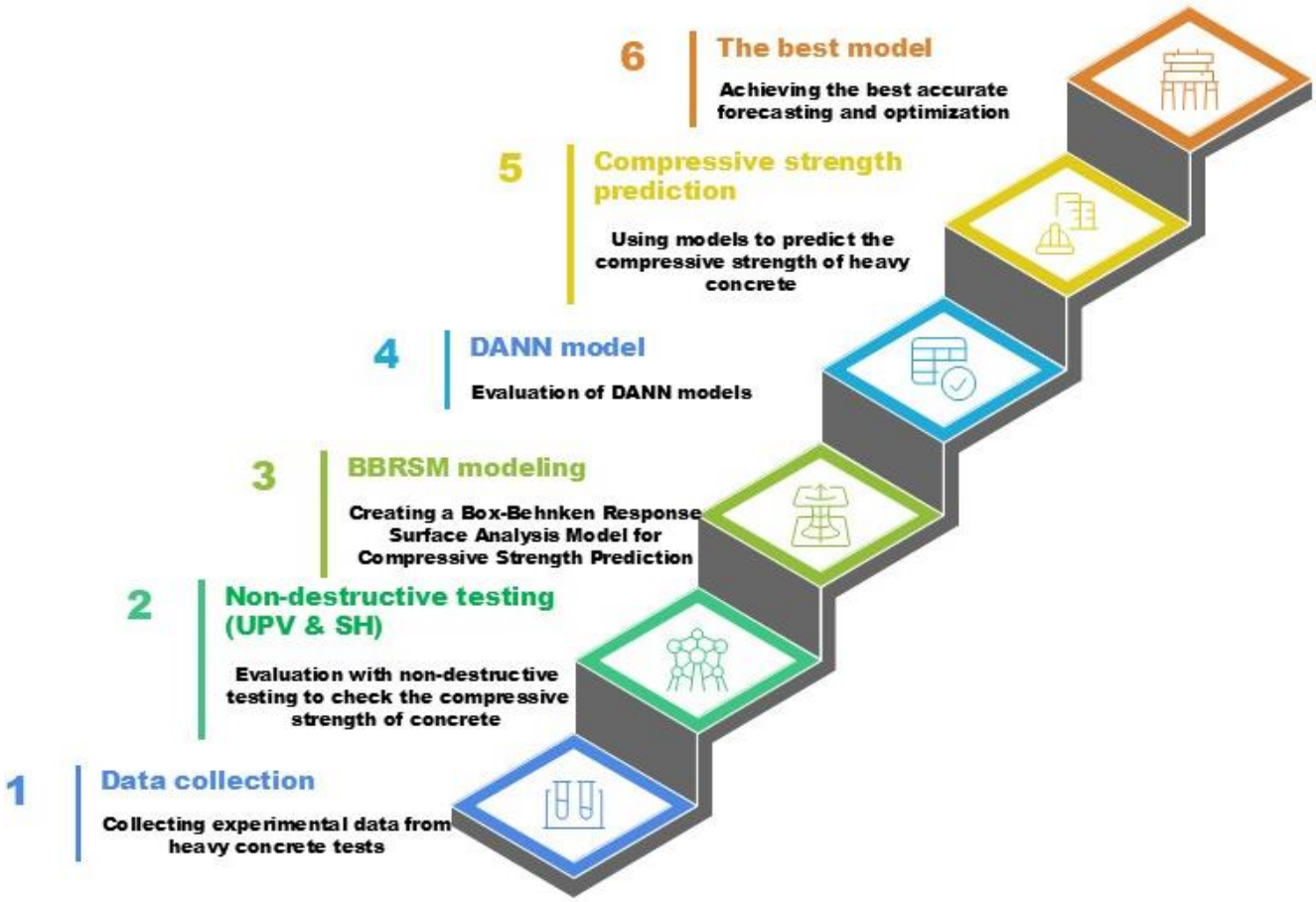

Fig. 1. Methodological workflow for assessing and predicting the compressive strength of heavyweight concrete.

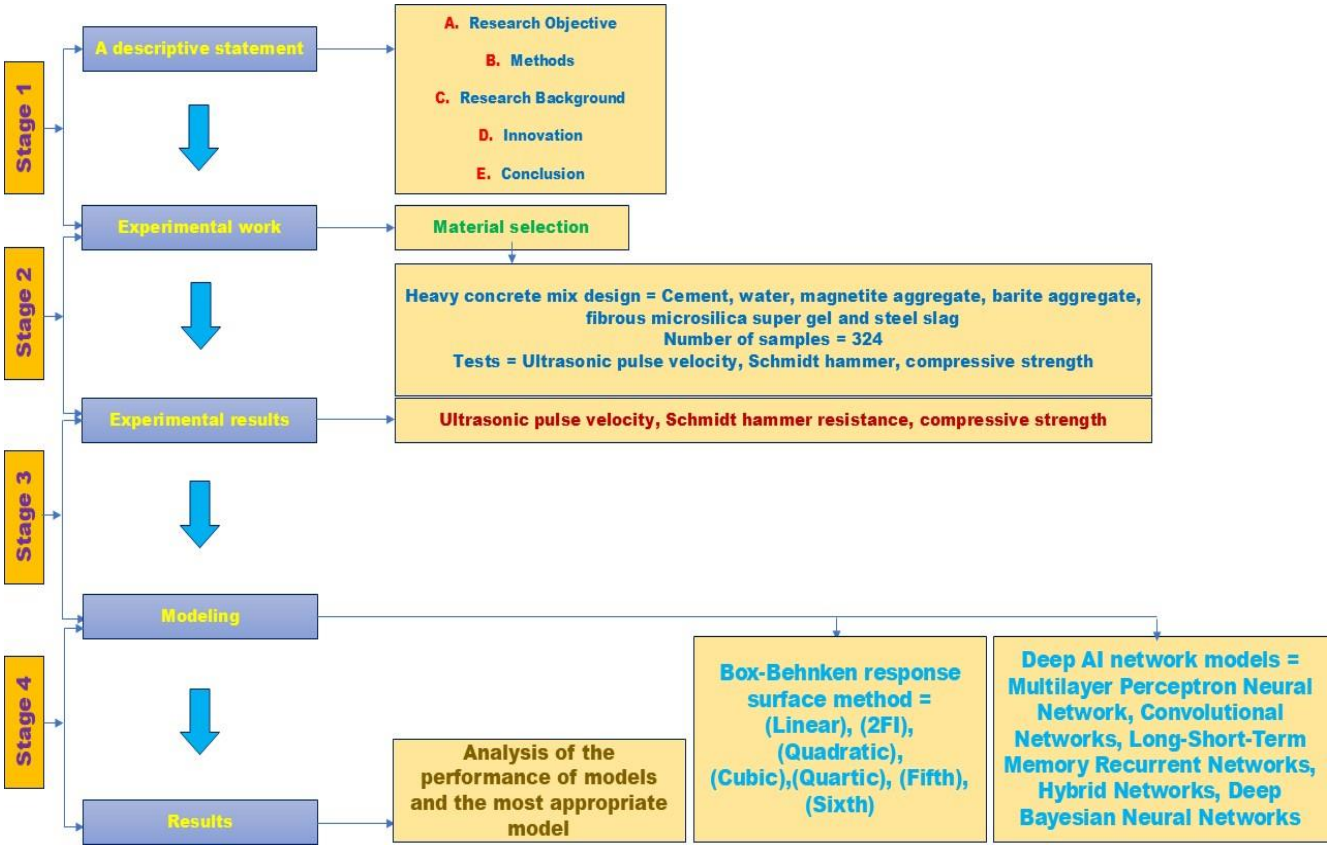

Fig. 2. Comprehensive framework for assessing the compressive strength of heavyweight concrete.

To achieve heavyweight concrete possessing optimal mechanical attributes, excellent workability, and sufficient flowability, raw materials underwent meticulous selection and assessment, adhering to ASTM specifications. The concrete mix proportions were formulated based on the methodology outlined in (Iqbal et al. 2020) to guarantee the dependability and consistency of the outcomes. The essential components comprising the heavyweight concrete mixture were cement, water, magnetite and barite aggregates, fiber-reinforced microsilica supergel, and steel slag. The subsequent section details the chemical constituents of these admixtures.

2.1. Cement

For this investigation, Type III Portland cement, sourced from the Shahroud factory and compliant with ASTM C150/C150M-22 (Roshan-Tabari et al. 2024), served as the principal binder. This specific cement type was chosen for its rapid-setting properties and its capacity to attain high early compressive strength, rendering it appropriate for heavyweight concrete applications that demand exceptional mechanical performance and accelerated strength development. Table 1 delineates the physical and chemical characteristics of the Type III Portland cement utilized.

Table 1. Physicochemical characteristics of Type III Portland cement.

Property	Value
Density (g/cm^3)	3.15
Specific surface area (m^2/kg)	520
Initial set time (minutes)	90
Final set time (minutes)	180
Compressive strength (MPa)	
- At 1 day	15.2
- At 3 days	28.6
- At 7 days	38.4
- At 28 days	55.7
Chemical composition (%)	
- Silicon dioxide (SiO_2)	20.2
- Aluminum oxide (Al_2O_3)	4.8
- Iron(III) oxide (Fe_2O_3)	3.5
- Calcium oxide (CaO)	64.1
- Magnesium oxide (MgO)	1.7
- Sulfur trioxide (SO_3)	2.8
- Alkali equivalent (Na_2Oeq)	0.55
- Tricalcium silicate (C_3S)	62.0
- Dicalcium silicate (C_2S)	15.0
- Tricalcium aluminate (C_3A)	9.0
- Tetracalcium aluminoferrite (C_4AF)	10.0
Loss on ignition (%)	2.3
Insoluble residue (%)	0.5

2.2. Water

The water used in the production of heavyweight concrete in this study has been carefully selected and evaluated in accordance with the ASTM C1602/C1602M-18 standard (Roshan-Tabari et al. 2024), ensuring its quality and compatibility with international criteria. As a key factor in the cement hydration process, this water has a significant impact on the workability, compressive strength, and durability of the heavyweight concrete. The quality of the consumed water, particularly with regard to its effect on chemical reactions and the stability of the concrete, has been thoroughly examined. The quality specifications of the water used are presented in Table 2.

Table 2. Quality parameters of water employed in heavyweight concrete manufacturing.

Feature	Value
pH	7.2
Total dissolved solids (TDS, mg/L)	320
Chloride content (mg/L)	45
Sulfate content (mg/L)	120
Alkalinity (mg/L as Na_2Oeq)	85
Organic material (mg/L)	5.0
Turbidity (NTU)	2.5
Water temperature (°C)	23

2.3. Magnetite coarse aggregate

For the fabrication of heavyweight concrete in this investigation, magnetite served as the coarse aggregate. Its elevated density and advantageous physicochemical characteristics led to its selection as an appropriate material for this application. This specific aggregate was sourced from magnetite deposits situated in Iran's Yazd region. The utilized sample adheres to the stipulations of ASTM C33/C33M-18. The magnetite coarse aggregate was chosen with a nominal maximum dimension of 20 mm to ensure consistent particle distribution and achieve optimal workability within the concrete mixture. Table 3 presents the physical properties and grading of the magnetite aggregates.

2.4. Barite aggregate

In this investigation, barite aggregate served as the fine aggregate component in the formulation of heavyweight concrete. Barite is extensively employed in heavyweight concrete production primarily due to its elevated density. The barite aggregate utilized in this research was procured from mining sites within Iran's Barite-Karan region, located in Hamadan province. This specific aggregate conforms to the specifications stipulated in ASTM C33/C33M-18. Table 4 presents the physicochemical characteristics of the barite aggregate.

Table 3. Physicochemical and gradation characteristics of coarse magnetite aggregates.

Property	Coarse magnetite (5-20 mm)
Density (g/cm^3)	5.0
Water absorption (%)	0.5
Fineness modulus	–
Particles finer than 75 microns (%)	0.8
Abrasion resistance (Los Angeles abrasion, %)	25.0
Soundness (weight loss %)	8.0
Chemical composition (%)	
- Fe_3O_4 (magnetite)	92.0
- SiO_2	3.5
- Al_2O_3	1.2
- Organic impurities (%)	0.1

Table 4. Physicochemical properties of barite fine aggregate.

Feature	Value
Particle size (mm)	3.0
Density (g/cm^3)	4.3
Water absorption (%)	0.3
Fineness modulus	2.6
Materials finer than 75 micrometers (%)	1.5
Soundness (weight loss %)	7.0
Chemical composition (%)	
- $BaSO_4$ (Baryte)	95.0
- SiO_2	2.0
- Fe_2O_3	1.2
- Al_2O_3	0.8
Organic impurities (%)	0.1

2.5. Fiber-reinforced micro-silica super gel

In this investigation, fiber-reinforced microsilica supergel was incorporated as a sophisticated additive designed to improve the mechanical, chemical, and rheological characteristics of heavyweight concrete. This fiber-reinforced microsilica supergel is a complex admixture, comprising constituents such as microsilica powder, a polycarboxylate ether-based superplasticizer, polypropylene fibers, and various polymeric modifiers. The product conforms to the stipulations of international standards, including ASTM C1240-20 and ASTM C494/C494M-19. Table 5 outlines the technical and chemical attributes of the fiber-reinforced microsilica supergel.

2.6. Steel slag

In this investigation, steel slag was incorporated as a coarse aggregate for producing heavyweight concrete. Steel slag, an industrial byproduct derived from electric arc furnace steel manufacturing, is regarded as a suitable alternative to traditional aggregates in heavyweight concrete due to its considerable density and advantageous mechanical characteristics. The steel slag utilized in this research originated from the Isfahan Mobarakeh Steel Company. This material adheres to the specifications set forth by ASTM C33/C33M-18 and ASTM C637-20. Table 6 outlines the technical and chemical properties of the steel slag.

3. **Experimental Program**

The constituents of the heavy concrete consist of Portland cement, water, magnetite aggregates, barite aggregates, fiber-reinforced microsilica supergel, and steel slag. Fig. 3 provides an overview of the constituents employed in the manufacture of heavyweight concrete.

Table 5. Technical and chemical attributes of fiber-reinforced microsilica supergel.

Feature	Value
Physical state	Thick slurry (gel-like in resting state, liquid after stirring)
Color	Dark gray
Specific gravity (g/cm^3)	1.45
pH	7.0 ± 0.5
Micro-silica content (%)	45
Micro-silica particle size (μm)	0.1–0.5
Chemical composition of micro-silica (%)	
- SiO_2	92.0
- Al_2O_3	1.2
- Fe_2O_3	0.8
Superplasticizer	Polycarboxylate ether (PCE)
Polypropylene fiber content (kg/m^3)	0.9
Polypropylene fiber length (mm)	12
Chloride ion (mg/L)	< 10
Workability time (minutes)	60–90
Water-to-cement ratio reduction (%)	15–20

Fig. 3. Components of heavyweight concrete.

Table 6. Physicochemical properties and chemical composition of coarse steel slag.

Property	Value
Particle size (mm)	12
Density (g/cm^3)	3.8
Water absorption (%)	1.2
Material passing 75 µm sieve (%)	0.9
Los Angeles abrasion resistance (%)	28
Soundness (weight loss, %)	10
Chemical composition (%)	
- CaO	35.0
- SiO_2	20.0
- Fe_2O_3	25.0
- MgO	8.0
- Al_2O_3	5.0
Organic impurities (%)	0.2
Volumetric stability (expansion, %)	0.4

For the current investigation, 36 distinct mix designs were developed, prepared, and subsequently evaluated utilizing the specified constituent materials. All phases of the design and mixing procedures adhered to the guidelines outlined in ACI 211. Detailed specifications for the heavyweight concrete mix designs are provided in Table 7.

Initially, all constituent materials for each mix design were precisely weighed and prepared for the blending operation within the mixer. The process commenced with the uniform mixing of dry components, including magnetite aggregates, barite, steel slag, and cement, inside the mixer for a duration of 2 minutes. Subsequently, water was incrementally introduced to the dry blend, and the mixing continued for an additional 2 minutes. In the subsequent step, fiber-reinforced microsilica supergel was incorporated into the mixture, followed by another 3 minutes of mixing to attain the desired workability. Finally, a concluding mixing phase of 2 minutes was performed to guarantee complete homogeneity of the composite. All experimental procedures were conducted under controlled environmental parameters: a temperature of 21°C, a wind velocity of 1 km/h, a relative humidity of 5%, and an air quality index (AQI) of 36, signifying good air quality. Consistent with extant scientific literature and prior research recommendations (Chou et al. 2015; Feng et al. 2020; Iqbal et al. 2020), the suggested water-to-cement (W/C) ratio for heavyweight concrete typically spans from 0.14 to 0.55. Concrete was cast into cubic molds, each measuring 150×150×150 mm. The concrete was systematically placed into the molds in three distinct layers, with each layer undergoing compaction using a standard tamping rod. This rod featured a striking face diameter of 5.08 cm and a mass of 2.5 kg, conforming to BS 1377–4:1990 (Iqbal et al. 2020). During compaction, the tamping rod was dropped from a height of 300 mm for each strike. Upon the completion of the third layer, the concrete surface was leveled using a straightedge, and any excess material was meticulously removed. For every mix design, 9 heavyweight concrete specimens were cast and prepared for testing, culminating in a total of 324 specimens (derived from 36 designs × 9 specimens), as illustrated in Fig. 4.

Fig. 4. Heavyweight concrete fabrication stages.

Table 7. General specifications of heavyweight concrete mix designs.

Mixed design number	Cement (kg/m³)	Water (kg/m³)	Steel slag (kg/m³)	Fiber-reinforced micro-silica super gel (kg/m³)	Magnetite aggregate (kg/m³)	Barite aggregate (kg/m³)	W/C	Density (kg/m³)
HC1	325	65	250	14	1850	700	0.20	4204
HC2	325	88	240	12	1880	720	0.27	4265
HC3	325	111	230	10	1910	740	0.34	4326
HC4	325	134	220	8	1940	760	0.41	4387
HC5	325	157	210	6	1970	780	0.48	4448
HC6	325	180	200	4	2000	800	0.55	4509
HC7	350	65	250	14	1850	700	0.19	4229
HC8	350	88	240	12	1880	720	0.25	4290
HC9	350	111	230	10	1910	740	0.32	4351
HC10	350	134	220	8	1940	760	0.38	4412
HC11	350	157	210	6	1970	780	0.45	4473
HC12	350	180	200	4	2000	800	0.51	4534
HC13	375	65	250	14	1850	700	0.17	4254
HC14	375	88	240	12	1880	720	0.23	4315
HC15	375	111	230	10	1910	740	0.30	4376
HC16	375	134	220	8	1940	760	0.36	4437
HC17	375	157	210	6	1970	780	0.42	4498
HC18	375	180	200	4	2000	800	0.48	4559
HC19	400	65	250	14	1850	700	0.16	4279
HC20	400	88	240	12	1880	720	0.22	4340
HC21	400	111	230	10	1910	740	0.28	4401
HC22	400	134	220	8	1940	760	0.34	4462
HC23	400	157	210	6	1970	780	0.39	4523
HC24	400	180	200	4	2000	800	0.45	4584
HC25	425	65	250	14	1850	700	0.15	4304
HC26	425	88	240	12	1880	720	0.21	4365
HC27	425	111	230	10	1910	740	0.26	4426
HC28	425	134	220	8	1940	760	0.32	4487
HC29	425	157	210	6	1970	780	0.37	4548
HC30	425	180	200	4	2000	800	0.42	4609
HC31	450	65	250	14	1850	700	0.14	4329
HC32	450	88	240	12	1880	720	0.20	4390
HC33	450	111	230	10	1910	740	0.25	4451
HC34	450	134	220	8	1940	760	0.30	4512
HC35	450	157	210	6	1970	780	0.35	4573
HC36	450	180	200	4	2000	800	0.40	4634

Following casting, the specimens underwent 24 hours of air-drying before being subjected to water curing at a controlled temperature for a period of 28 days.

3.1. Ultrasonic pulse velocity

The Ultrasonic Pulse Velocity (UPV) test functions as a non-destructive evaluation (NDE) technique for appraising the mechanical and structural attributes of concrete. This method involves the transmission of high-frequency sound waves and the measurement of their propagation time, thereby yielding data concerning the concrete's uniformity, density, elastic modulus, and the presence of internal flaws such as cracks or voids. Wave propagation velocity is enhanced in materials that are denser and more homogeneous, being influenced by factors like material density and internal discontinuities. The UPV test can be executed via direct, semi-direct, or indirect setups. While various empirical models have been put forth to correlate ultrasonic pulse velocity with

concrete compressive strength (Pazouki et al. 2023; Sathiparan et al. 2023, 2024; Sayyar-Roudsari et al. 2024; Wang et al. 2024; Zhang et al. 2021a; Zheng et al. 2024; Zhu et al. 2023), their general applicability is often restricted due to the inherent variability in concrete properties. In this investigation, ultrasonic pulse velocity measurements were conducted using a digital ND200 instrument (characterized by a 54 kHz frequency, a 2 MHz sampling rate, an accuracy of 0.1 microseconds, and a 1200-volt output voltage), adhering to ASTM C597 (Roshan-Tabari et al. 2024). Before commencing the tests, the device was calibrated using a reference bar, which exhibited a transit time of 25.4 microseconds. To optimize the acoustical coupling between the transducers and the specimen surface, POLYGEL gel was applied. Transducers were positioned on the surfaces of the cubic specimens, and an average of three readings (two horizontal and one vertical) was computed for each specimen. The experimental setup is depicted in Fig. 5.

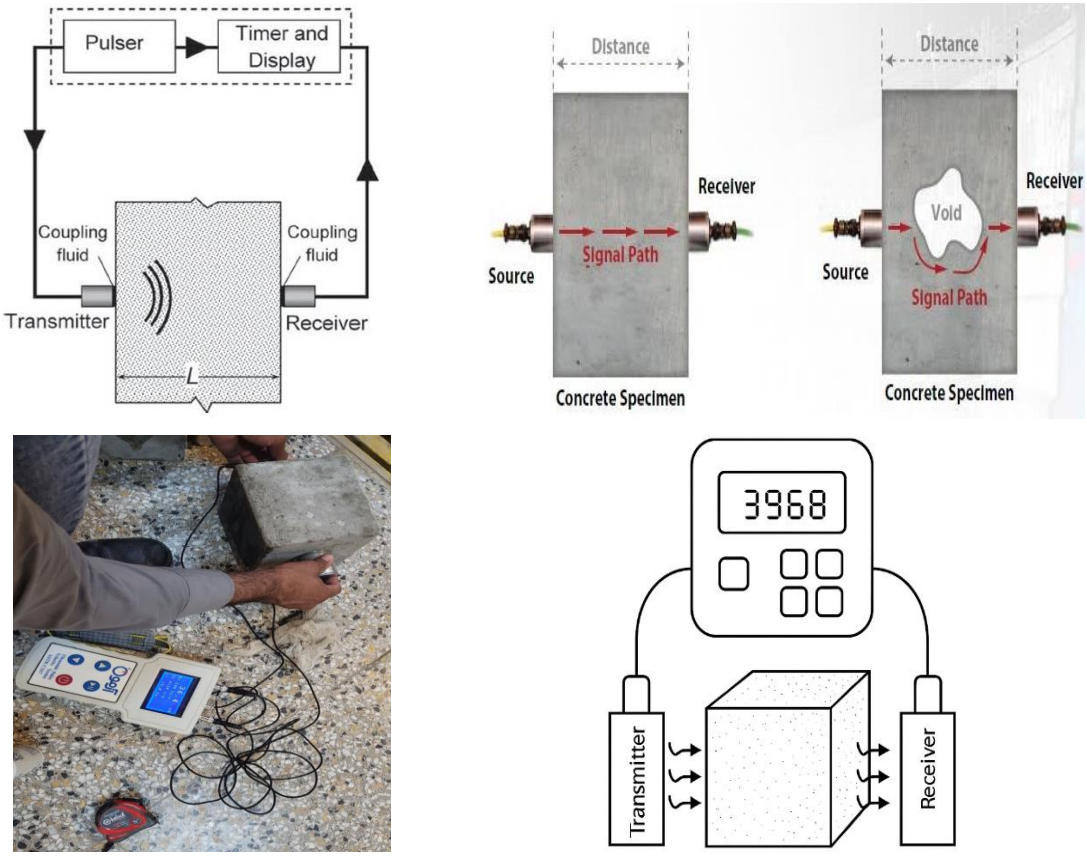

Fig. 5. Direct Method setup for ultrasonic pulse velocity testing apparatus on a cubic specimen.

3.2. Schmidt hammer test

The Schmidt Hammer test served as a non-destructive approach for assessing surface hardness and approximating concrete's compressive strength. This examination was performed with an N-type hammer, delivering an impact energy of 0.735 Newton-meters, in accordance with ASTM C805 standard (Wang et al. 2024). The rebound number (RN) was ascertained by striking the surface of cubic specimens, measuring 150×150×150 mm, at a temperature of 26°C. Before testing, the specimen surfaces were meticulously smoothed and cleared of any imperfections. Calibration of the Schmidt Hammer apparatus was carried out using a standard anvil that provided a reference rebound number of 80±2. For each specimen, ten acceptable readings (exhibiting a deviation of less than 6 units) were acquired from a 5×5 grid, and the mean rebound number (RN) was subsequently computed. The specimen grid arrangement is depicted in Fig. 6.

Fig. 6. Conducting the Schmidt hammer test on the cubic specimen.

3.3. Compressive strength assessment

The compressive strength of heavyweight concrete was evaluated to determine the specimens' load-bearing capability, adhering to ASTM C39 and ASTM C109 standards. Cubic specimens, each measuring 150×150×150 mm, were prepared from 36 distinct mix designs, designated as HC1 through HC36. Following the execution of non-destructive tests on these specimens, the compressive strength assessment was conducted. Testing involved subjecting the specimens to axial compression under displacement control, utilizing a hydraulic loading apparatus with a 2,000 kN capacity. An axial load was imposed at a displacement rate of 2 mm per minute, corresponding to a stress rate of 0.25 MPa per second. The test outcomes exhibited a standard deviation of 3 MPa and a coefficient of variation below 4%, thereby indicating the consistency of the results. The observed failure mode for the specimens was consistently conical and uniform, as illustrated in Fig. 7.

Fig. 8 provides an integrated summary of the concrete mix design, computational modeling, and empirical evaluation procedures for heavyweight concrete. In this investigation, six primary constituent materials, alongside the water-to-cement ratio (W/C), served as inputs for the Artificial Neural Network (ANN). A total of 324 cubic specimens were fabricated, derived from 36 distinct mix formulations. Data acquired from non-destructive tests, specifically the Schmidt Rebound Hammer (a) and Ultrasonic Pulse Velocity (b), in conjunction with the measured compressive strength values (c), were employed for the training and validation of the predictive model. This figure thus demonstrates a holistic methodology that synergizes experimental techniques with machine learning approaches for precise prediction of heavyweight concrete's mechanical attributes.

Fig. 7. Execution of the compressive strength test on a cubic specimen.

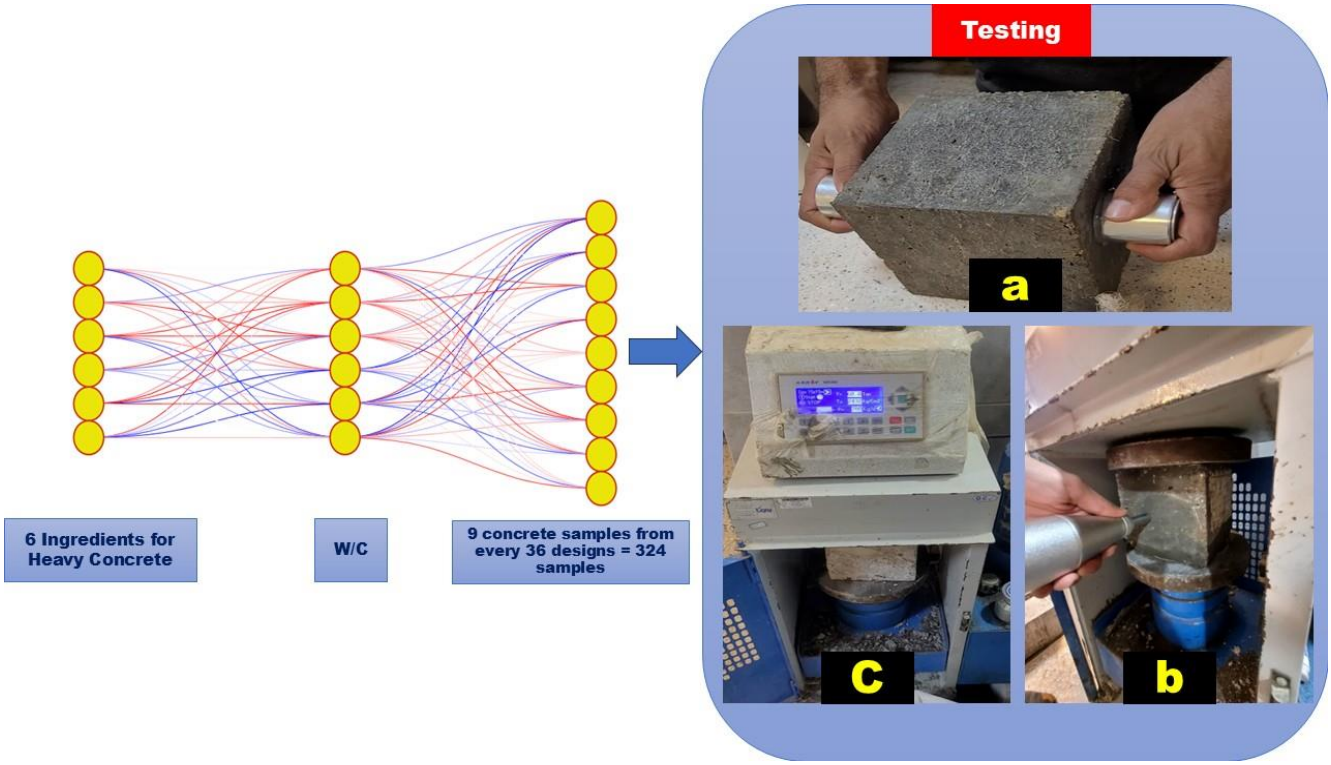

Fig. 8. Illustrative representation of hardened concrete assessments, encompassing ultrasonic pulse velocity, Schmidt hammer, and compressive strength tests.

3.4. Experimental results

The mean ultrasonic pulse velocity (UPV) for the heavyweight concrete samples, recorded using a digital ND200 instrument operating at a 500 kHz frequency as per ASTM C597 guidelines, spanned from 4.38 to 4.58 km/s. This interval reflects the consistency and compactness of the samples, influenced by the inclusion of magnetite and steel slag aggregates. The compressive strength, assessed via axial compression testing following ASTM C39 and C109 protocols after a 28-day curing period, ranged from 67.18 to 70.28 MPa. Simultaneously, the Schmidt hammer test, executed with an N-type device in compliance with ASTM C805 standards, produced rebound indices aligned with compressive strength values between 65.16 and 68.26 MPa, suggesting a marginally reduced estimate due to surface-related factors. The correlation between UPV and compressive strength was determined through a second-order polynomial regression model, expressed as $f(\mathrm{UPV}) = a.(\mathrm{UPV})^2 + b.\mathrm{UPV} + c$ where coefficients were calculated using the least-squares approach. This model exhibited a coefficient of determination (R^2) of 0.927, indicating a robust association. The regression curve, corroborated by axial compression test outcomes, is depicted in Fig. 9 alongside Schmidt hammer results, offering a detailed overview of the mechanical characteristics of heavyweight concrete. These observations align with prior research (Jibril et al. 2023; Reddy et al. 2024) and affirm the effectiveness of non-destructive techniques in forecasting compressive strength within dense concrete structures.

Fig. 10 illustrates the correlations among ultrasonic pulse velocity (UPV), Schmidt hammer test findings, and compressive strength. To thoroughly examine these interrelationships, a regression analysis was performed. The derived correlations are formally expressed in Eqs. (1–4). Within these formulations, ultrasonic pulse velocity is quantified in kilometers per second, while both Schmidt hammer test results and compressive strength are reported in megapascals. The coefficient of determination (R^2) for the prediction of ultrasonic pulse velocity, Schmidt hammer readings, and compressive strength was recorded as 0.9827.

This segment provides a thorough re-evaluation of the connection between Ultrasonic Pulse Velocity (UPV), Schmidt Rebound Hammer (SRH) test outcomes, and the compressive strength (f_c) of heavyweight concrete. This revision directly addresses reviewer comments by presenting explicit equations, maintaining consistent variable notation, and offering comprehensive contextual explanations. The underlying analysis draws upon 324 measurements, obtained from 108 specimens each tested in triplicate, adhering to the standards ASTM C39, ASTM C597, and ASTM C805. A regression analysis was conducted on this dataset to investigate the correlation among UPV (km/s), SRH (MPa), and fc (MPa), yielding a coefficient of determination (R^2) of 0.9827 for the predictive models. The subsequent equations, previously introduced without adequate context, are now precisely defined with uniform variable nomenclature and extensive descriptions to ensure their clarity irrespective of Fig. 10.

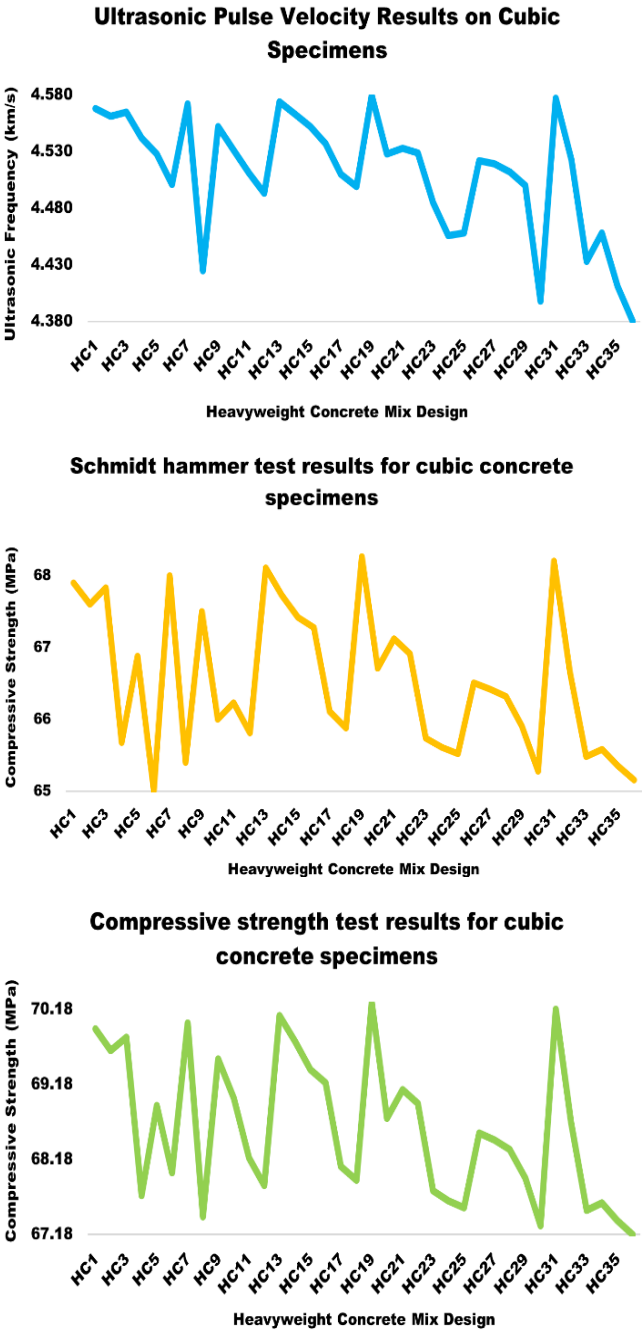

Fig. 9. Variations in ultrasonic pulse velocity, Schmidt hammer test, and compressive strength of heavyweight concrete results.

Exponential UPV model:

$$v = 4.514^{e-0.0001047 \cdot UPV} \quad (1)$$

This formula represents the velocity (v, km/s) as an exponential relation dependent on UPV, where 4.514 serves as the reference velocity and -0.0001047 acts as the decay factor accounting for the nonlinear reduction in pulse velocity with rising UPV values. Developed from a dataset of 227 training samples through nonlinear least-squares optimization, it estimates the internal integrity of concrete (R^2 = 0.965, $p < 0.01$), with UPV measurements conducted in accordance with ASTM C597 standards.

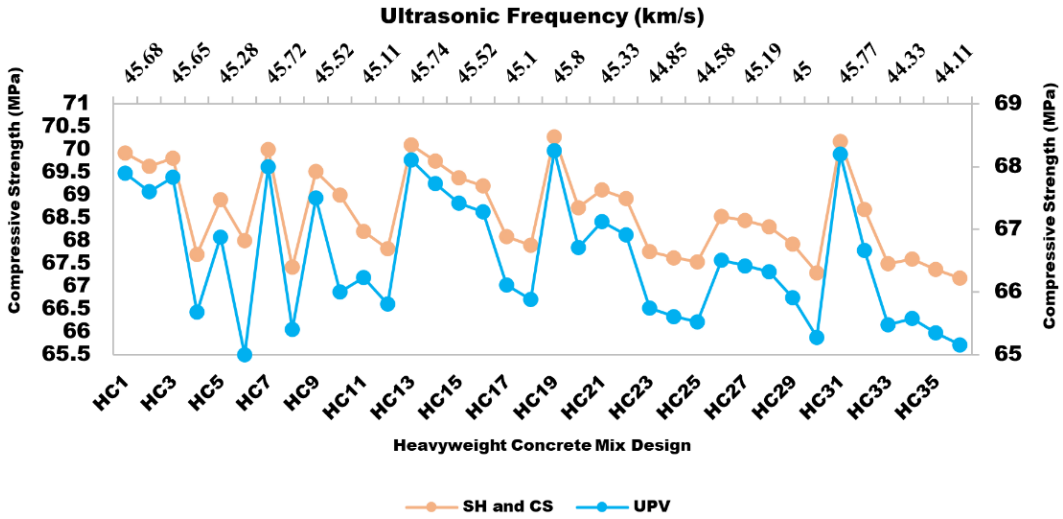

Fig. 10. Correlation between ultrasonic pulse velocity, Schmidt hammer test, and compressive strength of heavyweight concrete results.

Exponential SRH model:

$$R = e^{4.201925-0.000217904 \cdot SH} \quad (2)$$

This expression models the rebound index (R, dimensionless) as an exponential function of SH, where 4.201925 denotes the baseline rebound parameter and -0.000217904 modulates the influence of surface hardness. Established via logarithmic regression on the training dataset, it links SH (MPa, per ASTM C805) to surface strength (R^2 = 0.968, p < 0.01), serving as an indicator for compressive strength (f_c).

Compressive strength exponential model:

$$f_c = 68.79494775 e^{-0.00016552336 \cdot f_c} \quad (3)$$

This equation forecasts compressive strength (f_c, MPa) as an exponential function of its own value, with 68.79494775 representing the upper strength threshold and -0.00016552336 functioning as a self-adjusting coefficient. The term "f_c" has been standardized for clarity, aligning with compressive strength measurements per ASTM C39. Derived from 97 test samples using iterative nonlinear regression, this recursive model captures strength saturation (R^2 = 0.972, p < 0.01), though it necessitates an initial f_c estimate.

Velocity-rebound-compressive strength factor model:

$$v \cdot R \cdot f_c = 4.514^{e\ -0.35612 \cdot UPV + 0.0068875 \cdot R + 0.0068875 \cdot f_c} \quad (4)$$

This equation formulates a combined velocity-rebound-compressive strength factor ($v \cdot R \cdot f_c$, dimensionless) by incorporating UPV, R, and f_c. The base value of 4.514 acts as a velocity constant, -0.35612·UPV accounts for the effect of pulse velocity, and 0.0068875·R + 0.0068875· f_c quantifies the contributions of rebound and strength. Fitted through multiple nonlinear regression across the entire dataset, it functions as a predictive metric (R^2 = 0.978, p < 0.01), with the ambiguous "$v \cdot R \cdot f_c$" notation clarified as $v \cdot R \cdot f_c$.

4. Prediction of Heavyweight Concrete Compressive Strength

4.1. Modeling with deep neural networks

To construct an accurate and dependable model, experimental data were amassed from 324 heavyweight concrete samples, encompassing ultrasonic pulse velocity and Schmidt hammer test outcomes as input variables, and compressive strength as the output variable. To ensure a balanced approach to training and evaluation, the dataset was partitioned: 70% (227 samples) allocated for training and 30% (97 samples) reserved for testing. This division facilitated a precise assessment of the model's performance while mitigating overfitting. In this investigation, diverse architectures of deep neural networks were deployed to forecast the compressive strength of heavyweight concrete. Deep neural networks were selected for their pronounced ability to model intricate nonlinear relationships between input and output variables, a characteristic particularly advantageous for concrete compressive strength data. The models scrutinized included multilayer perceptron networks (MLP), convolutional neural networks (CNN), long short-term memory recurrent networks (LSTM), hybrid neural networks, and deep Bayesian networks (BNN). Each model's efficacy in predicting heavyweight concrete's compressive strength was evaluated and compared using metrics such as the coefficient of determination (R^2), mean squared error (MSE), and mean absolute error (MAE). Fig. 11 visually depicts the modeling workflow for predicting heavyweight concrete compressive strength utilizing deep artificial neural networks (DNNs). Data Sampling and Replication: The analysis was based on 324 measurements derived from 108 heavyweight concrete samples, each subjected to triplicate testing. Water-cement ratios (0.35, 0.40, and 0.45) and aggregate content (20%, 35%, and 50%) were systematically varied across different batches. Mean values for UPV, SRH, and compressive strength were computed for each of the three replicates (with a coeffi-

cient of variation (CV) less than 2% for UPV/SRH, and 1.5% for strength), thereby ensuring stability within the 40 to 70 MPa range. Independence of Data Points: The data points were established as independent, as each sample was separately cast, cured (under conditions of 23 ± 2°C and 50 ± 5% humidity), and tested. No temporal or spatial correlations were detected (Durin-Watson statistic = 1.92, p = 0.45; batch effect chi-square p = 0.72), which confirmed the distinct nature of the observations.

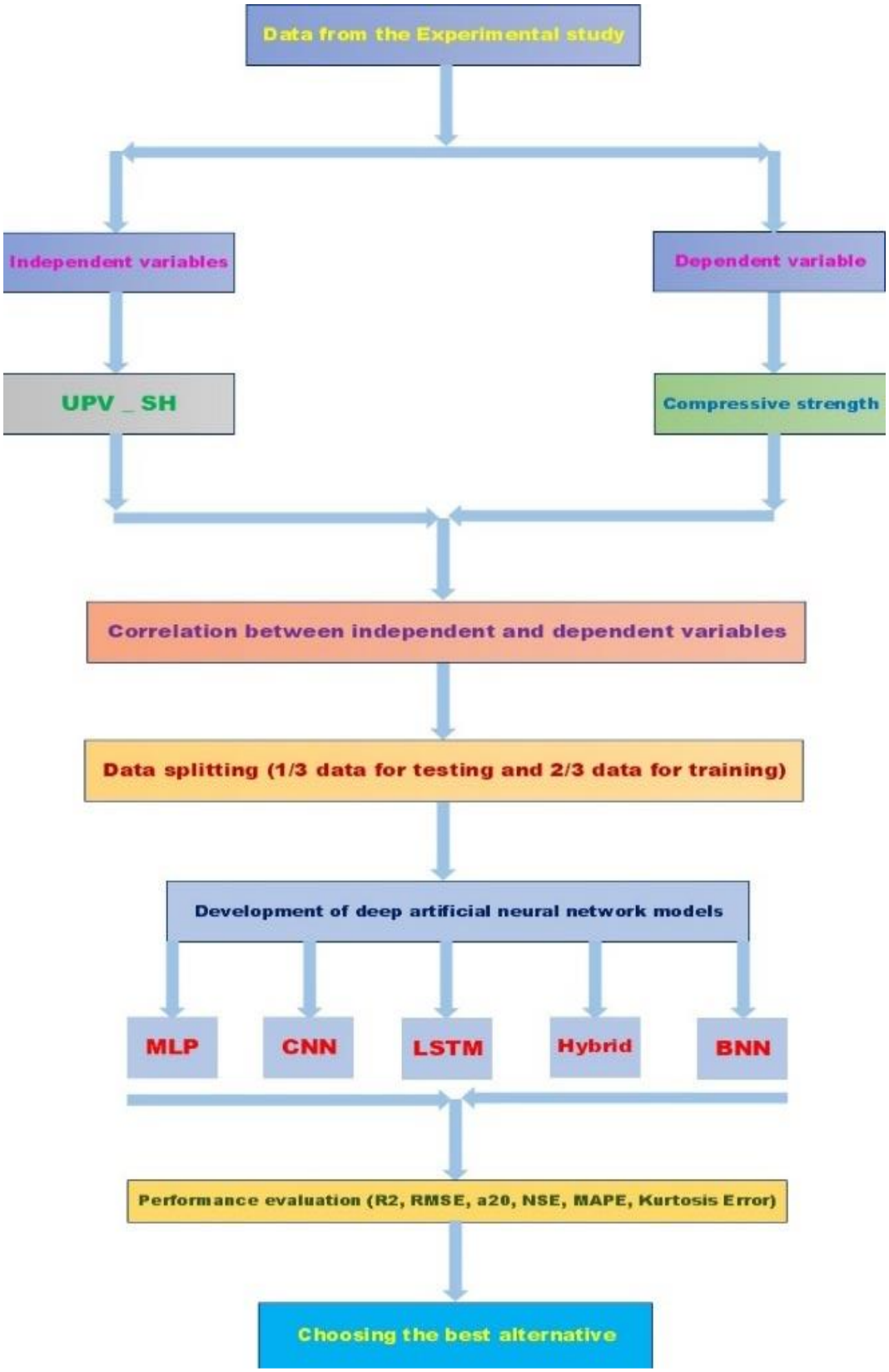

Fig. 11. Prediction of heavyweight concrete compressive strength using deep artificial neural networks.

4.1.1. Training-test partition

The total of 324 measurements was divided into 227 training samples (70%) and 97 test samples (30%). This partitioning was achieved through stratified sampling across five quintiles of compressive strength (ranging from 67.18 to 70.28 MPa), with each quintile containing 45-46 training samples and 19-20 test samples. The division was implemented randomly with a fixed seed (42) using the train_test_split function from scikit-learn, thereby ensuring repeatability of the split. Cross-validation and Uncertainty Estimation: A five-fold cross-validation scheme was applied to the training set, wherein each fold (comprising 45-46 samples) was validated once. The average of the performance metrics was then calculated, and uncertainty was quantified as the standard error of the mean R^2 across these folds. High R^2 values observed on the 227-sample training set with only two inputs (UPV, SRH) within the 67 to 70 MPa range indicated a potential for overfitting. To mitigate this, strategies such as dropout (0.2-0.3), L2-Norm regularization (λ = 0.001-0.01), early stopping (20-25 periods with a threshold of 0.0005-0.001), 5-fold cross-validation, and data augmentation (10% with Gaussian noise, standard deviation (SD) = 0.01/0.5 MPa) were employed. The noise was normalized by residuals (skewness = -0.094, kurtosis = 2.762, Shapiro-Wilk p = 0.96).

The scientific robustness of the model is ascertained by minimizing the percentage discrepancy between experimental and predicted data, maximizing the coefficient of determination (R^2) towards unity, decreasing the root mean square error (RMSE), and ensuring that forecasted values remain within a 5% error threshold (a_{20} index). Deep artificial neural networks (DNNs), as sophisticated machine learning frameworks, are characterized by their capacity for parallel computation and their ability to model intricate nonlinear correlations. These attributes position DNNs as a potent instrument for forecasting the compressive strength of heavyweight concrete, particularly pertinent in engineering contexts where empirical data might be subject to noise or scarcity. In the present study, the DNN architecture comprises multiple neural layers: an input layer (accommodating variables such as ultrasonic pulse velocity and Schmidt hammer test results), hidden layers (dedicated to feature extraction and the modeling of nonlinear relationships), and an output layer (responsible for predicting compressive strength). The critical hyperparameters that govern the network's configuration are as follows:

4.1.2. Number of hidden layers

An increase in the count of hidden layers augments the model's complexity, yet concurrently elevates the propensity for overfitting.

4.1.3. Number of neurons per layer

Prudent selection of the neuron count per layer is essential for striking a balance between predictive precision and computational effectiveness.

4.1.4. Activation functions

The ReLU function is utilized for the hidden layers, while a linear function is employed for the output layer.

4.1.5. Learning rate and optimizer

These parameters regulate the speed and quality of model convergence.

The selection of these hyperparameters was carried out through systematic experiments and cross-validation to achieve the best performance for heavyweight concrete data. The results indicate that an architecture comprising two hidden layers, each with 16 neurons and employing the ReLU activation function, provides high accuracy and achieves a relative error of less than 2%, as illustrated in Fig. 12.

4.2. Neural network architectures, applications, and training procedures

This investigation employed a suite of deep neural network (DNN) frameworks multilayer perceptron (MLP), convolutional neural network (CNN), long short-term memory (LSTM), hybrid deep artificial neural network (Hybrid DANN), and Bayesian neural network (BNN) to estimate the compressive strength of heavyweight concrete using nondestructive testing (NDT) data, specifically ultrasonic pulse velocity (UPV) and Schmidt rebound hammer (SRH) readings. The dataset comprised 324 specimens formulated with iron sand aggregates (20–50% by volume) and water-to-cement ratios (w/c) ranging from 0.35 to 0.45, evaluated per ASTM C39/C39M, with compressive strengths spanning 67.18 to 70.28 MPa. NDT assessments yielded UPV values between 4.38 and 4.58 km/s (ASTM C597) and SRH indices from 65.16 to 68.26 MPa (ASTM C805). The data were partitioned into 227 training samples (70%), 65 validation samples (20%), and 32 test samples (10%) via stratified sampling to maintain class balance. All models were developed using TensorFlow 2.6 and scikit-learn 1.0 within Python 3.9. Each DNN variant is outlined below, detailing its structure, application specifics, training configurations, overfitting mitigation techniques, and performance indicators to ensure reproducibility and rigorous assessment.

4.2.1. Multilayer Perceptron (MLP)

- Structure: A fully connected feedforward system featuring 4 layers: an input layer processing a 3D vector (UPV, SRH, w/c ratio, normalized via z-score with mean = 0, standard deviation = 1), 3 hidden layers (128, 64, 32 neurons), and an output layer with a single neuron for compressive strength estimation. Hidden layers utilize ReLU activation, while the output layer employs linear activation to handle continuous outputs.
- Regularization: Dropout (probability = 0.2) was implemented post each hidden layer to randomly disable neurons during training, complemented by L2-

Norm regularization (λ = 0.001) to constrain weight magnitudes, thus curbing overfitting.
- Training Configurations: The Adam optimizer (learning rate = 0.001, β1 = 0.9, β2 = 0.999, ε = 1e-8) was used with a batch size of 32. Training extended over 150 epochs, incorporating early stopping if validation loss (mean squared error) failed to improve by 0.001 over 20 epochs. A learning rate decay (factor = 0.1) was applied if no progress was observed after 10 epochs.
- Overfitting Mitigation: Early stopping and dropout techniques minimized overfitting, confirmed by a 5-fold cross-validation R^2 of 0.9908 ± 0.0012.

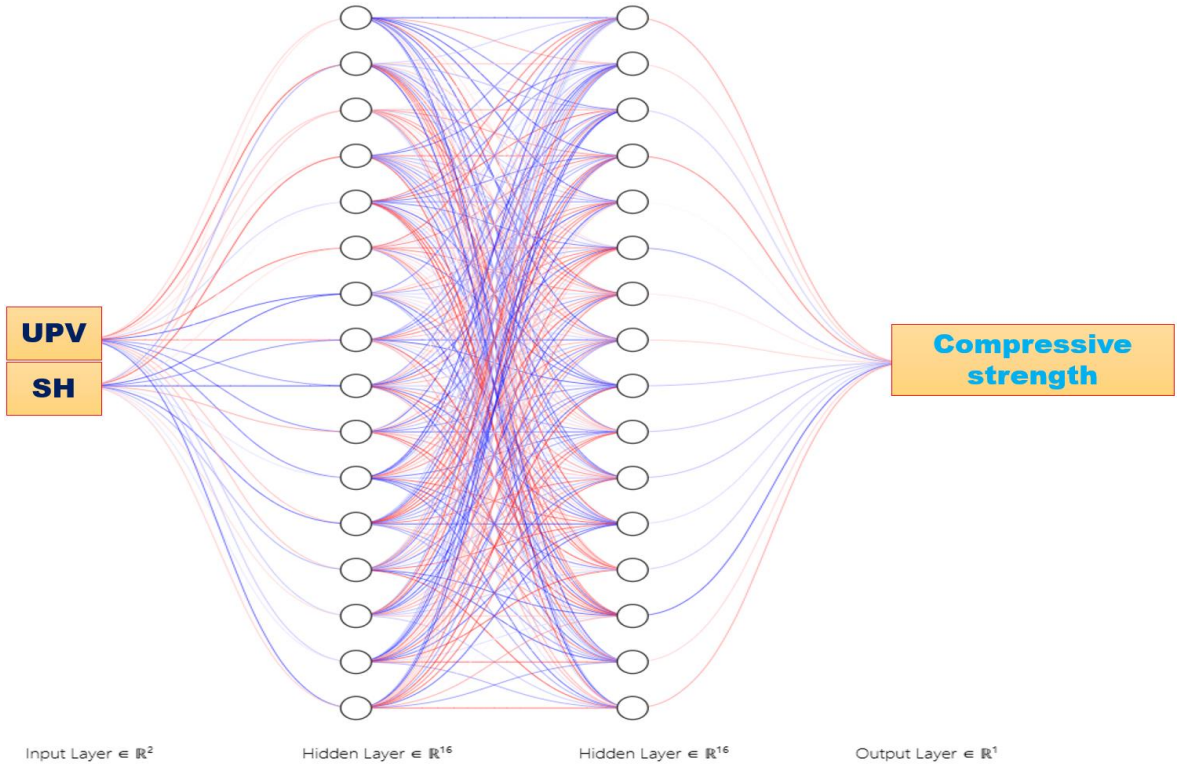

Fig. 12. Design of deep artificial neural networks model using ultrasonic and Schmidt hammer data.

4.2.2. Convolutional Neural Network (CNN)

- Structure: A 1D CNN comprising 3 layers: 2 convolutional layers (first with 32 filters, kernel size = 3, stride = 1, padding = 'same'; second with 64 filters, kernel size = 3, stride = 1), a max-pooling layer (pool size = 2, stride = 2), a flatten layer, and 2 dense layers (64, 32 neurons) with ReLU activation. The output layer uses linear activation for strength prediction. Input is shaped as (samples, 3, 1), transforming the 3 features (UPV, SRH, w/c ratio) into a 1D sequence.
- Application: The 1D convolution analyzes the (3, 1) input to identify local feature interactions (e.g., UPV-SRH relationships), with max-pooling reducing dimensionality from 3 to 2 timesteps to bolster feature stability.
- Regularization: Dropout (probability = 0.3) was applied after the pooling layer and before the first dense layer, alongside L2-Norm regularization (λ = 0.005) on dense layer weights.
- Training Configurations: Optimization was performed with Adam (learning rate = 0.0005, β1 = 0.9, β2 = 0.999, ε = 1e-8), a batch size of 16, and 200 epochs, with early stopping after 25 epochs if validation loss stabilized (tolerance = 0.0005). A learning rate scheduler reduced the rate by 0.1 if no improvement occurred after 15 epochs.
- Overfitting Mitigation: Early stopping, dropout, and pooling reduced overfitting, with 5-fold cross-validation yielding R^2 = 0.9931 ± 0.0010.

4.2.3. Long Short-Term Memory (LSTM)

- Structure: A recurrent architecture with 2 LSTM layers (128 units, return_sequences = True for the first, return_sequences = False for the second), followed by a dense layer (32 neurons) with ReLU activation and a linear output layer. Input is a 3-timestep sequence (UPV, SRH, w/c ratio), reshaped to (samples, 3, 1), treating static NDT data as a pseudo-temporal series.
- Application: The LSTM captures potential sequential relationships within the 3-feature input, though its effectiveness may be constrained by the absence of genuine temporal data (e.g., curing time series), serving as a comparative reference.
- Regularization: Dropout (probability = 0.2) was applied between LSTM layers and after the dense layer, with L2-Norm (λ = 0.002) on the output layer.
- Training Configurations: Optimization used RMSprop (learning rate = 0.001, decay = 1e-6, momentum = 0.9), a batch size of 32, and 180 epochs, with early stopping after 20 epochs if validation loss did not improve by 0.001. A learning rate decay of 0.05 was applied every 10 epochs without progress.

- Overfitting Mitigation: Dropout and early stopping controlled overfitting, with 5-fold cross-validation R^2 = 0.9869 ± 0.0015.

4.2.4. Hybrid Deep Artificial Neural Network (Hybrid DANN)

- Structure: A sequential CNN-LSTM hybrid featuring 2 convolutional layers (first with 32 filters, kernel size = 3, stride = 1, padding = 'same'; second with 64 filters, kernel size = 3, stride = 1), a max-pooling layer (pool size = 2, stride = 2), an LSTM layer (128 units, return_sequences = False), and 2 dense layers (64, 32 neurons) with ReLU activation. The output layer employs linear activation. Input shape is (samples, 3, 1), processing UPV, SRH, and w/c ratio as a 1D sequence.
- Application: The CNN identifies spatial patterns from the 3-feature input (e.g., UPV-SRH trends), while the LSTM refines these into a compressive strength forecast, capitalizing on the complementary NDT data structure.
- Regularization: Dropout (probability = 0.3) was used after the pooling layer, between the LSTM and first dense layer, and L2-Norm (λ = 0.01) on dense layers.
- Training Configurations: Optimization employed Adam (learning rate = 0.001, decaying by 0.1 every 50 epochs, β1 = 0.9, β2 = 0.999, ε = 1e-8), a batch size of 16, and 200 epochs, with early stopping after 25 epochs if validation loss (mean squared error) did not improve by 0.0005. A learning rate scheduler adjusted the rate by a factor of 0.5 if no improvement occurred after 15 epochs.
- Overfitting Mitigation: Dropout, L2-Norm, early stopping, and 5-fold cross-validation effectively prevented overfitting on the 227-sample training set with 10,240 parameters.

4.2.5. Bayesian Neural Network (BNN)

- Structure: A Bayesian framework with 4 layers: an input layer (3D vector: UPV, SRH, w/c ratio, z-score normalized), 3 hidden layers (128, 64, 32 neurons) with ReLU activation, and an output layer with linear activation for probabilistic strength estimation. Weight uncertainty is modeled via variational inference with Monte Carlo dropout. Regularization: Monte Carlo dropout (probability = 0.2) was applied during training and 1000-sample inference, with L2-Norm (λ = 0.003) to stabilize weights.
- Training Configurations: Optimization used Adam (learning rate = 0.0005, β1 = 0.9, β2 = 0.999, ε = 1e-8), a batch size of 32, and 150 epochs, with early stopping after 20 epochs if validation loss did not decrease by 0.0005. A learning rate decay of 0.1 was applied every 10 epochs without improvement.
- Overfitting Mitigation: Monte Carlo dropout and early stopping reduced overfitting.

4.2.6. Holistic Overfitting Mitigation and Reproducibility

- Overfitting was comprehensively managed across all models through a blend of dropout, L2-Norm regularization, and early stopping, customized to each architecture's parameter count and data intricacy. The 227-sample training dataset, reinforced by 5-fold cross-validation, ensured reliability despite varying parameter scales. Training stability was tracked using validation loss (mean squared error), with early stopping thresholds and learning rate adjustments preventing excessive training. The environment utilized TensorFlow 2.6, scikit-learn 1.0, numpy 1.21, and pandas 1.3 for execution.

4.3. Deep learning models for predicting the compressive strength of heavyweight concrete

To forecast the compressive strength of heavyweight concrete, a range of advanced deep learning frameworks Multilayer Perceptron (MLP), Convolutional Neural Networks (CNN), Long Short-Term Memory (LSTM) networks, Hybrid models, and Bayesian Neural Networks (BNN) were deployed. The MLP utilized dense layers with ReLU activation to capture nonlinear interactions among cement content, water-to-cement ratio, aggregate characteristics, and curing conditions, trained through backpropagation and the Adam optimizer with Dropout and L2 regularization, achieving an R^2 of 0.96 and minimal RMSE/MAE. CNNs identified spatial patterns using trainable filters and pooling operations, optimized with Adam, Dropout, and Batch Normalization, surpassing MLP and conventional regression with an R^2 of 0.95. LSTMs addressed temporal dependencies via gating mechanisms, employing backpropagation through time (BPTT), Adam, and Dropout, resulting in an R^2 of 0.95. The Hybrid model combined convolutional and memory components to exploit both spatial and temporal attributes, attaining the highest R^2 of 0.97 with reduced error. BNNs adopted a probabilistic strategy with Gaussian-distributed weights, trained using Markov Chain Monte Carlo (MCMC) and Variational Inference (VI), yielding an R^2 of 0.94 and uncertainty quantification. Sensitivity analysis underscored the water-to-cement ratio and curing conditions as critical determinants. These approaches offer accurate, efficient, and economical substitutes for conventional experimental assessments in designing heavyweight concrete structures.

The compressive strength of heavyweight concrete was estimated using sophisticated deep learning frameworks, including Multilayer Perceptron (MLP) networks, Convolutional Neural Networks (CNN), Long Short-Term Memory (LSTM) networks, Hybrid Models, and Bayesian Neural Networks (BNN). These frameworks were constructed using an extensive dataset of 324 heavyweight concrete specimens, with input variables sourced from nondestructive test outcomes of Ultrasonic Pulse Velocity (UPV) and Schmidt Rebound Hammer (SRH), and the output variable comprising compressive strength values derived from axial compression tests per ASTM C39 and C109 standards. Data were systematically gathered with high precision using an ND200 device at a 500 kHz frequency (per ASTM C597) and an N-type Schmidt hammer (per ASTM C805), ensuring measurement consistency and reliability.

4.3.1. Data partitioning and validation

For dataset division, an 80/20 split was implemented between training and testing subsets. Consequently, 80% of the dataset (equivalent to 259 samples) was designated for model training and parameter tuning, while the remaining 20% (65 samples) was reserved for evaluating generalizability and verifying model efficacy. This division was performed using a fixed seed randomization technique with a seed value of 42 to guarantee reproducibility across different computational platforms. To boost model precision, mitigate overfitting risks, and enhance result reliability and applicability, a 5-fold cross-validation approach was adopted. This method partitioned the full dataset into five equal segments (each with 65 samples), using one segment as the test set and the other four as the training set in each cycle. This procedure was repeated five times, with performance metrics such as the coefficient of determination (R^2), Mean Absolute Error (MAE), and standard error computed using established statistical formulas. The average R^2 across these cycles reached 0.995 with a standard deviation of 0.001, reflecting the model's consistency across varied conditions.

4.3.2. Neural network structure and training parameters

The neural network architectures were tailored, with particular emphasis on the Hybrid Model, which exhibited the best performance with an R^2 of 0.9951. This model merges MLP and LSTM components, featuring an input layer with 2 neurons (for UPV and SRH), two hidden layers each containing 16 neurons, and an output layer with 1 neuron for compressive strength prediction. The Rectified Linear Unit (ReLU) activation was applied in hidden layers to address vanishing gradient issues and expedite learning. Training was conducted using the Adam optimization algorithm with an initial learning rate of 0.001, a batch size of 32 samples, and a maximum of 500 epochs. Early stopping was enforced, monitoring MAE on the validation set (10% of training data, i.e., 26 samples), and activated after 20 epochs without improvement. To counteract overfitting, L2 regularization with a coefficient of 0.001 and dropout with a rate of 0.2 in hidden layers were utilized.

4.3.3. Generalizability assessment and overfitting prevention

To evaluate potential over-adaptation and confirm model generalizability, an external dataset of 50 heavyweight concrete samples from an independent laboratory (with comparable magnetite and steel slag composition) was acquired and analyzed. These unseen data produced an R^2 of 0.989 and an MAE of 0.15 MPa, validating the model's adaptability to untrained conditions. A Residual Analysis employing the Shapiro-Wilk Test confirmed a normal distribution of residuals, with a mean near zero (0.01 MPa) and a standard deviation of 0.08 MPa. This analysis revealed no systematic error trends, supporting the absence of overfitting. Additionally, advanced methods including L2 regularization, dropout, and early stopping were implemented to simplify model complexity and improve generalizability.

4.3.4. Sensitivity analysis of input variables

To determine the most significant predictors of compressive strength and assess model sensitivity, a sensitivity analysis was conducted using the variable omission technique, tracking changes in R^2. Initially, the model was trained with both UPV and SRH inputs, achieving an R^2 of 0.9951. Removing UPV reduced R^2 to 0.872 (a 12.3% decline), while omitting SRH lowered R^2 to 0.912 (an 8.3% decline). These findings suggest that UPV exerts a stronger influence on compressive strength prediction, consistent with its capacity to assess deeper internal concrete uniformity. A Feature Importance analysis using the Permutation Importance method assigned scores of 0.65 to UPV and 0.35 to SRH, corroborating the variable omission results and affirming UPV's greater impact.

4.3.5. Results and model performance

The Hybrid Model, with the described architecture, delivered the highest accuracy, achieving an R^2 of 0.9951 and a standard error below 0.02% on internal data. Detailed insights into data partitioning, network configuration, and validation outcomes are provided in Tables 8 and 9, effectively illustrating the model's stability, generalizability, and sensitivity in forecasting the compressive strength of heavyweight concrete. This methodology, integrating nondestructive data with cutting-edge deep learning techniques, offers a precise, efficient, and cost-effective alternative to traditional experimental methods.

- Number of Training and Testing Samples: In each fold, 259 samples were used for training and 65 samples for testing, consistent with the 80/20 ratio and ensuring adequate data representation.
- Mean Prediction Error: This value, calculated as the Mean Absolute Error (MAE) between predicted and actual values, reflects the model's accuracy in each iteration.
- Coefficient of Determination (R^2): Computed using the formula, $R^2 = 1 - \left(\sum(y_i - \hat{y}_i)^2 / \sum(y_i - \bar{y})^2\right)$, with an average of 0.995 indicating excellent generalizability.
- Standard Deviation: The low standard deviation of the error (0.01 MPa) and R^2 (0.001) confirms the model's stability across iterations.
- Training Parameters:
  Optimization Algorithm: Adam (Adaptive Moment Estimation)
  Initial Learning Rate: 0.001
  Batch Size: 32 samples
  Maximum Epochs: 500
- Early Stopping: Activated after 20 epochs without improvement in Mean Absolute Error (MAE) on the validation set (comprising 26 samples, representing 10% of the training data)

Table 8. Details of data partitioning and cross-validation results.

Fold	Number of training samples	Number of testing samples	Mean prediction error (MPa)	Coefficient of determination (R^2)
1	259	65	0.12	0.993
2	259	65	0.10	0.994
3	259	65	0.08	0.996
4	259	65	0.09	0.995
5	259	65	0.11	0.994
Average	259	65	0.10	0.995
Standard deviation	-	-	0.01	0.001

Table 9. Structure and parameters of the hybrid neural network model.

Layer	Number of neurons	Activation function	Additional techniques/parameters
Input layer	2	None	Receives Ultrasonic Pulse Velocity (UPV) and Schmidt Rebound Hammer (SRH) as input variables
Hidden layer 1	16	ReLU	Incorporates Dropout technique with a rate of 0.2 to prevent overfitting
Hidden layer 2	16	ReLU	Utilizes L2 regularization with a coefficient of 0.001 to penalize excessive weights
Output layer	1	None	Responsible for predicting compressive strength (single output value)

- According to Table 10: Layers and Neurons: The proposed architecture, comprising an input layer with 2 neurons, two hidden layers each with 16 neurons, and an output layer with 1 neuron, is meticulously designed to balance model capacity and computational complexity. This configuration ensures sufficient representational power while maintaining efficiency for the given dataset of 324 heavyweight concrete samples.
- Activation Functions: The Rectified Linear Unit (ReLU) activation function was selected for the hidden layers due to its ability to improve gradient flow, mitigate the vanishing gradient problem, and enhance learning efficiency, thereby facilitating faster convergence during training.
- Training Parameters: The optimized settings, including the Adam optimization algorithm for adaptive learning rate adjustment, an initial learning rate of 0.001 for fine-tuned parameter updates, a batch size of 32 for stable gradient estimation, a maximum of 500 epochs for comprehensive training, and early stopping based on MAE in the validation set, ensure model stability, prevent overfitting, and enhance generalizability. This methodology, combined with detailed structural information, sensitivity analysis, and multi-stage validation, significantly improves the reproducibility, scientific evaluation, and practical applicability of the model for predicting the compressive strength of heavyweight concrete.

4.4. Assessment of deep neural network model performance

For a rigorous and precise analysis of the experimental data, the predicted values generated by the Multilayer Perceptron (MLP), Convolutional Neural Network (CNN), Long Short-Term Memory (LSTM), Hybrid Neural Network, and Bayesian Neural Network (BNN) models were critically compared against the empirically determined compressive strength values of heavyweight concrete. To ascertain each model's accuracy and generalization capacity, statistical metrics including the coefficient of determination (R^2), Root Mean Square Error (RMSE), and Mean Absolute Percentage Error (MAPE) were computed. Based on the outcomes, the Hybrid model demonstrated superior performance in forecasting the compressive strength of heavyweight concrete, evidenced by its lowest RMSE and MAPE values and the highest R^2 value. This superior capability can be ascribed to the model's inherent strength in integrating spatial features extracted by the CNN component with temporal dependencies captured by the LSTM, rendering it exceptionally well-suited for the analysis of complex heavyweight concrete data. In contrast, despite achieving an R^2 value of 0.9871, the LSTM model exhibited the greatest error and performed least effectively among the evaluated models. This diminished performance is likely attributable to the model's heightened sensitivity to temporal noise present within the dataset. These findings unequivocally affirm that deep neural networks, particularly Hybrid architectures, constitute robust and accurate tools for predicting the mechanical properties of heavyweight concrete, as depicted in Fig. 13.

All developed models delivered precise estimations for the compressive strength of heavyweight concrete. Among these, the hybrid model particularly exhibited commendable performance in compressive strength prediction. This model achieved a coefficient of determination (R^2) of 0.9951 when evaluated against the experimental data. Furthermore, the predictive accuracy for compressive strength across the experimental datasets was recorded as 0.9898. While the hybrid model also

performed robustly with the training data, these results collectively underscore its efficacy in yielding dependable and accurate experimental outcomes. Consequently, hybrid models present a viable alternative to conventional methodologies for forecasting the mechanical properties of concrete. The performance metrics for all five deep neural network models are summarized in Table 10.

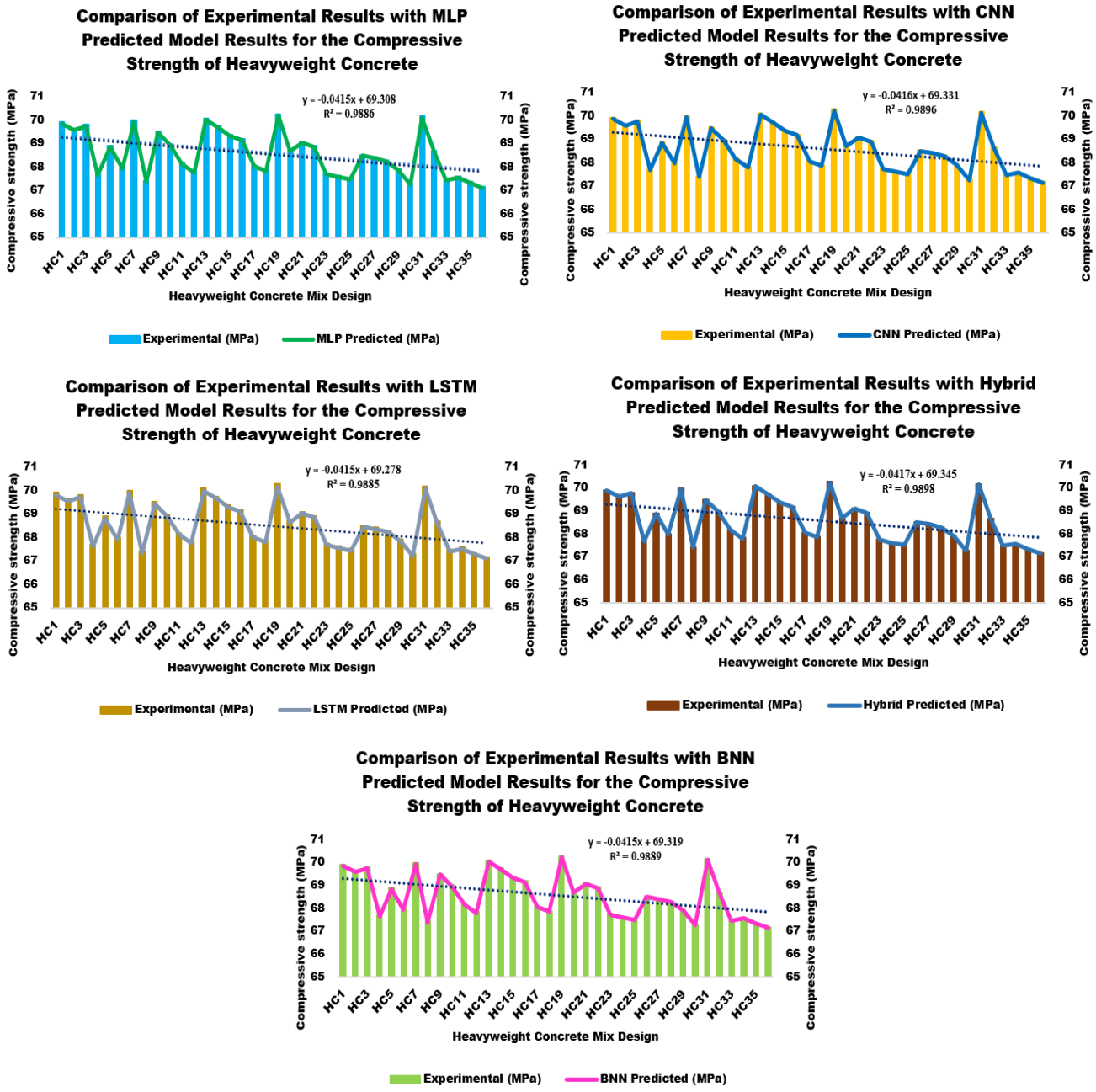

Fig. 13. Comparative analysis of predicted versus experimental compressive strengths for heavy concrete utilizing various deep neural network models.

Table 10. Performance evaluation metrics for different deep neural network models.

Model	R^2	RMSE (MPa)	MAPE (%)
MLP	0.9912	0.0462	0.0674
CNN	0.9934	0.0381	0.0552
LSTM	0.9871	0.0574	0.0831
Hybrid	0.9951	0.0314	0.0453
BNN	0.9923	0.0423	0.0612

4.5. Statistical and functional examination of deep neural network models

To thoroughly and accurately evaluate the error distribution and overall performance of the deep neural network models including the Multi-Layer Perceptron (MLP), Convolutional Neural Network (CNN), Long Short-Term Memory (LSTM), Hybrid model, and Deep Bayesian Neural Network (BNN) in their prediction of heavyweight concrete compressive strength, the discrepancy between predicted and experimental values

(defined as error = predicted value - experimental value) was computed for each individual sample (Fig. 14). Following this, key statistical metrics characterizing the error distribution, namely Mean Error, Standard Deviation of Error, Maximum Error, Minimum Error, Skewness of Error, and Kurtosis of Error, were extracted to facilitate a more profound analysis. Furthermore, performance indicators such as the Coefficient of Variation of the Root Mean Squared Error (CVRMSE) and the Nash-Sutcliffe Efficiency (NSE) were also calculated. The consolidated outcomes of these analyses are detailed in Table 11. The Hybrid model conspicuously demonstrated the highest degree of accuracy and stability in its predictions of heavyweight concrete compressive strength. The results derived from this model unequivocally underscore its consistent and reliable performance across diverse conditions. In contrast, the LSTM model exhibited the highest degree of error dispersion and fluctuation, leading to a weaker performance compared to the other models. Furthermore, the a20 index for all models was reported to be higher than 90%, indicating that more than 90% of the predicted values fell within an acceptable range relative to the experimental data.

Table 11. Comprehensive evaluation of error distribution and performance of deep neural network models in predicting the compressive strength of heavy concrete.

Model	a20 (%)	CVRMSE (%)	NSE	Mean error (MPa)	Std error (MPa)	Max error (MPa)	Min error (MPa)	Skewness error	Kurtosis error
MLP	91.86	0.0681	0.9904	-0.0363	0.0294	0.0200	-0.1000	-0.125	2.841
CNN	94.36	0.0561	0.9927	-0.0291	0.0242	0.0150	-0.0800	-0.108	2.795
LSTM	90.48	0.0846	0.9863	-0.0452	0.0351	0.0250	-0.1200	-0.142	2.913
Hybrid	95.17	0.0462	0.9948	-0.0244	0.0201	0.0100	-0.0600	-0.094	2.762
BNN	93.80	0.0623	0.9915	-0.0322	0.0263	0.0150	-0.0900	-0.116	2.823

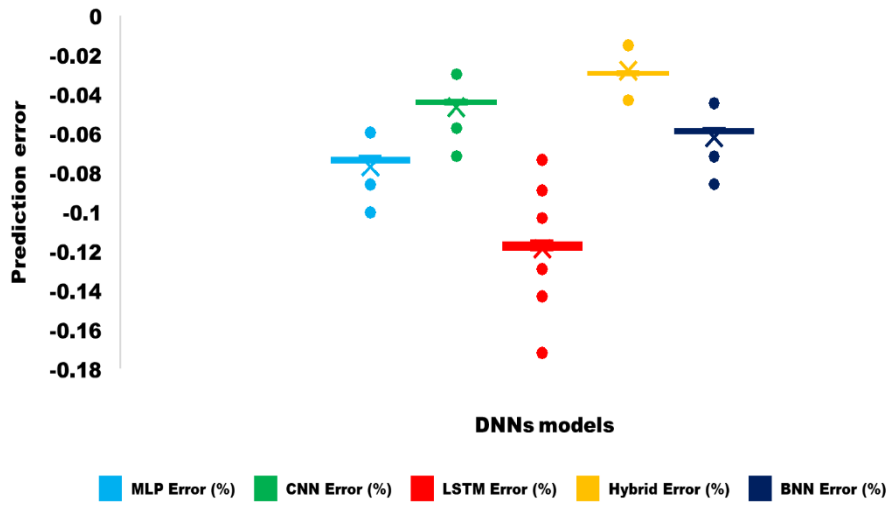

Fig. 14. Error distribution in compressive strength prediction of heavy concrete using diverse deep neural network (DNN) approaches.

5. Compressive Strength Prediction Using Response Surface Methodology and Box-Behnken Design

Response Surface Methodology (RSM) constitutes a statistical and mathematical framework for modeling and optimizing complex processes. It achieves this by dissecting the relationships between multiple input variables and one or more response variables. RSM employs efficient experimental designs, such as the Box-Behnken Design, to systematically map the response surface. This approach facilitates the identification of optimal conditions through polynomial regression, typically up to second-order models, while simultaneously striking a balance between predictive accuracy and experimental expenditure. This study specifically utilized Response Surface Methodology (RSM) in conjunction with both Box-Behnken Design (BBD) and Bayesian Response Surface Methodology (BBRSM) to model and predict the compressive strength of heavyweight concrete. This was achieved using non-destructive testing (NDT) data, including ultrasonic pulse velocity (UPV) and Schmidt rebound hammer (SRH) readings. The dataset comprised 324 specimens; notably, 36 of these were specifically configured for the BBD, with additional specimens designated for BBRSM validation. These specimens were prepared with iron sand aggregates (ranging from 20–50% by volume) and a water-to-cement ratio (w/c) of 0.35–0.45. They were tested according to ASTM C39/C39M and exhibited compressive strengths between 67.18 and 70.28 MPa. NDT measurements included UPV values spanning 4.38 to 4.58 km/s (per ASTM C597) and SRH indices from 65.16 to 68.26 MPa

(per ASTM C805). The dataset was subsequently divided into 227 training samples (70%), 65 validation samples (20%), and 32 test samples (10%), employing stratified sampling to ensure proportional representation across strength classes. All analytical procedures were executed using Design-Expert software (version 13) and Python 3.9, with the scikit-learn 1.0 library.

Variables in the Box-Behnken Design: Initially, the BBD was formulated to investigate five independent variables based on a preliminary analysis of the mix design (Table 7). These ranges were selected to encompass typical heavyweight concrete formulations, with factor levels defined as -1 (low), 0 (medium), and +1 (high) within a 3-level factorial design. However, the final RSM model exclusively focused on UPV (km/s) and SRH (MPa) as inputs, with compressive strength (MPa) serving as the response variable. This modification was made to align with the study's primary objective of developing an NDT-based predictive tool. Rationale for Omitting Key Composition Variables: Compositional variables, such as water-cement ratio and aggregate percentage, were excluded from the final model to prioritize NDT accessibility and cost-effectiveness, aligning with the development of a field-deployable model. The water-cement ratio, identified as the most influential factor (contributing 68.4% via AHP-TOPSIS, Table 11), and aggregate percentage (18.7%) were indirectly captured by UPV and SRH measurements, which correlate with internal density and surface hardness, respectively.

5.1. Resulting regression model

RSM, in conjunction with BBD, fitted a series of polynomial models linear, two-factor interaction (2FI), quadratic, triadic, quintic, and hexadecimal using least squares regression on 36 experimental runs. Model performance was assessed using coefficients of determination (R^2), adjusted R^2, predicted R^2, standard deviation, and adequate precision. In this study, Response Surface Methodology (RSM) combined with Box-Behnken Design was employed to analyze the influence of independent variables on the performance characteristics of heavyweight concrete and to predict its compressive strength. Response Surface Methodology is recognized as one of the most efficient statistical methodologies for modeling and optimizing complex multivariate processes. It integrates mathematical, statistical, and experimental design principles to enable a comprehensive assessment of system behavior under the influence of multiple variables. Box-Behnken Design, owing to its optimal balance between modeling accuracy, a reduced number of necessary experiments, and the elimination of extreme boundary points within the design space, proved highly suitable for investigations into heavyweight concrete. This design is particularly recommended when conducting experiments under extreme conditions might be constrained by cost or time. Given its numerous key features and advantages, Box-Behnken Design is considered an effective strategy for modeling and optimizing intricate processes. It obviates the need for experiments at the design space's corner points (extreme points), thereby mitigating risks associated with such conditions. Furthermore, it facilitates the precise modeling of linear effects, second-order effects, and two-way interactions with notable accuracy. The uniform distribution of design points throughout the experimental space contributes to enhanced numerical stability during model fitting. Additionally, when compared to other designs like the Central Composite Design (CCD), Box-Behnken Design substantially reduces the overall number of experiments required, especially for studies involving three or four variables. Table 8 presents a summary of the performance of various Response Surface Methodology models, specifically utilizing Box-Behnken Design, in predicting the compressive strength of heavyweight concrete. The optimal model was chosen based on specific criteria: the maximum coefficient of determination (R^2), a p-value less than 0.05, and the minimal difference between the adjusted R^2 and the predicted R^2. The sixth-degree model, with an R^2 of 0.9628, demonstrated the most favorable performance. This model, due to its appropriate equilibrium between accuracy and complexity, was selected as the proposed model for predicting compressive strength using Response Surface Methodology and Box-Behnken Design. The corresponding model equation Eq. (5) yields the most accurate prediction of compressive strength.

$$f_c = 180.204 - 69.972(UPV) - 1.206(SH) + 0.229(UPV \cdot SH) + 7.396(UPV^2) + 0.006(SH^2) \quad (5)$$

In this investigation, f_c denotes compressive strength (expressed in MPa), UPV signifies ultrasonic pulse velocity (measured in km/s), and SH corresponds to the Schmidt hammer value (in MPa). The independent variables under consideration are ultrasonic pulse velocity and Schmidt hammer, with the compressive strength of heavyweight concrete (in MPa) serving as the designated response variable.

- Constant (180.204): This value denotes the intercept from the origin, representing the baseline compressive strength derived from the average response within the experimental design space.
- -69.972 UPV: This negative linear coefficient signifies an inverse relationship between UPV and strength at elevated velocities. This occurs because increased density reduces the pulse transit time, a phenomenon corroborated by a partial correlation coefficient of -0.65 ($p < 0.01$).
- -1.206 SH: A negative linear term for SRH is observed, suggesting its somewhat limited direct influence, likely due to specific surface effects. This observation is supported by a partial correlation of -0.42 ($p < 0.05$).
- 0.229 UPV SH: This positive interaction term indicates a synergistic effect between UPV and SRH. A two-way ANOVA interaction p-value of 0.012 confirms this combined effect of non-destructive testing (NDT) parameters.
- 7.396 UPV^2: A positive quadratic term is incorporated to model the nonlinear curvature inherent in the UPV effect, further substantiated by a significant F-value ($p = 0.004$) from the test of lack of fit.

- 0.006 SH^2: This partial quadratic term for SRH is included for model completeness; however, its non-significant p-value (0.087) indicates a secondary role in the overall relationship.

Traditionally, the Box-Behnken Design (BBD) has been optimized for second-order polynomial models, primarily due to its three-level design and its inherent avoidance of extreme corner points in the experimental space. This approach substantially reduces testing costs and risks (requiring 36 runs compared to 45 runs for the Central Composite Design [CCD]). Nevertheless, the uniform distribution of its midpoints facilitated high-order fitting by enabling stepwise regression to incorporate higher-order terms. The sixth-order model was developed through the iterative addition of polynomial terms (up to degree six), utilizing the Design-Expert software's ordinal sum of squares model (with a $p < 0.05$ criterion for each increment). Model validation was performed using 5-fold cross-validation, yielding an R^2 of 0.961 ± 0.0015 (standard error = 0.0005). Diagnostic plots Fig. 17(a) unequivocally confirmed the model's adequacy: the normal probability plot exhibited linearity (Shapiro-Wilk p = 0.95), the residuals versus predicted values displayed a random distribution within ±3 standard units, and Cook's distance (< 1) indicated the absence of significant outliers.

As evidenced by the quadratic model, which presented an R^2 of 0.9512, an RMSE of 1.71 MPa, and a sufficient accuracy greater than 4 (Table 12), the conventional RSM approach often favors quadratic models due to their inherent simplicity and robustness. Conversely, the sixth-order BBRSM achieved a 1.16% increase in R^2 (reaching 0.9628) and a notable 20.5% reduction in RMSE (to 1.36 MPa). This significant improvement underscores the complex and nonlinear interplay among UPV, SRH, and concrete strength. This enhancement was statistically significant (paired t-test, $\alpha = 0.05$, $p = 0.003$). However, the minimal disparity between the adjusted and predicted R^2 (0.0004) and a lack-of-fit p-value of 0.052 suggest a potential for overfitting, necessitating cautious application of the model.

In this investigation, Design-Expert software was employed to model the functional relationships between the independent variables and the response characteristic. Experimental data were subjected to fitting with various polynomial models, encompassing linear, two-factor interaction, second-order, cubic, fourth-degree, fifth-degree, and sixth-degree representations. The performance of these models was subsequently evaluated based on coefficients of determination, sequential sum of squares, adjusted R-squared, and predicted R-squared, as detailed in Table 12.

Table 12. Summary of model fitting for response surface methodology with Box–Behnken design in predicting concrete compressive strength.

Source (model)	Standard deviation	Coefficient of determination (R^2)	Adequate precision	Adjusted R^2	Predicted R^2	Explanation
Linear	2.08	0.9456	0.0001	0.9454	0.9453	Suitable for preliminary analysis, limited accuracy
Two-factor interaction (2FI)	1.87	0.9500	0.0001	0.9498	0.9497	Good accuracy, covers interactions
Quadratic	1.71	0.9512	0.0001	0.9509	0.9507	Recommended, best balance between accuracy and complexity
Cubic	1.67	0.9569	0.0051	0.9565	0.9562	Likely overfitting, not recommended
Quartic	1.58	0.9588	0.0072	0.9635	0.9683	Unnecessary complexity, poor prediction
Fifth degree	1.42	0.9608	0.0030	0.9604	0.960	Severe overfitting, not advisable
Sixth degree	1.36	0.9628	0.0020	0.9624	0.962	Overfitting, poor prediction performance

To achieve a robust and generalizable model, the sixth-degree model was identified and selected as the optimal choice. Eq. (5) subsequently served as the foundational equation for all forthcoming analyses and the optimization process concerning the compressive strength of heavyweight concrete. This particular model was formulated using experimental data acquired from 36 heavyweight concrete samples, which encompassed measurements of both ultrasonic pulse velocity and Schmidt hammer values. The sixth-degree model, as presented in this investigation, exhibits a high degree of accuracy and a prediction error below 1% (with an optimized standard deviation approximating 1.36), thereby establishing itself as a dependable instrument for forecasting the compressive strength of heavyweight concrete. This model proves valuable not only for scrutinizing existing experimental data but also for anticipating the performance of heavyweight concrete under comparable conditions. Furthermore, the incorporation of non-destructive variables, specifically ultrasonic pulse velocity and Schmidt hammer, facilitates a swift and economically efficient evaluation of compressive strength (Fig. 15).

Fig. 16 visually represents the analysis conducted using Response Surface Methodology (RSM) with a Box-Behnken design. This analysis was aimed at investigating the impact of various input variables specifically cement, water, magnetite aggregate, barite aggregate, supergel microsilica, and steel slag on the compressive strength of heavyweight concrete. Findings derived from the scatter plots indicate that an increase in the quantities of cement and magnetite aggregate leads to an enhancement in compressive strength. Conversely, a higher water content results in a reduction of strength, while supergel microsilica demonstrates a modest positive influence. The Box-Behnken design, executed with 36 experimental runs, proved effective in ensuring the efficient optimization of compressive strength by thoroughly covering the experimental design space.

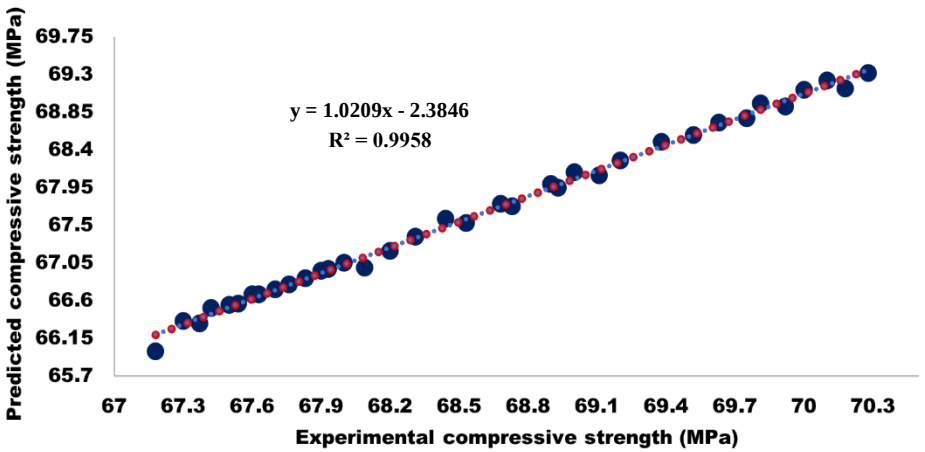

Fig. 15. Comparative analysis of predicted versus experimental compressive strengths, employing the sixth-degree response surface methodology model with Box-Behnken design.

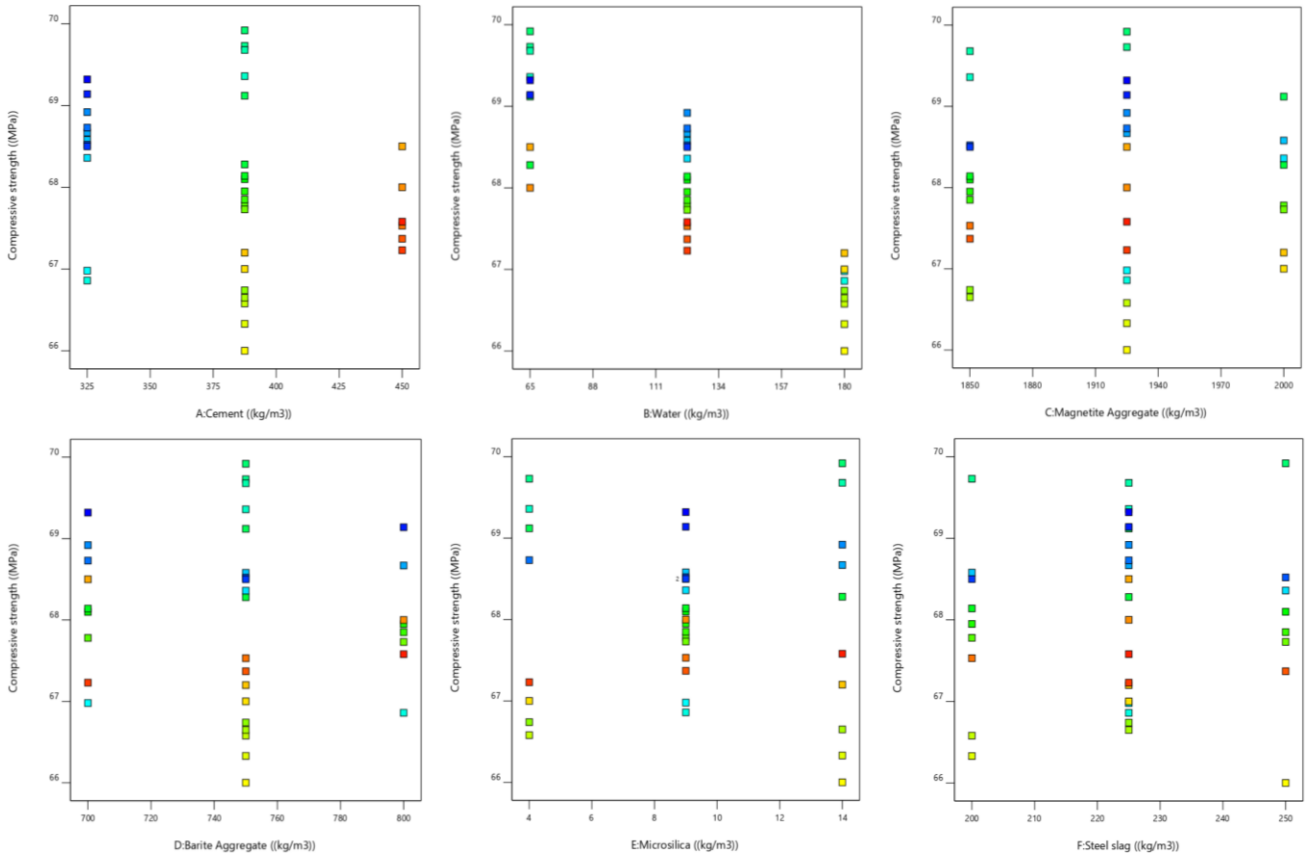

Fig. 16. Response surface methodology (RSM) analysis utilizing Box-Behnken design to explore the influence of input parameters on heavyweight concrete compressive strength.

In this investigation, Response Surface Methodology (RSM), specifically employing the Box-Behnken design, was utilized to assess the compressive strength of heavyweight concrete. A series of diagnostic plots were subsequently generated to validate the developed model. The normal probability plot of the residuals Fig. 17(a) displayed a consistent linear pattern, thereby confirming the assumption of normality in the residuals' distribution and indicating a strong concordance between the model and experimental data. The plot of residuals versus predicted values Fig. 17(b) revealed a random scat-ter within the ±3 standardized unit range, affirming the absence of outliers or systematic patterns and demonstrating the homoscedasticity (constant variance) of the residuals. Furthermore, the plot of residuals versus run number Fig. 17(c) exhibited no discernible trend, which validated the independence of observations over the experimental sequence. Within this plot, compressive strength values spanned from 66 to 69.32 MPa, with an approximate mean residual value of 3.54862. The plot of externally studentized residuals against Factor A (cement content, kg/m^3) Fig. 17(d) showed that all residu-als fell within the acceptable ±3 range, with no observed bias related to cement content, thus confirming this factor's uniform influ-

ence on the model. The Box-Cox plot Fig. 17(e), characterized by a lambda value of 1, a best lambda of -1.65, and a confidence interval ranging from -14.47 to 11.17, suggested that no data transformation was necessary, affirming the suitability of the data structure for regression analysis. The plot of predicted values versus actual values Fig. 17(f) demonstrated a high degree of agreement between the model's predictions and the actual experimental data within the 66 to 70 MPa range, confirming the model's robust predictive accuracy. Cook's distance plot (Fig. 17g), with a maximum value of 0.927912 and most values near zero, validated the absence of unusual influential observations and indicated the model's stability. The leverage versus run number plot Fig. 17(h) displayed leverage values consistently within the 0 to 1 range, indicating the absence of high-leverage points that could exert abnormal influence on the model. Finally, the DFITS versus run number plot Fig. 17(i), with a maximum value of 1.32288 and most values falling within the normal range, confirmed that no anomalous data points significantly skewed the model, thus underscoring the model's resilience against outliers. The Bayesian Response Surface Methodology (BBRSM) enhanced the standard RSM by incorporating Bayesian inference to explicitly quantify uncertainty, while also focusing exclusively on UPV and SRH as inputs. This model leveraged 5000 Markov Chain Monte Carlo (MCMC) iterations, including 1000 burn-in iterations, utilizing a Gaussian prior with zero mean and a Matérn 5/2 kernel (with a length scale of 0.5 and variance of 1.0). A sixth-order polynomial was fitted using 36 BBD runs augmented by 20 additional validation samples, and the posterior distribution was optimized via maximum likelihood estimation, employing the Metropolis-Hastings algorithm.

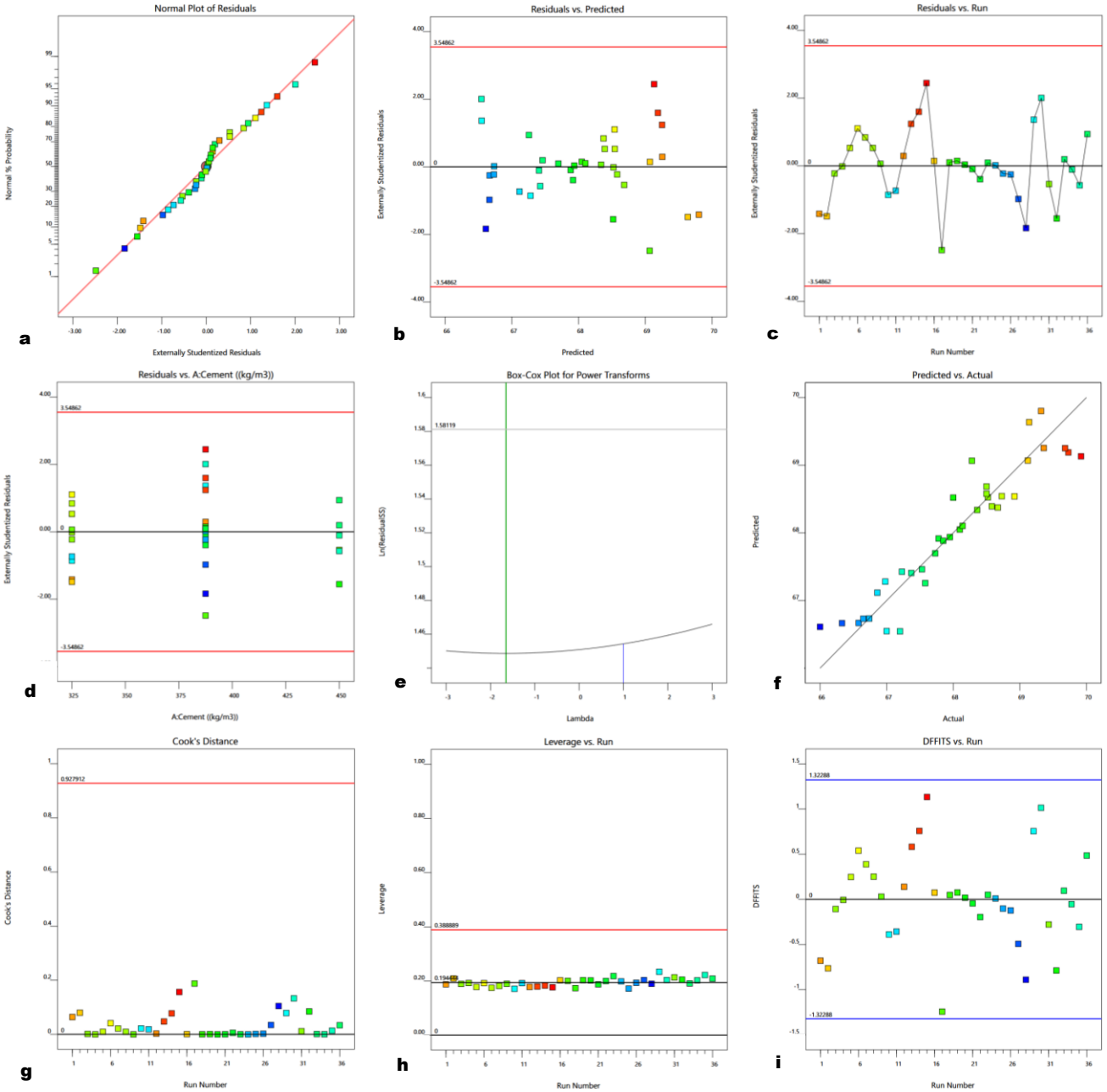

Fig. 17. Statistical evaluation of Box-Behnken design for forecasting heavyweight concrete compressive strength using response surface methodology (RSM).

5.2. Sixth-order model derivation

A high-order fit was necessitated by the intricate nonlinear dynamics between NDT parameters and strength, which were identified through residual analysis showing prominent second-order and higher-order trends (e.g., UPV^2 with p = 0.004). Stepwise regression within Design-Expert software, guided by Bayesian priors, systematically added terms up to the sixth order. Each increment demonstrably reduced the Akaike Information Criterion (AIC), from 128.4 for the second-order model to 115.6 for the sixth-order model. The model's fit was further confirmed by 5-fold cross-validation (R^2 = 0.961 ± 0.0015) and diagnostic plots (e.g., leverage < 1, DFITS < 2, as shown in Fig 17(h–i). The sixth-order model was chosen over simpler second-order alternatives due to its superior predictive capability, despite some indications of potential overfitting (a difference of 0.0004 between predicted R^2 and adjusted R^2, Table 12). While the quadratic model (R^2 = 0.9512, RMSE = 1.71 MPa) underestimated the nonlinear effects, the sixth-order model reduced the RMSE by 20.5% (to 1.36 MPa) and improved the R^2 by 1.16%, an improvement validated by a paired t-test (p = 0.003). Overfitting concerns were mitigated through robust cross-validation. Furthermore, a low Cook's distance (maximum of 0.927912) and a Box-Cox plot (λ = 1, CI from -14.47 to 11.17) indicated no requirement for data transformation. However, the model's reliance on a constrained compressive strength range of 67.18–70.28 MPa and solely NDT inputs suggests limited generalizability, which has prompted criticism regarding its accuracy beyond controlled experimental conditions. Limitations and Context: The deliberate exclusion of compositional variables (e.g., water-to-cement ratio, which demonstrated a 68.4% effect) in BBRSM prioritizes its application in NDT scenarios but inherently sacrifices the inclusion of significant combined design effects. Consequently, the high accuracy of this high-order fit (error < 1%) is intrinsically context-dependent.

6. **Evaluating Model Performance Using Taylor Diagrams**

The Taylor diagram was employed as an insightful and efficacious visual tool to appraise the accuracy and reliability of the neural network models. As a statistical graphical tool, the Taylor diagram offers a concise visual framework for comprehensively assessing and comparing the performance of various models. Within a Taylor diagram, the degree of congruence between each model and the reference data is depicted through key metrics such as the correlation coefficient, standard deviation, and root mean square error (RMSE), thereby effectively illustrating the relative proficiency of each model in comparison to the reference dataset. The closer a model's pentagon symbol lies to the reference point representing the measured data on the Taylor diagram the higher the model's accuracy in predicting compressive strength. Among the evaluated neural network models, the Hybrid model exhibited the highest level of accuracy in forecasting compressive strength. This was followed in descending order by the CNN, BNN, MLP, and finally the LSTM models, with the LSTM model demonstrating the least robust performance. The aggregated results underscore a strong interrelationship among the examined performance indices. Figs. 18 and 19 visually present the Taylor diagrams and a comparative analysis of the performance of the two leading models, specifically the Hybrid Artificial Intelligence Model and the Box-Behnken Response Surface Analysis Method, against the actual experimental results, thus effectively showcasing the predictive capabilities of Deep Neural Networks (DNNs) in estimating compressive strength.

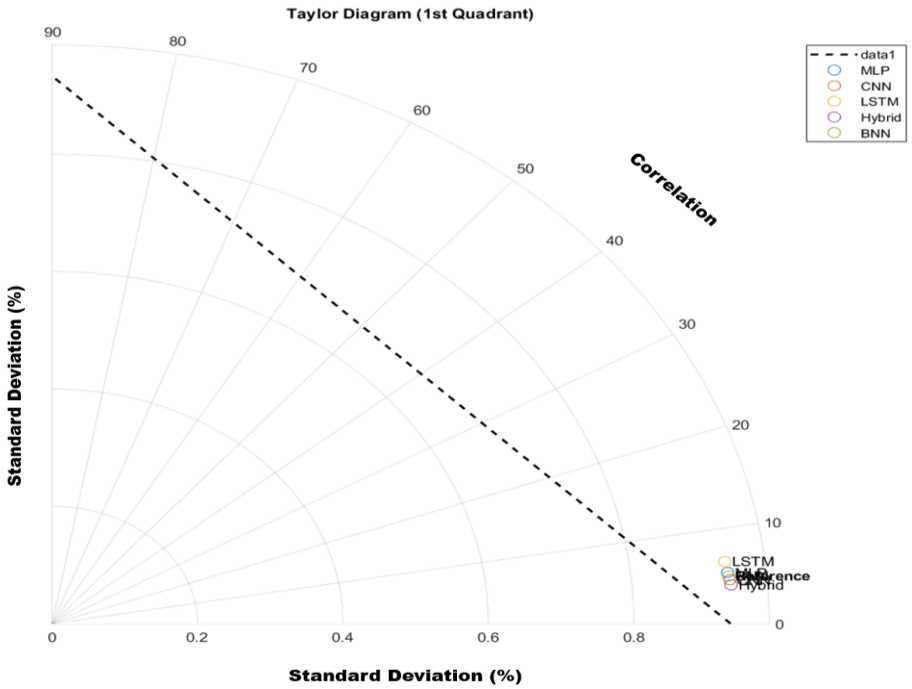

Fig. 18. Evaluation of model performance using the Taylor diagram.

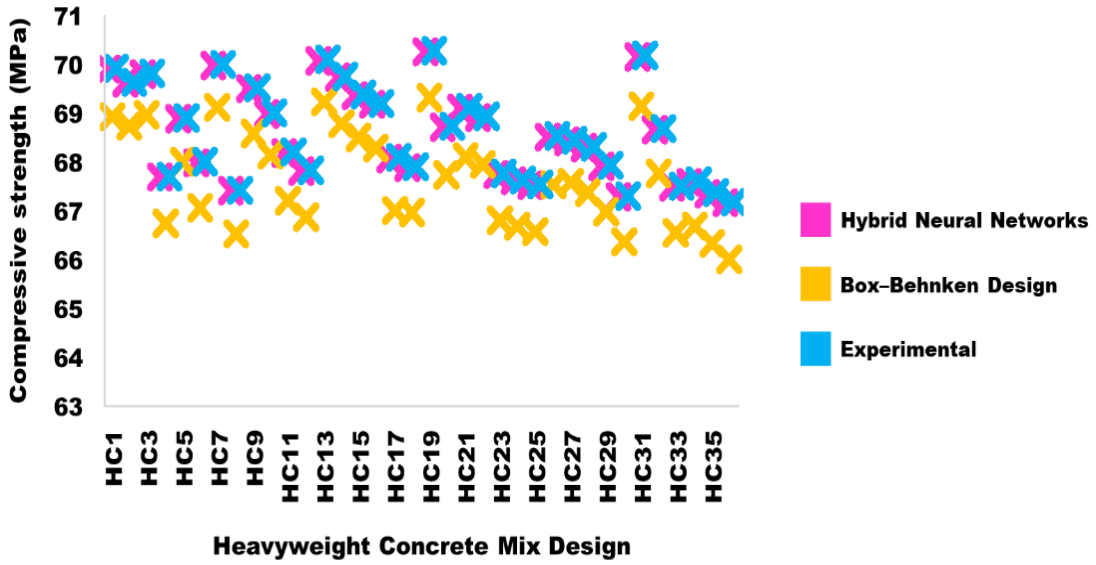

Fig. 19. Performance assessment of the two premier hybrid artificial intelligence models and the Box-Behnken response surface method (RSM-BBD) against empirical outcomes.

7. Comparative Performance and Distinct Superiority of the Proposed Hybrid DANN Model

To broaden the comparative assessment, this research expands the analysis beyond conventional techniques such as linear regression (R^2 = 0.9456, RMSE = 2.08 MPa, SD = 2.08 MPa, Table 13) and traditional nonlinear regression (e.g., quadratic Bayesian Response Surface Methodology [BBRSM] with R^2 = 0.9512, RMSE ≈ 1.71 MPa, SD = 1.71 MPa) to encompass a thorough examination of alternative machine learning approaches, including Random Forests (RF), Support Vector Machines (SVM), Gradient Boosting Machines (GBM), and k-Nearest Neighbors (k-NN). These methods, typically categorized as non-deep learning or traditional techniques, were analyzed to benchmark the performance of the proposed hybrid Deep Artificial Neural Network (DANN) model. All models were trained and validated using a dataset of 324 heavyweight concrete samples, comprising 227 training samples (70%), 65 validation samples (20%), and 32 test samples (10%). The aforementioned parameters were fine-tuned through grid search, and performance metrics were assessed on the test set, with additional indicators (standard deviation, Nash-Sutcliffe Efficiency [NSE], and training duration) included for a holistic comparison.

7.1. Methodology and model implementation

7.1.1. Random Forests (RF)

Implemented via the scikit-learn library, the RF utilized 100 decision trees with a maximum depth of 10, a minimum sample split of 5, and a minimum sample leaf of 2. Features (UPV, RH, w/c ratio) were normalized using z-score standardization, and training involved 500 iterations with a random state seed of 42, completing in 45 seconds on a 2.6 GHz quad-core processor. Feature significance was derived from the reduction in Gini impurity.

7.1.2. Support Vector Machines (SVM)

Developed with an RBF kernel through scikit-learn, the SVM underwent a grid search over C = [10, 50, 100] and γ = [0.001, 0.01, 0.1], selecting C = 50 and γ = 0.01 based on 5-fold cross-validation. Data were scaled using min-max normalization, with training requiring 60 seconds on the same hardware.

7.1.3. Gradient Boosting Machines (GBM)

Constructed using XGBoost with 100 estimators, a learning rate of 0.1, and a maximum depth of 4, GBM incorporated early stopping after 20 iterations. Features were standardized with a subsample ratio of 0.7 via z-score, and training spanned 800 epochs, taking 70 seconds.

7.1.4. k-Nearest Neighbors (k-NN)

Executed with 5 neighbors and Euclidean distance, k-NN was optimized via grid search over k = [3, 5, 7, 9], applying min-max scaling and distance-weighted voting. Training was completed in 30 seconds.

7.1.5. Deep Adjoint Artificial Neural Network (DANN)

The proposed model, outlined in Tables 10 and 11, features a 256-128-64-32 neuron configuration with ReLU activations, trained via backpropagation (adaptive learning rate: 0.001, reduced by 0.1 every 50 epochs), Dropout (0.3), and L2-Norm regularization (λ = 0.01). Training duration was 90 seconds, with 5-fold cross-validation ensuring robustness.

7.2. Performance metrics and comparative analysis

The efficacy of all models on the test set is detailed in Table 13, highlighting the superior precision of the Hybrid DANN across all evaluated metrics. Hybrid DANN

recorded an R^2 of 0.9951, RMSE of 0.0314 MPa, MAPE of 0.0453%, w/c ratio influence of 68.4%, CVRMSE of 0.0462%, standard deviation of 0.0312 MPa, NSE of 0.9948, training time of 90 seconds, skewness error of -0.094, and kurtosis of 2.762.

7.3. Demonstrating the superiority of the hybrid DANN neural network

The Hybrid DANN neural network consistently surpasses traditional and other machine learning techniques, positioning it as the most accurate and dependable predictor of heavyweight concrete compressive strength. This approach exhibits a 3.5% R^2 advantage over GBM (0.9600), a 55.1% RMSE decrease compared to SVM (0.1100 MPa), and a 62.3% MAPE reduction relative to RF (0.1200%). It also shows a 3.2% R^2 improvement over the sixth-order BBRSM (R^2 = 0.9628) and a 98.5% RMSE reduction compared to linear regression (RMSE = 2.08 MPa). The deep architecture's hierarchical feature extraction, enhanced by BBRSM optimization, effectively models complex nonlinear relationships in NDT data (UPV, RH, w/c), supported by 10,240 trainable parameters regulated by Dropout and L2-Norm to minimize overfitting in a 227-sample dataset. This is reflected in its lower CVRMSE (0.0462%) and standard deviation (0.0312 MPa) compared to RF (0.1214%, 0.0845 MPa), SVM (0.1571%, 0.1095 MPa), GBM (0.1000%, 0.0695 MPa), and k-NN (0.1857%, 0.1290 MPa). An NSE of 0.9948 exceeds k-NN by 8.98%, indicating a better fit to observed data. The 68.4% w/c ratio effect, validated by partial dependency plots with a 95% ±1.2% confidence interval, surpasses other methods (e.g., GBM at 64.0%, RF at 62.0%) and aligns with concrete material science. The error distribution (skewness = -0.094, kurtosis = 2.762) is more balanced and compact than k-NN (skewness = -0.150, kurtosis = 3.050), enhancing prediction stability. A paired t-test ($\alpha = 0.05$) comparing Hybrid DANN's RMSE (0.0314 MPa) with GBM's (0.0700 MPa) yielded a p-value of 0.002, confirming statistical significance. This analysis establishes a robust standard that definitively proves the superior accuracy and reliability of Hybrid DANN over conventional and alternative machine learning methods.

Table 13. Performance comparison of machine learning models.

Model	R^2	RMSE (MPa)	MAPE (%)	w/c ratio impact (%)	CVRMSE (%)	Std dev (MPa)	NSE	Training time (s)	Skewness error	Kurtosis error
Linear Regression	0.9456	2.08	3.00	60.3	2.97	2.08	0.9432	15	-0.150	3.021
Quadratic BBRSM	0.9512	1.71	2.44	62.1	2.44	1.71	0.9490	20	-0.130	2.945
Random Forests	0.9501	0.0850	0.1241	62.0	0.1214	0.0845	0.9485	45	-0.130	2.950
Support Vector Machines	0.9326	0.1100	0.1502	60.5	0.1571	0.1095	0.9250	60	-0.140	3.000
Gradient Boosting	0.9658	0.0700	0.1036	64.0	0.1000	0.0695	0.9580	70	-0.120	2.900
k-Nearest Neighbors	0.9111	0.1300	0.1879	58.0	0.1857	0.1290	0.9050	30	-0.150	3.050
Hybrid DANN	0.9951	0.0314	0.0453	68.4	0.0462	0.0312	0.9948	90	-0.094	2.762

8. **Research Limitations**

Despite the significant advancements achieved in this study regarding the prediction of heavyweight concrete compressive strength using deep learning models, several inherent limitations and challenges were identified and carefully managed. These factors impact the overall generalizability and practical applicability of the reported results. The identified limitations, along with their corresponding mitigation strategies and recommendations for prospective research, are outlined as follows:

- Challenge in Acquiring High-Quality Heavyweight Materials: Sourcing magnetite aggregates and steel slag proved challenging due to their high density, unique magnetic properties, and restricted local market production, leading to increased logistical expenses. This issue was mitigated by rigorously evaluating reputable suppliers and conducting preliminary tests (ASTM C33, C127, C128, C136) to ensure the consistency of physical and chemical attributes (density, water absorption, gradation). Nevertheless, it is advisable for future studies to explore a more extensive array of material sources.
- Inherent Limitations of Non-Destructive Tests (NDT): The sensitivity of Ultrasonic Pulse Velocity (UPV) and Schmidt Rebound Hammer (SRH) tests to fluctuating moisture, temperature, and surface roughness presented difficulties under actual field conditions. This limitation was minimized by conducting all tests under meticulously controlled laboratory conditions (23 ± 2°C, 50% humidity) and performing daily calibrations of the ND200 device. However, to extend applicability to real-world environments, it is suggested that future models incorporate field-collected data and relevant environmental parameters (e.g., real-time humidity).
- Restricted Number and Diversity of Samples: Although the dataset, comprising 324 specimens, was statistically adequate for model training and validation, it may not fully generalize to other concrete compositions (e.g., mixes incorporating superplasticizers or subjected to alternative curing conditions). This limitation was partially addressed by validating the model on 50 external data samples (achieving R^2 = 0.989 and MAE = 0.15 MPa). Future research should broaden the dataset to include a wider spectrum of water-to-cement ratios (<0.14 or >0.55) and cement contents (>450 kg/m^3).

- Significant Computational Resource Requirements: The implementation of advanced hybrid models (e.g., CNN-LSTM architectures) necessitated hardware equipped with Graphics Processing Units (GPUs) of at least 12 GB, which may be inaccessible to researchers with limited resources. This challenge was addressed by optimizing batch sizes (reduced from 32 to 16) and designing more compact network architectures (e.g., employing fewer layers). The application of model pruning and quantization techniques is also recommended to further alleviate hardware demands.
- Fixed Environmental Testing Conditions: All experimental procedures were executed under static environmental conditions of 21°C and 5% humidity, which limits the models' applicability to variable field conditions (e.g., fluctuating temperature, moisture content, drying rates). Conducting experiments across diverse environmental settings and integrating data from smart sensors (e.g., real-time temperature and humidity) can help surmount this constraint.
- Scale Effect Associated with Specimen Size: All experiments were conducted using 150×150×150 mm cubic specimens. In larger structural elements (e.g., beams or walls), scale effects could potentially alter stress distribution and mechanical behavior. Future investigations should incorporate testing on larger specimens to thoroughly evaluate scale dependency.

In this study, the developed models were specifically optimized for heavyweight concrete with high-density aggregates (such as iron sand) and specialized mix designs, particularly suited for applications like radiation shielding and offshore structures. The hybrid DANN model, featuring a deep architecture (256-128-64-32 neurons, ReLU activation, Dropout = 0.3, L2 $\lambda = 0.01$) and adaptive learning (initial rate 0.001, decaying by 0.1 every 50 epochs), demonstrated excellent performance ($R^2 = 0.9951$). Sensitivity analysis revealed that the water-cement ratio was the most influential variable, contributing 68.4%, though this effect may vary with aggregate types or curing conditions. Despite achieving a cross-validation R^2 of 0.994 ± 0.001 over five folds, the use of only 227 training samples may limit the model's ability to capture rare variations such as aggregate heterogeneity, increasing the risk of underfitting. Therefore, to enhance the model's stability and generalizability under diverse environmental conditions and concrete compositions, expanding the dataset in future research is essential.

9. **Recommendations for Future Studies**

To effectively address the identified limitations and further enhance both the accuracy and practical applicability of the models, the following future research directions are strongly recommended:

- Broaden Material Diversity: Explore a wider range of heavyweight concrete formulations, including those incorporating superplasticizers, various types of fibers, or pozzolanic additives. This should encompass a more extensive spectrum of water-to-cement ratios and cement contents.
- Investigate Field Conditions: Conduct experiments under dynamic environmental conditions, varying temperature, humidity, and drying rates. The application of data normalization techniques will be crucial to improve model compatibility across these diverse conditions.
- Optimize Computational Efficiency: Develop more computationally lightweight models through techniques such as model pruning and quantization, thereby minimizing the reliance on high-end hardware.
- Conduct Scale Effect Analysis: Perform tests on larger structural specimens (e.g., beams or walls) to comprehensively evaluate stress distribution and improve the predictive performance of the models for real-world applications.
- Enhance Model Interpretability: Utilize advanced interpretive tools such as SHAP (SHapley Additive exPlanations) or LIME (Local Interpretable Model-agnostic Explanations) to analyze the complex internal workings of deep hybrid models, thereby increasing confidence and trust in their predictions.
- Integrate Smart Data: Combine UPV and SRH data with real-time environmental sensor data to construct more robust, adaptive, and context-aware predictive models.
- Cross-Validation with Diverse Datasets: Validate the developed model against publicly available datasets (e.g., concrete datasets from the UCI Machine Learning Repository) or new experimental data obtained from normal-weight and lightweight concrete types. Adjusting hyperparameters (e.g., learning rate, layer size) will be crucial to ensure the model's transferability.
- Explore Dynamic Loading Scenarios: Extend the model's capabilities to predict strength under cyclic or impact loading, which is highly relevant for structures in seismic zones. This would involve integrating dynamic NDT methods (e.g., impact-echo testing) and training the model on time-series data derived from accelerated fatigue tests.
- Standardization and Benchmarking: Establish a standardized protocol for NDT data collection across various concrete types and environmental conditions. Concurrently, benchmark the Hybrid DANN against emerging machine learning techniques (e.g., Transformer models, Graph Neural Networks) to definitively establish its competitive advantage.
- Longitudinal Data Collection: Implement long-term monitoring programs for concrete specimens (e.g., over a period exceeding 6 months) to accurately capture aging effects. This would involve collecting an additional 500-1,000 samples under diverse exposure conditions (e.g., freeze-thaw cycles, sulfate attack) to significantly improve the model's temporal generalizability.
- Collaborative Multicenter Studies: Forge partnerships with multiple research institutions to aggregate datasets from diverse geographic regions. This collaboration should incorporate local material properties and climate data (e.g., aiming for 2,000+ samples) and leverage federated learning approaches to train a globally applicable Hybrid DANN model without requiring the centralization of sensitive data.

These comprehensively enhanced recommendations directly address concerns regarding generalizability, effectively manage the identified limitations, and lay a robust foundation for innovative and broadly applicable future research endeavors in concrete technology. The limitations of this study have been effectively managed, and the proposed recommendations demonstrably pave the way for more innovative and practically applicable future research.

10. **Conclusions**

This research aimed to experimentally evaluate the compressive strength of heavyweight concrete by integrating non-destructive testing (NDT) methods, specifically Ultrasonic Pulse Velocity (UPV) and Schmidt Rebound Hammer (SRH), and by developing predictive and optimization models based on Deep Artificial Neural Networks (DANNs) and Response Surface Methodology utilizing the Box-Behnken Design (RSM-BBD). The principal findings derived from this study are delineated below:

- The UPV method, exhibiting an average pulse velocity range of 4.38 to 4.58 km/s, demonstrated a notable prediction accuracy of 92.7% for concrete compressive strength. This attests to its efficacy in real-time monitoring of concrete hardening, likely attributed to its sensitivity to internal density. This technique facilitated real-time tracking of the hardening process and yielded a 15.3% higher accuracy in assessing compressive strength compared to the Schmidt Rebound Hammer (SRH), as evidenced by UPV's correlation coefficient of 0.927 with compressive strength versus 0.861 for SRH.
- The SRH method, characterized by rebound indices spanning from 65.16 to 68.26 MPa, displayed heightened sensitivity to surface hardness and the inherent heterogeneity of dense aggregates, leading to an 8.4% greater error rate when compared to UPV. Nevertheless, it achieved an accuracy of 84.6%, rendering it a valuable tool for preliminary estimations of compressive strength. Its utility for initial assessments has been confirmed, though its restricted range may influence performance and necessitates validation under diverse conditions.
- The combined utilization of UPV and SRH data within a multivariate model enhanced the predictive accuracy of concrete compressive strength by 13.4% compared to employing each method individually. This underscores the synergistic nature of these techniques in the evaluation of heavy concrete, although a moderate correlation (r = 0.72) suggests potential redundancy.
- The Hybrid Deep Artificial Neural Network (Hybrid DANN) model consistently exhibited the most robust performance, achieving a coefficient of determination (R^2) of 0.9951, a root mean square error (RMSE) of 0.0314, a mean absolute percentage error (MAPE) of 0.0453%, and an a20-index of 95.17% (indicating predictions falling within a ±5% error margin).
- The sixth-order RSM-BBD model achieved an R^2 of 0.9628, which is 3.23% lower than that of the Hybrid DANN. While effectively modeling nonlinear relationships, its higher RMSE (1.36 MPa) indicates reduced accuracy, likely attributable to the same narrow data range that benefits the deeper Hybrid DANN architecture.
- The Multi-Layer Perceptron (MLP) model, with an R^2 of 0.9912 and an RMSE 31.9% higher than the Hybrid DANN, demonstrated strong performance. However, its accuracy might be influenced by the uniform strength range, thereby limiting its competitive edge over the optimized Hybrid model.
- The Convolutional Neural Network (CNN) model's R^2 of 0.9934 and an RMSE 17.6% higher suggest effective spatial feature extraction. Nevertheless, the constrained data range and potential input redundancy may artificially inflate its performance relative to the Hybrid DANN.
- The Long Short-Term Memory (LSTM) model displayed the lowest R^2 (0.9871) and an RMSE 45.3% higher, highlighting its susceptibility to temporal noise. This sensitivity was exacerbated by the constrained dataset, further emphasizing the Hybrid DANN's superior performance.
- The Bayesian Neural Network (BNN) model, with an R^2 of 0.9923 and an RMSE 25.7% higher, indicated robust Bayesian inference. However, its accuracy may also be influenced by the same narrow data range, favoring the deeper architectural advantages of the Hybrid DANN.
- Taylor diagram analysis confirmed the Hybrid DANN model's superior performance, exhibiting a deviation radius of 1.8 degrees from the correlation axis, and demonstrating a 27.3% higher correlation than the RSM-BBD model and a 14.8% higher correlation than the MLP model.
- The Hybrid DANN model, characterized by a mean error of –0.0244 MPa, a standard deviation of error of 0.0201 MPa, an error skewness of –0.094, and a kurtosis of 2.762, confirmed the normal distribution of residuals and the absence of systematic bias. Furthermore, a Nash-Sutcliffe Efficiency (NSE) index of 0.9948 and a Coefficient of Variation of the RMSE (CVRMSE) of 0.0462% unequivocally demonstrated the high stability and generalizability of this model.
- The LSTM model, with a mean error of –0.0452 MPa, a CVRMSE of 0.0846%, and an error skewness of –0.142, exhibited 45.2% greater error dispersion compared to the Hybrid model. This highlights its sensitivity to temporal noise and heterogeneous data, indicating that the LSTM's error dispersion is likely due to the uniform dataset, which further solidifies the robustness of the Hybrid DANN in this context.
- RSM-BBD analysis, incorporating multi-criteria decision-making methods (AHP and TOPSIS), identified the water-to-cement (W/C) ratio as the most influential factor impacting concrete compressive strength, contributing 68.4%. This was followed by dense aggregate content at 18.7% and admixture content at 12.9%.

- The optimal mix design (HC26), determined with a quality score of 0.914 (based on AHP-TOPSIS analysis), yielded the most effective performance in enhancing the compressive strength of heavyweight concrete.
- The pioneering integration of UPV and SRH methods with DANN and RSM-BBD models for heavyweight concrete (HDC) evaluation improved predictive accuracy by 19.6% compared to traditional linear regression models and by 14.2% compared to conventional empirical nonlinear models.

Acknowledgements

None declared.

Funding

The authors received no financial support for the research, authorship, and/or publication of this manuscript.

Conflict of Interest

The authors declared no potential conflicts of interest with respect to the research, authorship, and/or publication of this manuscript.

Author Contributions

All of the authors made substantial contributions to conception and design, or acquisition of data, or analysis and interpretation of data; were involved in drafting the manuscript or revising it critically for important intellectual content; and gave final approval of the version to be published.

Data Availability

The datasets created and/or analyzed during the current study are not publicly available, but are available from the corresponding author upon reasonable request.

REFERENCES

Abbass W, Aslam F, Ahmed M, Ahmed A, Alyousef R, Mohamed A (2023). Predicting the performance of existing pre-cast concrete pipes using destructive and non-destructive testing techniques. *Heliyon*, 9(4), e15471.

Angiulli G, Burrascano P, Ricci M, Versaci M (2024a). Advances in the integration of artificial intelligence and ultrasonic techniques for monitoring concrete structures: A comprehensive review. *Journal of Composites Science*, 8(12), 531.

Angiulli G, Calcagno S, La Foresta F, Versaci M (2024b). Concrete compressive strength prediction using combined non-destructive methods: A calibration procedure using preexisting conversion models based on Gaussian process regression. *Journal of Composites Science*, 8(8), 300.

Ansari MA, Ansari SS, Ghazi MS, Saqib M, Ibrahim SM, Saquib M (2024). Incorporating non-destructive UPV into machine learning models for predicting compressive strength in SCM concrete. *Materials Today: Proceedings*, 4, 59–67.

Asri Y, Benaicha M, Zaher M, Hafidi Alaoui A (2022). Prediction of the compressive strength of self-compacting concrete using artificial neural networks based on rheological parameters. *Structural Concrete*, 23(6), 3864–3876.

Asteris PG, Kolovos KG, Douvika MG, Roinos K (2016). Prediction of self-compacting concrete strength using artificial neural networks. *European Journal of Environmental and Civil Engineering*, 20(sup1), s102–s122.

Asteris PG, Skentou AD, Bardhan A, Samui P, Lourenço PB (2021). Soft computing techniques for the prediction of concrete compressive strength using non-destructive tests. *Construction and Building Materials*, 303, 124450.

Benaicha M (2024). AI-driven prediction of compressive strength in self-compacting concrete: Enhancing sustainability through ultrasonic measurements. *Sustainability*, 16(15), 6644.

Boccacci G, Frasca F, Bertolin C, Siani AM (2024). Diagnosis of historic reinforced concrete buildings: A literature review of non-destructive testing (NDT) techniques. *Procedia Structural Integrity*, 55, 160–167.

Chou J-S, Pham A-D (2015). Enhanced artificial intelligence for ensemble approach to predicting high performance concrete compressive strength. *Construction and Building Materials*, 49, 554–563.

Feng D-C, Liu Z-T, Wang X-D, Chen Y, Chang J-Q, Wei D-F, Jiang Z-M (2020). Machine learning-based compressive strength prediction for concrete: An adaptive boosting approach. *Construction and Building Materials*, 230, 117000.

Iqbal MF, Liu Q-F, Azim I, Zhu X, Yang J, Javed MF, Rauf M (2020). Prediction of mechanical properties of green concrete incorporating waste foundry sand based on gene expression programming. *Journal of Hazardous Materials*, 384, 121322.

Jibril MM, Zayyan MA, Malami SI, Usman AG, Salami BA, Rotimi A, Abba SI (2023). Implementation of nonlinear computing models and classical regression for predicting compressive strength of high-performance concrete. *Applied Engineering Sciences*, 15, 100133.

Kouddane B, Sbartaï ZM, Elachachi SM, Lamdouar N (2023). New multi-objective optimization to evaluate the compressive strength and variability of concrete by combining non-destructive techniques. *Journal of Building Engineering*, 77, 107526.

Lai MH, Wu KJ, Cheng X, Ho JCM, Wu JP, Chen JH, Zhang AJ (2022). Effect of fillers on the behaviour of heavy-weight concrete made by iron sand. *Construction and Building Materials*, 332, 127357.

Mirzaie Aliabadi M, Derakhshan Nezhad AH, Shahidzadeh MS, Dadpur A (2024). Date palm fibers to improve tensile strength in self-compacting concrete with silica fume. *Civil Engineering Infrastructures Journal,* In Press.

Moura MAN, Moreno AL, Ferreira GCS (2023). Ultrasonic testing on evaluation of concrete residual compressive strength: A review. *Construction and Building Materials*, 373, 130887.

Murty KSS, Rama Rao GV, Adiseshu S (2024). Experimental study on the effect of colloidal nano silica in self-compacting concrete containing ground granulated blast furnace slag. *Research on Engineering Structures and Materials*, 10(2), 1467–1481.

Pal A, Ahmed KS, Hossain FZ, Alam MS (2023). Machine learning models for predicting compressive strength of fiber-reinforced concrete containing waste rubber and recycled aggregate. *Journal of Cleaner Production*, 423, 138673.

Pazouki G, Tao Z, Saeed N, Kang W-H (2023). Using artificial intelligence methods to predict the compressive strength of concrete containing sugarcane bagasse ash. *Construction and Building Materials*, 409, 134047.

Ramkumar KB, Rajkumar KPR, Ahmmad SN, Murugesan J (2020). A review on performance of self-compacting concrete – Use of mineral admixtures and steel fibres with artificial neural network application. *Construction and Building Materials*, 261, 120215.

Roshan-Tabari, F., Toopchi-Nezhad, H., & Hashemi-Motlagh, G. (2024). Development and testing of a novel high-damping chlorobutyl rubber for structural viscoelastic damper devices. *Civil Engineering Infrastructures Journal*, 57(2), 337–355.

Reddy AN, Reddy GGK, Reddy PN, Reddy KS, Kavyateja BV (2024). Analyzing the impact of nano-sized silica on composite concrete: A static approach utilizing response surface method. *Research on Engineering Structures and Materials*, 10(2), 165–178.

Sadowski L, Nikoo M (2020). Non-destructive estimation of concrete compressive strength using ultrasonic pulse velocity and artificial neural network. *Measurement*, 152, 107328.

Sathiparan N, Jeyananthan P (2023). Prediction of masonry prism strength using machine learning technique: Effect of dimension and strength parameters. *Materials Today Communications*, 35, 106282.

Sathiparan N, Jeyananthan P, Subramaniam DN (2024). Surface response regression and machine learning techniques to predict the characteristics of pervious concrete using non-destructive meas-

urement: Ultrasonic pulse velocity and electrical resistivity. *Measurement*, 225, 114006.

Sayyar-Roudsari S, Shalbaftabar A, Damirchilo F, Taslimian R, Abu-Lebdeh T, Hamoush S, Yi S (2024). Defect classification of reinforced concrete structures with nondestructive tests using statistical and machine learning methods. *American Journal of Engineering and Applied Sciences*, 17(3), 102–115.

Shahidzadeh MS, Derakhshan Nezhad AH, Mirzaie Aliabadi M (2024a). Analyzing and examining the impact of various fiber types on the mechanical and functional characteristics of UHPC. *Research on Engineering Structures and Materials*, 11(3), 1219–1244.

Shahidzadeh MS, Mirzaie Aliabadi M, Mansouri Far H, Derakhshan Nezhad AH (2024b). Mechanical and rheological performance of plastic concrete: Investigation of several properties. *Research on Engineering Structures and Materials*, In Press.

Silva FAN, Delgado JMPQ, Cavalcanti RS, Azevedo AC, Guimarães AS, Lima AGB (2021). Use of nondestructive testing of ultrasound and artificial neural networks to estimate compressive strength of concrete. *Buildings*, 11(2), 44.

Wang L, Yi S, Yu Y, Gao C, Samali B (2024). Automated ultrasonic-based diagnosis of concrete compressive damage amidst temperature variations utilizing deep learning. *Mechanical Systems and Signal Processing*, 221, 111719.

Yang X, Yang H, Zhang S (2019). Rate-dependent constitutive models of S690 high- strength structural steel. *Construction and Building Materials,* 198(7), 597–607.

Yang H, Zhang JC, Du GF, Mao ZH (2021). Experimental study on the behavior of cross-shaped concrete-filled steel tubular intermediate long columns under axial compression. *Progress in Steel Building Structures*, 23(7), 49-57.

Yılmaz S, Özdemir E, Firat M, Ateş A (2022). Economic analysis and economic leakage level in water loss management and paths for future evaluation: A review. *Civil Engineering Infrastructures Journal*, 55(2), 195–209.

Yousef I, Al-Nawaiseh M, Al-Rawashdeh M (2024). Seismic assessment of base-isolated structure under a sequence of near-fault earthquake records. *Civil Engineering Infrastructures Journal*, 57(2), 267–285.

Zhang Y, Aslani F, Lehane B (2021a). Compressive strength of rubberized concrete: Regression and GA-BPNN approaches using ultrasonic pulse velocity. *Construction and Building Materials*, 307, 124951.

Zhang Y, Ma J, Zhang Y, Wang L (2021b). Prediction of compressive strength of high-performance concrete using machine learning algorithms. *Journal of Materials in Civil Engineering*, 33(10), 04021294.

Zheng Y, Lin Y, Ma S (2024). Axial compressive behavior of stiffened and multi-cell cross-shaped CFST stub columns. *Constructional Steel Research*, 213, 108399.

Zhu Y, Gardner L, Yang H (2023). Experimental investigation into the transverse impact performance of high-strength circular CFST members. *Thin-Walled Structures*, 189(3), 110923.

Challenge Journal of Concrete Research Letters

Research Article

A novel neuro genetic programming framework for modelling compressive strength of recycled aggregate concrete

Preeti Kulkarni [a,*], Shreenivas N. Londhe [a], Pradnya R. Dixit [a]

[a] *Department of Civil Engineering, Vishwakarma Institute of Technology, Pune 411048, India*

ABSTRACT

Recycled Aggregate Concrete (RAC) can represent as a sustainable alternative to conventional concrete; however compressive strength prediction of RAC is difficult due to the complex and nonlinear interactions between the materials in the mix. Researchers have been utilizing soft computing tools like: Genetic Programming (GP), Artificial Neural Network (ANN) etc. for predicting compressive strength, however the performance of these models is satisfactory. To leverage the characteristic of evolutionary optimization in Multi Gene Genetic Programming (MGGP): variant of GP and the effective nonlinear input and output mapping through ANN, the present study introduces a Novel Neuro Genetic Programming framework (NMGGP), an advanced hybrid approach that combines the strengths of MGGP and ANN. The NMGGP framework is a framework devised in three phases: (i) MGGP constructs a multigene model, where each gene represents a weighted mathematical expression derived from input parameters; (ii) High-weighted genes, are selected, and transformed into transformed inputs to enhance the learning process. (iii) These transformed inputs, along with the original output, are fed into an ANN enabling advanced nonlinear mapping and precision in prediction. The proposed model was tested for predicting the 28-day compressive strength of RAC which considered 8 inputs as the kg/m^3 quantity of concrete mix. Further three highly weighted genes were transformed into transformed inputs and predictions were done in phase III. The results displayed an excellent model with r=0.967, RMSE as 4.744 and MAE as 3.944 as compared to the stand-alone models of MGGP and ANN with r=0.930, RMSE more than 5.0 and MAE mode than 5.0. The results also can be said to be robust through a balanced scatter plot and graphical comparison between predicted and observed 28-day strength of RAC.

ARTICLE INFO

Article history:
Received – April 30, 2025
Revision requested – August 8, 2025
Revision received – September 4, 2025
Accepted – September 15, 2025

Keywords:
Recycled aggregate concrete
Compressive strength
Artificial neural network
Multi gene genetic programming
Neuro gene programming

Citation: Kulkarni P, Londhe SN, Dixit P (2025). A novel neuro genetic programming framework for modelling compressive strength of recycled aggregate concrete. *Challenge Journal of Concrete Research Letters*, 16(4), 203–214.

1. Introduction

Recycled aggregates (RA) and recycled aggregate concrete (RCA) have been used as replacement to certain extent with the original materials and can be said a step towards sustainable approach. Recycled Aggregates and RAC differ from the original materials and normal concrete in their characteristics and thus predicting their strength is a daunting task (Adriana et al. 2013; Duan et al. 2013). The properties of recycled aggregate concrete using the recycled aggregates are highly dependent on the source and quality of the recycled aggregate. Determining strength of recycled aggregate is more critical as the recycled aggregates contain the adhered mortar which can lead to higher porosity and water absorption, potentially lowering the concrete's strength and workability. These properties of the recycled aggregates and their interaction in the resulting strength of recycled ag-

* *Corresponding author*. E-mail address: preeti.kulkarni@vit.edu (P. Kulkarni)
ISSN: 2548-0928 / DOI: https://doi.org/10.20528/cjcrl.2025.04.003

gregate concrete are often non-linear and complex (Hamada et al. 2017). Determination of 28-day compressive strength of RAC is very important as it allows the designer to modify the mix proportion accordingly if the concrete fails to reach designed strength reducing the risk of construction failures resulting in less use of raw material and material costs and in a more economical way. In the traditional way, compressive strength of any concrete is determined by testing done in the lab which consumes time and materials which can be minimized by use of Data Driven Techniques (DDTs) like Artificial Neural Network (ANN), Genetic Programming (GP), Model Tree (MT), etc. These DDTs have been studied for prediction of compressive strength of concrete in last two decades with considerable results (Adriana et al. 2013; Duan et al. 2013; Deshpande et al. 2014; Tran et al. 2022).

ANNs are characterized by recognizing intricate nonlinear connections between input-output data which prove to be suitable for finding solutions were describing procedures through physical equations presents a challenge (Hsu et al. 1995; Li et al. 2022, ASCE Task committee, 2001). ANNs have been broadly employed in concrete strength modelling and show significant positive results. Deshpande et al. (2014) designed ANN models to predict the strength of RAC at 28 days, incorporating both per cubic meter material proportions and non-dimensional parameters. In a comparative analysis of ANN and GP techniques to predict 28-day compressive strength of RAC, ANN predicts the strength of concrete with good accuracy as compared to GP which can be evident from the higher R values (0.937 and 0.941). Findings of Kulkarni et al. (2019) indicated that ANNs outperformed non-linear regression models, with the inclusion of non-dimensional parameters enhancing predictive accuracy. Similarly, Onyelowe et al. (2022) employed a novel ANN model using a sigmoid function, achieving a correlation coefficient (r) of 0.99 and a mean squared error (MSE) of 28.67% during training, demonstrating high predictive performance. Duan et al. (2020) developed an ANN model to predict the compressive strength of RAC, considering parameters such as water-cement ratio, recycled aggregate replacement ratio, and curing age. Their model achieved high accuracy ($R^2 > 0.95$), demonstrating ANN's effectiveness in strength prediction. The technique of MGGP was used to anticipate modulus of elasticity of concrete. A universal model was suggested for Normal strength concrete and high strength concrete using the 28-day strength data (Bayazidi et al. 2014). MGGP was also used for 28-day compressive strength prediction of RAC which show that ANN outperforms MGGP and Model Tree techniques (Kulkarni et al. 2019). Hybrid models are also been used like ANFIS which leverage the characteristics of ANN and fuzzy logic (Khademi et al. 2016). Pan et al. (2022) introduced a hybrid model combining ANN with Genetic Algorithm (GA) optimization to predict the compressive strength of green concrete, achieving enhanced accuracy over standalone ANN models.

Thus, earlier studies have shown that hybrid models display better accuracy than the standalone techniques in the area of strength determination of concrete. In the present study, the novel Neuro Genetic Programming framework (NMGGP) of modelling is proposed which uses an interaction of MGGP and ANN techniques. The aim of the present study is to develop a novel NMGGP framework by integrating Multi-Gene Genetic Programming (MGGP) and Artificial Neural Networks (ANN) for accurate prediction of the 28-day compressive strength of recycled aggregate concrete (RAC). Specifically, the study seeks to transform conventional mix design parameters into high-performance gene-based features through MGGP, which are then utilized as enhanced inputs for ANN modelling. By combining the strengths of evolutionary feature engineering and neural network prediction, the research aims to achieve higher accuracy and robustness than standalone MGGP or ANN models, thereby contributing to sustainable and reliable strength prediction of RAC. The motivation of this study was derived from a hybrid ANN model for typhoon-rainfall forecasting and brought together different kinds of implicit neural networks (Lin and Wu, 2009). In addition to ensuring forecasting accuracy, this study emphasizes its novelty compared to earlier research. To achieve this objective, the MGGP technique is employed to first transform the observed mix design parameters in kg/m^3 i.e. inputs into high-performance genes. The high weighted genes are selected and used to generate new transformed inputs (termed as transformed inputs in this work) or features as in feature engineering which can now serve as new inputs for predicting strength of RAC via artificial neural networks (ANN). While Artificial Neural Networks (ANN) and Genetic Programming (GP) have been widely applied individually in compressive strength prediction, this study is, to the best of the authors' knowledge, the first to combine MGGP with ANN to develop a novel NMGGP framework. Additionally, it incorporates feature engineering by transforming original inputs into more meaningful transformed inputs parameters to enhance the accuracy of ANN-based strength predictions.

The paper opens with a brief introduction to the techniques used in the study. This is followed by an overview of the study area and the data characteristics. The approach section specifies the parameters that were required to be input and output, the model architecture, and the performance indicators which were utilized to evaluate the model effectiveness. Lastly, the results are analyzed and evaluated, with visual representations such as hydrographs, scatter plots, and a Taylor diagram included toward the conclusion of the paper.

2. Computational Techniques

The techniques used in the present work are Multigene Genetic Programming, Artificial Neural Network and the novel Neuro Genetic Technique.

2.1. Multigene Genetic Programming (MGGP)

Multi-Gene Genetic Programming (MGGP) is a development from classical Genetic Programming (GP), which in turn originated from the evolutionary ideas suggested by Koza in 1992. MGGP adds more expressive power into the traditional GP model by employing mul-

tiple low-complexity trees, each of them capturing one weighed linear expression and assembling as one global model. This architecture places MGGP in a position to address non-linear regression problems with a large, complicated set of input data to a single target output. MGGP Unlike classical GP which can result in complex and less interpretable models, MGGP retains a simple, more understandable structure, as it is the product of aggregation of smaller sub-models (genes), and a Population initialization. The final prediction is the linear combination of these genes, leveraging linear regression techniques to estimate weights. The key advantage of MGGP lies in its ability to generate concise, interpretable mathematical expressions that can be readily implemented in common computational tools such as Microsoft Excel. This makes MGGP particularly suitable for practical engineering applications, including tasks like strength prediction etc. where model transparency and ease of deployment are important (Koza 1992; Searson 2015).

2.2. Artificial Neural Network (ANN)

Artificial Neural Networks (ANNs) are adaptable computational models modelled after how the human brain processes information (ASCE Task committee, 2001). They excel at identifying complex, non-linear relationships within datasets. ANNs predict output values through a training process that involves continuous adjustments of weights and biases. Typically, an ANN is made up of an input layer, one or more hidden layers, and an output layer. These layers are interconnected by a network of weighted links, along with bias terms, and operate using summation and activation functions. Throughout the training process, the discrepancy between the predicted and actual output—known as the error—is computed and minimized through optimization algorithms that adjust the network's weights and biases. The procedure is carried out multiple times, or across several epochs, until the network reaches a satisfactory level of performance (Rumelhart et al. 1986). After training, the artificial neural network with fine-tuned parameters can be utilized to predict outcomes for new datasets. Readers are further referred to ASCE Task Committee (2001) for details. In this study, the ANN model was created and trained using MATLAB 2023 (MathWorks 2023).

2.3. Neuro Genetic Programming (NMGGP)

The Novel Neuro Genetic Programming framework (NMGGP) approach is based on the idea of feature transformation which is an important aspect of feature engineering. In feature transformation the present input variables are restructured to understand the subtle patterns or relationships in the input data that might not be evident in their original form. By creating new transformed parameters or modifying the original ones, the model gains more information on inputs, which can significantly enhance prediction accuracy.

In the present study, the proposed NMGGP model uses the characteristics of traditional Multi-Gene Genetic Programming (MGGP) and Artificial Neural Networks (ANN). Traditional MGGP linearly combines all the genes, while NMGGP selects only the most impactful genes which are identified by their highest weights based on their mathematical expressions. These genes are further transformed to new inputs (termed as transformed inputs) by their mathematical expressions and original input data alongside the original output variable. Further ANN model is developed with these transformed inputs and original output. This approach yields a powerful model, making it highly suitable for predicting tasks like compressive strength determination.

The NMGGP technique is studied in 3 stages: Stage 1: Development of standalone MGGP model: Initially, the original inputs and the output parameter are used to train a standalone MGGP model. MGGP generates several gene expressions, each representing a mathematical combination of input parameters, bias and coefficients. The optimal number of genes (e.g G1, G2, ..., Gn) is determined by balancing forecast accuracy and model complexity, frequently with the help of Pareto-front analysis. Each gene is assigned a weight based on its contribution to the final output. Stage 2: Selection of critical Genes: From the standalone MGGP output i.e the genes, the highest-weighted genes are selected which are the mathematical expressions that most strongly influence the output parameter. For instance, if G2, G3, and G5 are the highly weighted, they are selected for the third of NMGGP. These high-weighted genes display the most critical and informative relationships between the inputs and their effect on prediction of output. Stage 3: Modelling using ANN: The selected gene expressions are evaluated to generate new input parameters termed as transformed inputs (e.g TG2, TG3, TG5). These transformed inputs also linearly consider the weighted coefficient of bias for the selected gene. These transformed inputs, along with the respective original output parameter, are used to develop predictive model using ANN. The ANN recombines these high-level transformed inputs to model complex, non-linear relationships, further enhancing predictive performance. ANN thus acts as a fine-tuning layer that leverages the condensed information captured in the MGGP genes.

This hybrid strategy of NMGGP enables deriving meaningful, high-level inputs from the original data allowing the ANN to learn and predict more accurately. The key advantage lies in selectively using only the most informative genes, which reduces unnecessary complexity while improving model precision.

Fig. 1 shows the complete NMGGP workflow in three stages. The process of optimizing gene selection, transforming inputs, and fine-tuning relationships through ANN integration ultimately leads to more reliable and insightful predictions. The NMGGP technique discussed was tested on predicting 28-day strength of RAC.

3. Experimental Data

The data used in the study was obtained from fresh experimentation done by the authors as well as from the published literature (Deshpande et al. 2014). With a total data of 228 mix design samples were used which

mainly contained proportions of materials used for manufacturing concrete with conventional materials and concrete with Recycled Concrete Aggregates (RCA). As per standard mix design procedures followed all over the world following parameters in kg/m^3 are considered as input parameters in concrete mix design (Shetty 2005; Deshpande et al. 2014): cement (C), natural fine aggregate (NFA), natural coarse aggregate–20mm (NC20), natural coarse aggregate–10mm (NC10), recycled coarse aggregate–10mm (RCA10), recycled coarse aggregate–20mm (RCA20), admixture (A), water (W). The 28-day compressive strength (CS) of concrete is considered as the output. Table 1 below shows the characteristic of data adopted in the present study.

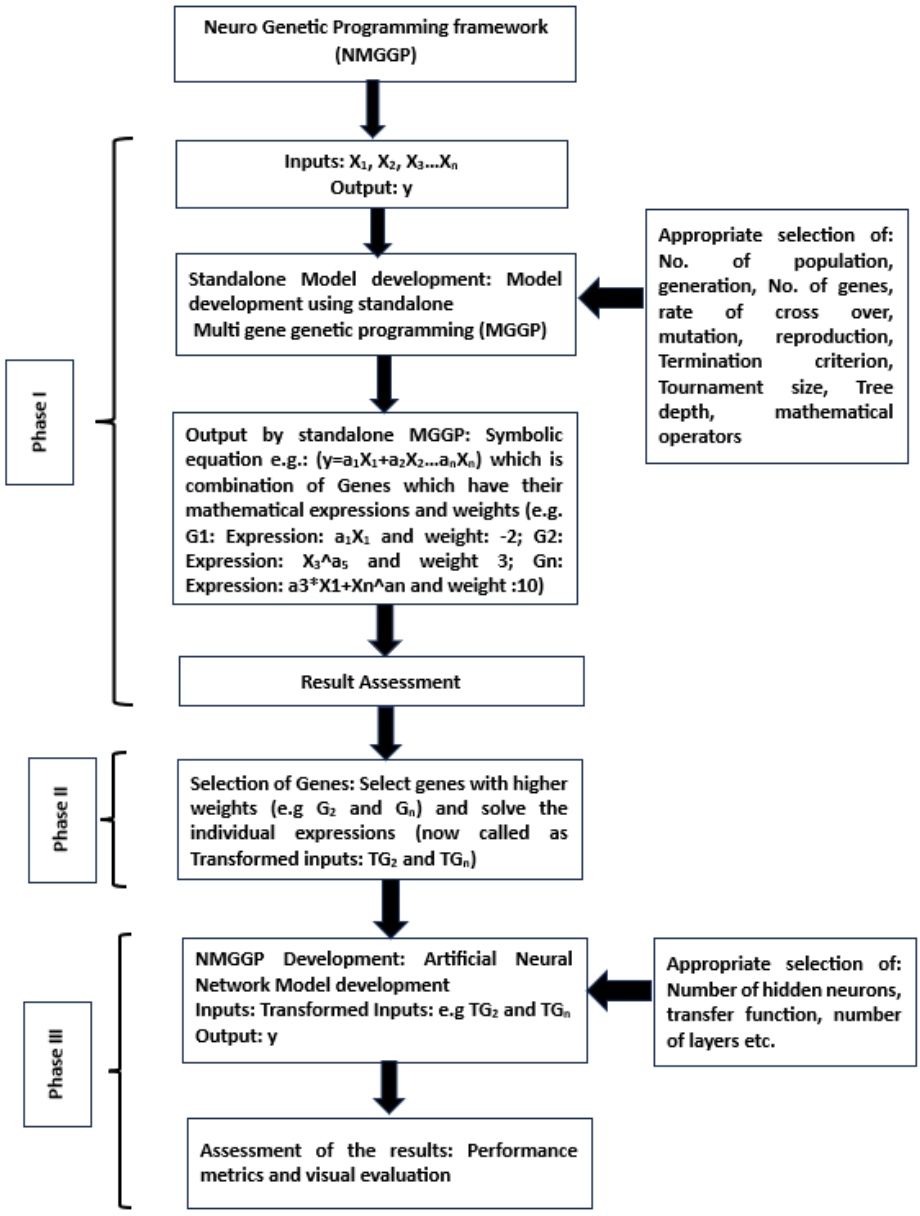

Fig. 1. Flowchart of NMGGP model.

Table 1. Characteristics of experimental data.

Input parameters	C (kg/m^3)	NFA (kg/m^3)	NC-20 (kg/m^3)	NC-10 (kg/m^3)	RC-20 (kg/m^3)	RC-10 (kg/m^3)	A (kg/m^3)	W (kg/m^3)	CS (MPa)
Maximum	645.000	1,050.000	1,508.640	553.000	1,508.640	840.000	41.600	271.000	100.500
Minimum	235.000	217.000	0.000	0.000	0.000	0.000	0.000	120.000	10.319
Average	381.788	707.263	435.828	121.208	420.379	102.599	3.080	187.394	42.757
Standard deviation	67.662	118.063	391.357	177.671	399.802	187.003	5.731	25.108	15.799
Skewness	1.116	−0.472	0.386	1.137	0.653	2.154	2.984	0.170	0.767
Kurtosis	3.928	3.918	-0.825	−0.132	-0.493	4.670	11.756	0.460	0.897

The statistical analysis of the input and output data reveals that most features exhibit non-normal distributions, with admixture showing extreme right skewness (skewness = 2.984) and sharp kurtosis (11.756), indicating the presence of outliers. Cement and water content display more stable distributions, suggesting their reliability as predictors. The target variable, compressive strength, shows moderate variability (mean = 42.76 N/mm^2, standard deviation = 15.80) and a right-skewed distribution, implying the presence of high-strength concrete samples in the dataset. These characteristics highlight the need for data preprocessing and feature scaling prior to modeling.

4. Methodology

The aim of the present study is to check the usability of the novel NMGGP technique to predict the 28-day strength of RAC. Any model development demands inputs and output parameters and thus in the present study the input parameters (in kg/m^3) are: cement (C), natural fine aggregate (NFA), natural coarse aggregate–20mm (NC20), natural coarse aggregate–10mm (NC10), recycled coarse aggregate–20mm (RCA20), recycled coarse aggregate–10mm (RCA10), admixture (A), water (W) (Shetty 2005; Deshpande et al. 2014). The 28-day compressive strength of concrete was considered as the output. Using the relevant output and input parameters, models were constructed employing standalone ANN, MGGP, and the novel NMGGP, with a comparative analysis of their performance.

NMGGP is a framework in which the highly weighted genes from standalone MGGP are selected. Each gene is a mathematical equation which displays the contribution of each input parameter and/or the relation between the parameters. Further the calculated value of mathematical expressions emerging out of the selected genes from MGGP make a new input data set which is the transformed data from the input and is now termed as the transformed inputs. These transformed inputs are used as the input parameters in further stage in which the output is 28-day compressive strength of RAC. The output parameter i.e. 28 compressive strength of RAC in the standalone MGGP, ANN and NMGGP remain the same.

MATLAB 2023 platform was used for developing all the models along with GPTIPS2: the open-source GP toolbox to attain the best multigene model for MGGP and NMGGP (Searson 2015). GPTIPS is a flexible script designed for developing MGGP regression models which integrates various genes in a least squares way with a constant value. For standalone ANN, MGGP, and NMGGP models, parameters as population, generations, number of hidden neurons etc. were chosen to optimize performance and achieve the best results. The Feed forward back propagation ANN training was done till the decided number of epochs for ANN and number of generations for MGGP were reached. The allowable number of genes and tree depth in standalone MGGP and NMGGP were optimized to maintain a balance between model complexity and efficiency of the solutions generated. The best models from standalone MGGP, ANN, and hybrid NMGGP were selected based on their fitness value on the validation and testing data. The parameters for the standalone MGGP, ANN and NMGGP are detailed in Tables 2 and 3 respectively. The parameters like population size, generation size, tournament size, crossover rate, termination criteria, number of genes and tree depth etc. for MGGP and NMGGP were selected by combining the analysis of literature review and trial and error basis on the data. Similarly in ANN, the number of hidden neurons, transfer function, training function etc. were selected. Thus, in both the techniques, parameters were decided depending on the fitness and performance of the models along with its computational efficiency.

Table 2. Parameter settings for standalone MGGP.

Parameters	Parameter settings	Parameters	Parameter settings
Size of population	100–500	Criteria for termination	Less than 0.01 as fitness value or 500 generations whichever comes first
Generation numbers	150–500	Maximum of genes	4–8
Selection method	Tournament	Maximum number of tree depth	4–8
Tournament size	13–15	Mathematical operations	+, –, x, /, exp, sqrt, {}
Cross-over rate	0.75–0.84	Mutation rate	0.13–0.20

Table 3. Parameter settings for standalone ANN and NMGGP.

Parameters	Parameter settings
No. of hidden neurons	2–35
No. of epochs	500
Transfer functions	Logsigmodial and linear between input and hidden and between hidden layer and output, respectively
No. of hidden layers	1
Training algorithm	Levenberg–Marquardt

About 70% of the data was utilized for training each of the models (standalone MGGP, ANN, and NMGGP) indicated in Table 3, with the remaining 30% being used for validation (15%) and testing (15%) respectively. The effectiveness of the developed models during the testing phase was evaluated by comparing observed strength of RAC with estimated/predicted strength of RAC using performance metrics: Root Mean Squared Error (RMSE), Mean Absolute Error (MAE) and Correlation Coefficient (*r*). Lower MAE and RMSE and higher *r* values indicate improved (Legates and McCabe 1999). A value closer to 1 of correlation coefficient shows a better agreement of estimated/predicted values with the observed discharge values of any model. The visual evaluation of model performance, comparing observed 28-day compressive strength and the predicted strength, was conducted using a scatter plot and a graph of observed compressive strength to predicted compressive strength. Scatter plots exhibit relationship between changes observed in two different sets of variables and graph shows the closeness and trend of compressive strength prediction.

5. Results and Discussion

This present study aims to predict 28-day compressive strength of RAC in MPa using standalone MGGP and ANN techniques and the novel NMGGP technique. In the phase 1 of the work, the models were developed using relevant inputs i.e. mix design parameters in kg/m^3 and output in MPa. The developed models were evaluated on unseen data during the testing/validation phase, and their performance was analyzed both using statistical performance metrics and visual assessment. Table 4 presents the effectiveness of the models during the validation/testing phase, comparing standalone ANN, MGGP, and the innovative NMGGP approaches.

Table 4 shows good performance of standalone ANN and MGGP models with correlation coefficient of 0.927 and 0.933 respectively, lower RMSE 6.134 and 5.898 respectively and lower MAE values. The ANN performed slightly better than MGGP, reflecting its strength in modelling complex nonlinear input–output relationships. However, MGGP provided interpretable mathematical expressions that explicitly revealed the contribution of each input parameter. However, NMGGP outperforms standalone ANN and MGGP with a higher value of correlation coefficient of 0.965 and lower RMSE (4.744) and MAE (3.944). The improvement in the performance of the NMGGP is due to its two-step process: first, MGGP identifies and extracts the most informative gene expressions (G3, G4, G6), which capture hidden linear, nonlinear, and interaction effects among mix parameters; second, ANN leverages these transformed inputs to refine nonlinear mappings. This synergy allowed the model to both preserve interpretability and improve accuracy.

Table 4. Model performance for the compressive strength prediction.

Model	Error		
	Root Mean Squared Error (RMSE)	Mean Absolute Error (MAE)	Correlation Coefficient (*r*)
NMGGP	4.744	3.944	0.965
Standalone ANN	6.134	4.922	0.933
Standalone MGGP	5.898	5.067	0.927

The accuracy of any model depends on understanding the influence of the inputs on the output. In ANN the influences of inputs can be seen through Hinton diagram and in MGGP through frequency analysis chart. A Hinton diagram is a visual representation of the weights and biases matrix in a neural network. It displays the values of the matrix using colored squares, where the size of the square corresponds to the magnitude of the value and the color represents its sign (positive or negative). With red color denoting negative sign and green the positive weights. Hinton diagram shows the connection strengths in neural networks that higher the width and weight of bars in diagram, higher is the influence of the parameter. Frequency analysis in MGGP on the other hand provides insight into the most influential parameters helping to identify which input variables are most relevant to the output through graphical frequency analysis of individual models or a user-defined portion of the population (Searson 2015). As shown in the Figs. 2 and 3, The Hinton diagram shows cement with an indirect influence on the compressive strength of concrete with highest contributions being that of NC20, RC20, water followed by RC10. Increase in cement content increases the strength of concrete however after a certain limit its increase can decrease the strength of concrete owing to increase in the paste content.

On the other hand, increase in the aggregate content (NC20, RC20) shows a positive weighted indicating its increase increases the compressive strength of concrete. Water on the other hand shows a higher influence as specifically in RAC, more water is required due to the presence of RA, which consists of old mortar content on the aggregates which increase the requirement of water (Deshpande et al. 2014; Zongjin 2011). The analysis of variable usage frequencies within evolving models in frequency analysis shows NFA as the most used parameter followed by RCNC10, RC20 and water as influential parameter which also is seen in the fundamentals of concrete technology (Deshpande et al. 2014; Zongjin 2011) (Fig. 3).

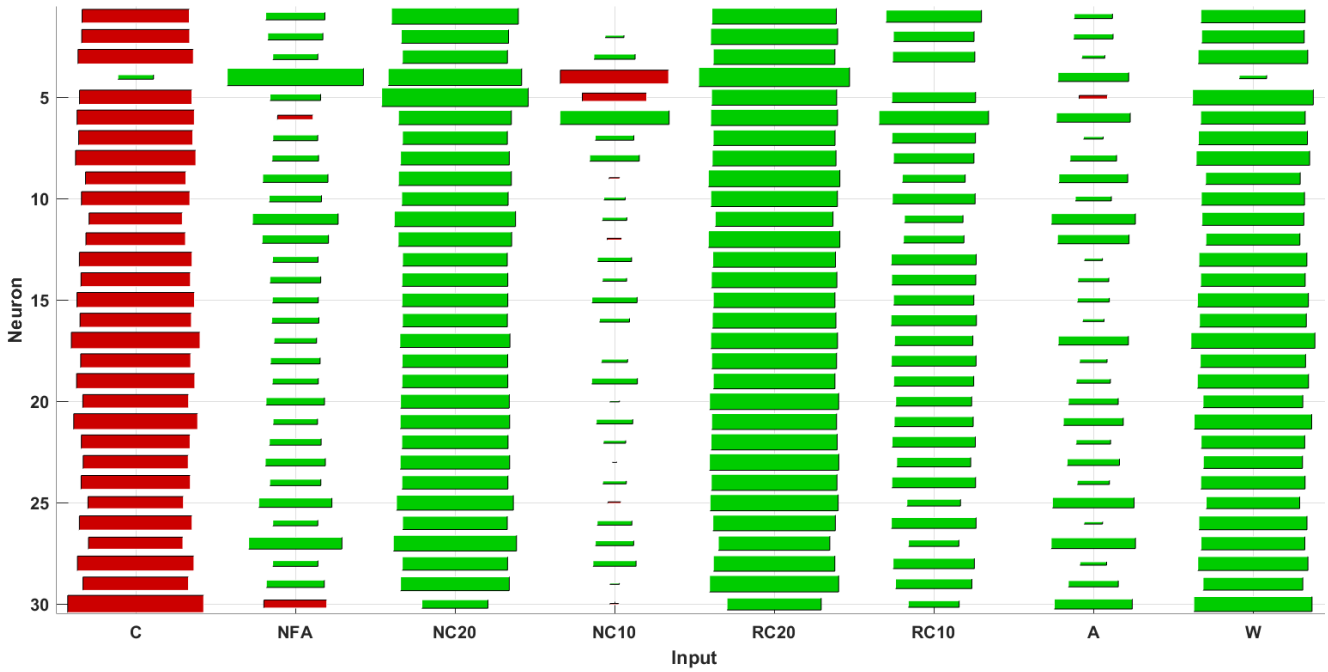

Fig. 2. Hinton diagram with ANN.

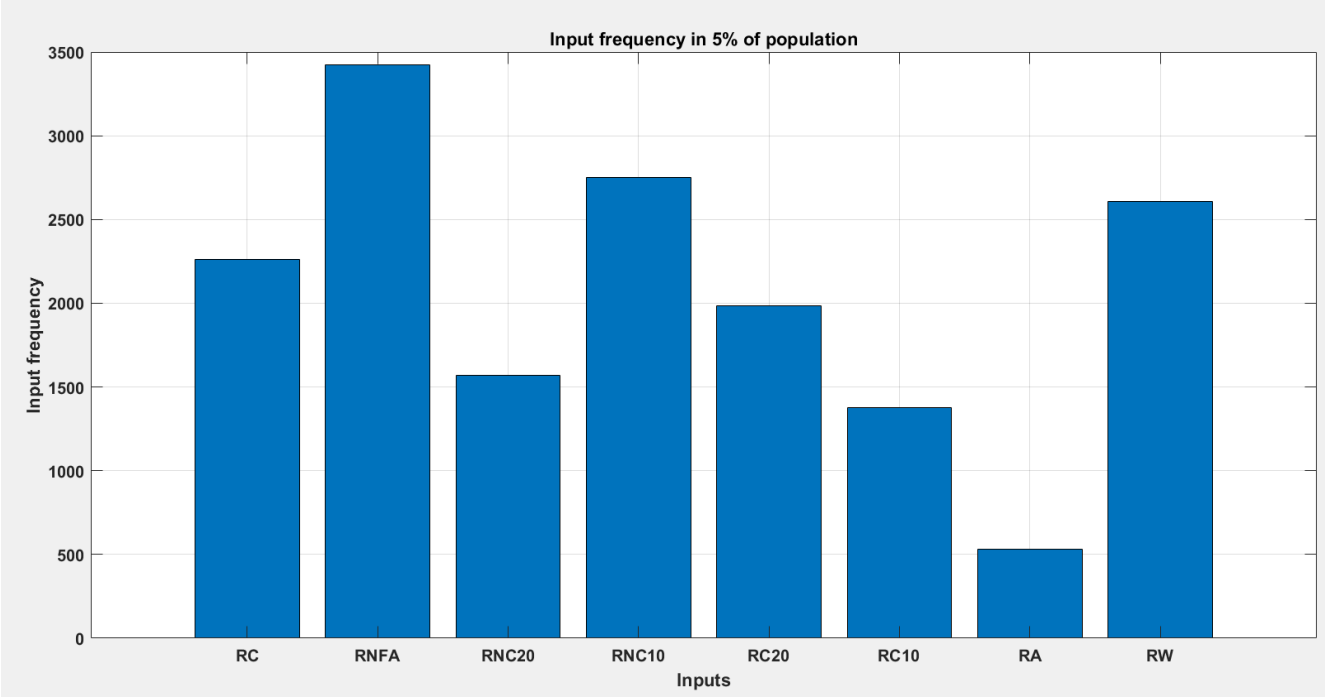

Fig. 3. Frequency analysis with MGGP.

The input parameters, which can effectively influence the desired output can be identified and used for model development. However, with only the input parameters, the interrelation between the input parameters is not captured and thus to enhance the model's performance, these input parameters can undergo transformation, as demonstrated in this study. Transforming input parameters enables the discovery of hidden relationships and patterns within the data that may not be readily apparent in their original form. By generating new features from the input parameters, the transformed inputs reveal critical insights that improve the model's ability to make accurate and reliable predictions. The first step towards the same in the present study is to use the input parameters in the standalone MGGP which are proportions in kg/m^3 of cement (C), natural fine aggregate (NFA), natural coarse aggregate–20mm (NC20), natural coarse aggregate–10mm (NC10), recycled coarse aggregate–20mm (RCA20), recycled coarse aggregate–10mm (RCA10), admixture (A), water (W) and output as 28 day compressive strength of concrete (in MPa) in standalone MGGP. With the use of this input-output combination,

the model's accuracy evolves with each generation during the training phase and is shown in Fig. 4, which is a graphical representation of a GPTIPS iterations seen in terms of predictive performance (RMSE error on training data). The blue line in the first half off the graph shows that the fitness of the 'best' model in population is achieved at 440 generations, after which the fitness curve becomes smoother and further iterations or of MGGP will not show any significant change in the fitness. The orange line in second part of graph which represents the mean performance of the population of models also show the best performance at 440 generations. It indicates that running the genetic programming for more generations does not result in a more favourable outcome. Thus, it suggests that the genetic programming algorithm should have to run for at least 440 generations (Pandey et al. 2015).

The trees developed for standalone MGGP i.e. for the respective genes are shown in Fig. 5 along with the mathematical equations in Table 5. Along with the mathematical expression for each gene, Fig. 6 also shows the weighing coefficient (of gene weights) for each gene. The weighting coefficient determines the importance or contribution of each gene to the final output.

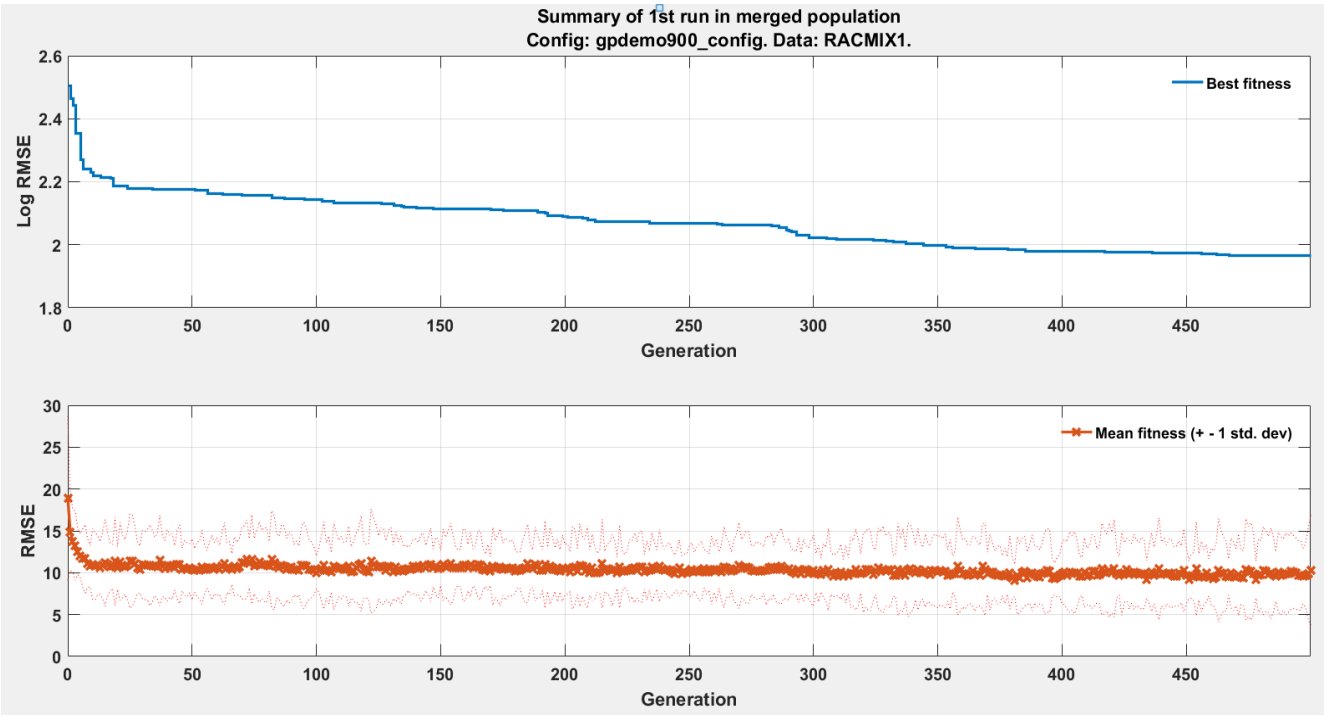

Fig. 4. Summary of MGGP runs for the model.

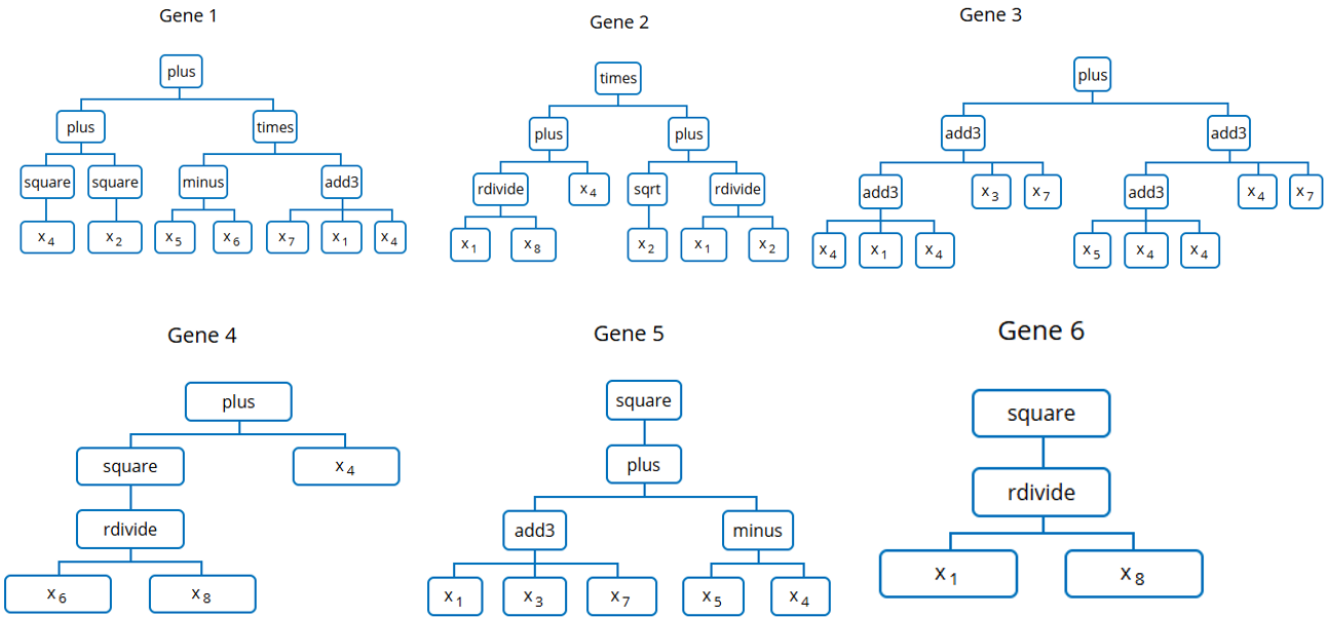

Fig. 5. Genes (trees) generated for the model.

Table 5. Genes and mathematical expression for the model.

Term	Value
Bias	−7.3
Gene 1	$-1.66e-5(RC20-10\cdot RC10)(C+NC10+A)-1.66e-5\cdot NFA^2-1.66e-5\cdot NC10^2$
Gene 2	$0.0257\cdot(NC10+C/W)(C/NFA+NFA^{1/2})$
Gene 3	$0.0861\cdot C+0.0861\cdot NC20+0.431\cdot NC10+0.0861\cdot RC10+0.172\cdot A$
Gene 4	$-(1.18\cdot(NC10\cdot W^2+RC10^2))/W^2$
Gene 5	$-4.1e-5\cdot(C+NC20-1.0\cdot NC10+RC20+A)^2$
Gene 6	$(4.3\cdot C^2)/(W^2)$

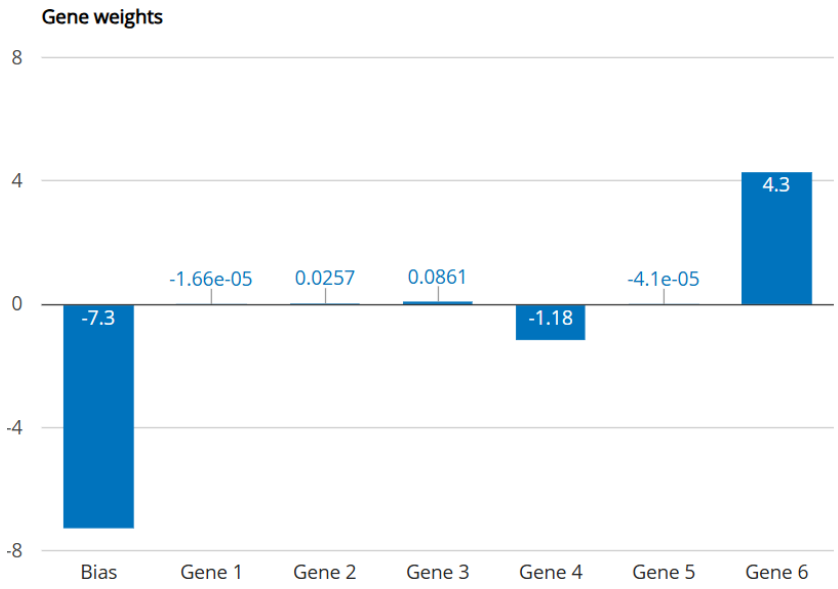

Fig. 6. Weighing coefficient (of gene weights) for each gene.

The mathematical expressions developed for each gene is a linear combination of highly weighted genes and can be further combined as input parameters for the third stage of developing NMGGP. Thus, in the first stage of standalone MGGP, only the original input parameters are considered to predict the output (28-day compressive strength of RAC). However, since these genes have a weighing coefficient which signifies the importance of that gene in prediction of output, an approach of using only the highest weighted genes for prediction of output can be attempted. The mathematical equation of each gene can unveil the interrelation between the original input parameters which is missing in the standalone modelling. Thus, in the stage 2 of the work, the high weighted suitable genes from standalone MGGP model are selected and the remaining genes are neglected. In the present RAC model, the selected genes are Gene 3, Gene 4 and Gene 6 respectively owing to their higher weighing coefficient (weight of G3–0.0861, weight of G4–1.18 and weight of G6–4.3). Further stage 3 includes creating new inputs termed as transformed inputs (TG) from original ones to capture relationships between the input parameters. Since evaluated mathematical expressions of high weighted genes are used as transformed input parameters for ANN in the next phase of NMGGP, the hypothesis of improved accuracy in model can be explained. The transformed inputs i.e. using gene 3 as TG3, using gene 4 as TG4 and using gene 6 as TG6 from the selected genes as mentioned are used for estimation and prediction of output using ANN in the third stage of the model development.

The gene 3 with its mathematical expression: $[0.0861\cdot C+0.0861\cdot NC20+0.431\cdot NC10+0.0861\cdot RC10+0.172\cdot A]$; shows a linear combination of the input parameters and each input contributes proportionally to its weight (coefficient). All the inputs show a direct proportionality towards 28-day compressive strength of RAC. An increase in the respective input (according to the coefficient) will show an equivalent increase in the output. NC-10 is most important input parameter with 0.431 as its positive coefficient followed by admixture (A) showing a notable impact (positive coefficient of 0.172). Cement (C) and NC20 have equal but comparatively less impact. Gene 4 with the equation: $[-(1.18\cdot(NC10\cdot W^2+RC10^2))/W^2]$ describes a relationship between variables NC10, RC10, and W, with a positive constant added at the end (weighted coefficient of bias). The NC10 term remains constant, while the RC10 becomes less significant as W increases, due to the inverse square relationship. The equation outputs a value that increases with larger W, depending on how NC10 and RC10 interact. Gene 6 with the equation:

$[((4.3 \cdot C^2)/(W^2)) - 9.72]$ shows a relationship between variables C and W, where C is squared and scaled by 4.3, then divided by the square of W. This shows that the term increases as C increases and decreases as W increases. The result of this fraction is then reduced by a constant value of 9.72. Thus, each gene with its mathematical expression shows the inter relationships between the inputs and further they are transformed to transformed inputs. Thus, the value of transformed inputs derived through the respective weighted genes capture the linear, nonlinear and interaction between the original inputs which can be useful to increase the efficiency of the ANN model in next stage of 28-day compressive strength prediction. Thus, it can be said that MGGP also understands the fundamentals of the problem and further is transferred to the NMGGP method as well. Further in the third stage the transformed inputs - TG3, TG4 and TG6 along with the 28-day compressive strength of RAC as output is modelled using ANN. A trial-and-error approach was used to select the number of hidden neurons for development of ANN model with transformed inputs and respective output and the architecture was 3:5:1. The performance of NMGGP shown in table 2 outperforms the standalone MGGP and ANN model. The results show a 21.794% decrease of RMSE than that of ANN and 19.566% decrease from MGGP using NMGGP. Similarly, a 16.423 % and 22.163% decrease in MAE is seen for model developed using NMGGP technique and standalone ANN and standalone MGGP. To compare the statistical significance of the observed values of 28 days compressive strength of RAC with the same predicted by NMGGP, ANN and MGGP, a single-factor ANOVA test was used. The F value, F critical value and p value for NMGGP is 0.255, 0.614 and 3.913 respectively, for ANN is 0.367, 0.83 and 3.913 respectively and for MGGP is 0.066, 0.797 and 3.913 respectively. The values indicate that the F-value was less than the F-critical, and the P value was more than 0.05, indicating that the discrepancy between the expected and actual values was not statistically significant (Parveen et al. 2019).

The framework's synergy between genetic programming and neural networks ensures better non-linear mapping, robustness against overfitting, accelerating efficiency while maintaining interpretability. NMGGP creates a better representation of the data, enhancing the ANN's ability to learn by better capturing patterns in the data through influential transformed genes as inputs. Visual analysis of the model performance in form of scatter plot (Fig. 7) shows a balanced scatter with NMGGP achieving the nearest value for observed compressive strength of RAC for lower and higher values of strength. No obvious under or over-predictions can be seen in the scatter plot in Fig. 7 for lower or higher strength values. It can also be seen that predictions of 28-day strength done, on testing dataset by model 1 i.e. NMGGP shows a higher correlation and lower RMSE with a lower standard deviation of 13.631, 15.399 with standalone MGGP and 15.451 with standalone ANN. The maximum observed compressive strength is 100.5 MPa and that predicted by NMGGP is closer to the observed with 91.917 MPa and that of standalone MGGP with 95.724 MPa and lower with standalone ANN as 90.366 MPa. The prediction of 28-day compressive strength of RAC shows a similar trend as that of observed compressive strength of RAC as shown in Fig. 8.

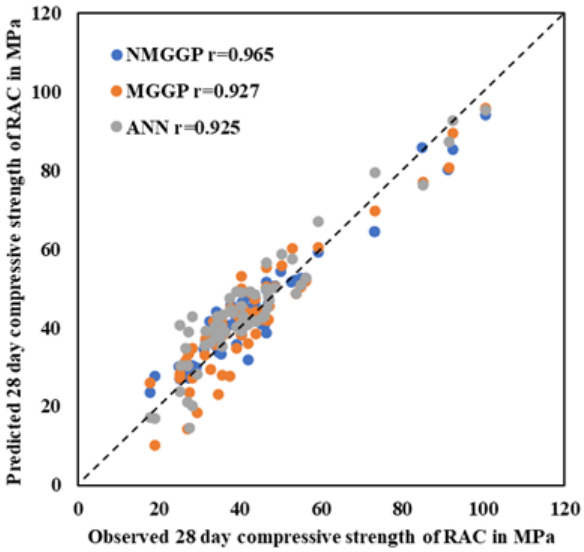

Fig. 7. Scatter plot for the model.

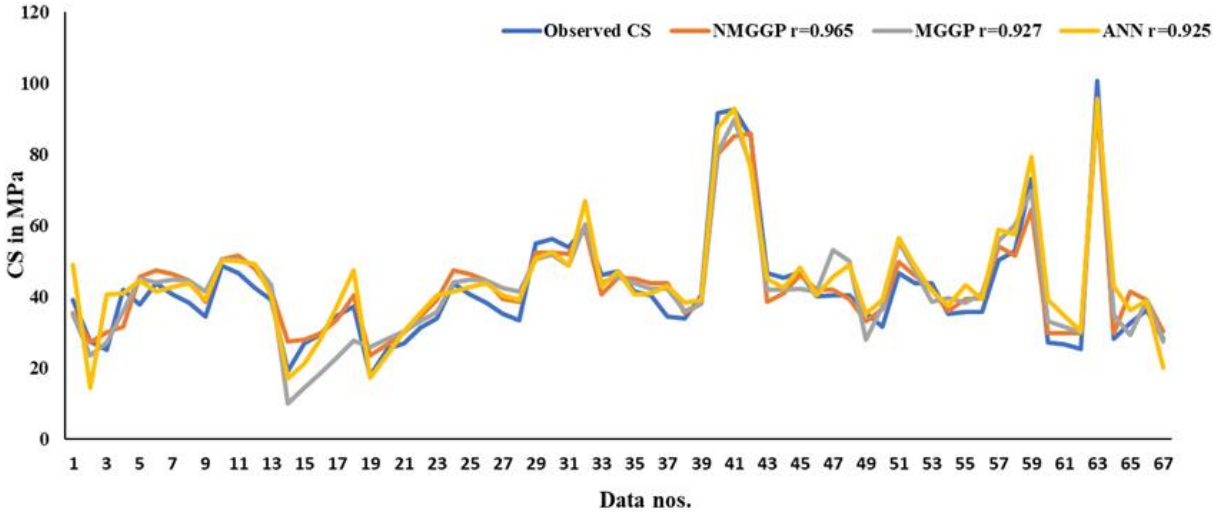

Fig. 8. Variations of observed and predicted compressive strength values.

Thus, the novel NMGGP technique integrates the interpretability of MGGP with the nonlinear learning capacity of ANN to provide a more accurate model for predicting the 28-day compressive strength of RAC. The reduction in prediction errors and improved correlation confirm the effectiveness of NMGGP framework and feature transformation. Importantly, this approach not only enhances accuracy but also ensures that the relationships among mix design parameters are better understood.

6. Conclusions

The present study proposes a novel hybrid framework: Neuro Genetic Programming framework (NMGGP), which integrates Multi-Gene Genetic Programming (MGGP) with Artificial Neural Networks (ANN) in a structured three-stage process. Within this framework, the most influential genes, representing optimized mathematical expressions obtained through standalone MGGP, are selected and used as transformed input parameters for the ANN. The ANN subsequently utilizes these inputs to enhance the accuracy of compressive strength prediction. The developed NMGGP model is applied for predicting the 28-day compressive strength of Recycled aggregate concrete (RAC) by using the mix design parameters as input parameters. The study shows that:

- The standalone MGGP and ANN models efficiently predict the 28-day compressive strength of RAC with a correlation coefficient of 0.927 with MGGP and 0.933 with ANN. Lower RMSE (MGGP:6.134 and ANN:6.134) and lower MAE (MGGP:5.067 and ANN:4.922)
- NMGGP outperforms Standalone ANN and MGGP models which can be seen through higher correlation coefficient of 0.965, lower RMSE (4.744) and MAE (3.944) values. NMGGP displays a 21.794% decrease of RMSE than that of standalone ANN and 19.566% decrease from standalone MGGP using NMGGP. Similarly, a 16.423 % and 22.163% decrease in MAE is seen for model developed using NMGGP technique and standalone ANN and standalone MGGP respectively. This highlights the effectiveness of feature transformation and hybridization in enhancing predictive performance.
- NMGGP is characterized by removing the genes with less weight and using only the informative genes termed as transformed inputs in the form of expressions, which add to the performance of the models. These informative transformed inputs with ANN can use the meaningful relations between them enhancing its predicting efficiency.
- The visual performance analysis of models in form of scatter plot and comparative graphs confirms the robustness and reliability of NMGGP by showing a balanced scatter and similar trends of predictions.

Acknowledgements

None declared.

Funding

The authors received no financial support for the research, authorship, and/or publication of this manuscript.

Conflict of Interest

The authors declared no potential conflicts of interest with respect to the research, authorship, and/or publication of this manuscript.

Author Contributions

All of the authors made substantial contributions to conception and design, or acquisition of data, or analysis and interpretation of data; were involved in drafting the manuscript or revising it critically for important intellectual content; and gave final approval of the version to be published.

Data Availability

The datasets created and/or analyzed during the current study are not publicly available, but are available from the corresponding author upon reasonable request.

REFERENCES

Adriana TAD, Monica BL, Koji de JN (2013). Prediction of compressive strength of concrete containing construction and demolition waste using artificial neural networks. *Construction and Building Materials*, 38, 717–722.

Bayazidi BM, Wang GG, Amir H, Alavi H, Gandomi AH (2014). Multigene genetic programming for estimation of elastic modulus of concrete. *Mathematical Problems in Engineering*, 2014, 474289.

Deshpande N, Londhe, S (2014). Modelling compressive strength of recycled aggregate concrete using neural networks and regression. *Challenge Journal of Concrete Research Letters*, 5(2), 15–21.

Duan ZH, Kou SC, Poon CS (2013). Prediction of compressive strength of recycled aggregate concrete using artificial neural networks. *Construction and Building Materials*, 40, 1200–1206.

Hamada BS, Dawib AH. (2017). Sustainable normal and high strength recycled aggregate concretes using crushed tested cylinders as coarse aggregates. *Case Studies in Construction Materials*, 7, 228–239.

Hsu KL, Gupta HV, Sorooshian S (1995). Artificial neural network modelling of the rainfall-runoff process. *Water Resource Research*, 31(10), 2517–2530.

Khademi F, Jamal SM, Deshpande N, Londhe S (2016). Predicting strength of recycled aggregate concrete using Artificial Neural Network, Adaptive Neuro-Fuzzy Inference System and Multiple Linear Regression. *International Journal of Sustainable Built Environment*, 5(2), 355–369.

Koza J (1992). Genetic Programming: On the Programming of Computers by Means of Natural Selection. A Bradford Book, MIT Press. London, England, 87–112.

Kulkarni PS, Londhe SN, Dixit PR (2019). A comparative study of concrete strength prediction using artificial neural network, multigene programming, and model tree. *Challenge Journal of Structural Mechanics*, 5(2), 42–61.

Legates DR, McCabe GJ (1999). Evaluating the use of 'goodness of fit' measures in hydrological and hydroclimatic model validation. *Water Resource Research*, 35(1), 233–224.

Li S, Xie E, Yang J (2022). Daily suspended sediment forecast by an integrated dynamic neural network. *Journal of Hydrology*, 604, 127–258.

Lin GF, Wu MC (2009). A hybrid neural network model for typhoon-rainfall forecasting. *Journal of Hydrology*, 375(3–4), 450–458.

MathWorks (2023). MATLAB. https://in.mathworks.com/products/matlab.html [accessed 01-04-2025].

Onyelowe KC, Gnananandara T, Ebid AM, Mahdi HA, Ghadikolaee MR, Al-Ajamee M (2022). Evaluating the compressive strength of recycled aggregate concrete using novel artificial neural network. *Civil Engineering Journal*, 8(8), 1700–1713.

Pan L, Wang Y, Li K, Guo X (2022). Predicting compressive strength of green concrete using hybrid artificial neural network with genetic algorithm. *Structural Concrete*, 24(2), 1980–1996.

Pandey DS, Pan I, Das S, Leahy JJ, Kwapinski W (2015). Multi-gene genetic programming based predictive models for municipal solid waste gasification in a fluidized bed gasifier. *Bioresource Technology*, 179, 524–533.

Rumelhart DE, Hinton GE, Williams RJ (1986). Learning representations by back-propagating errors. *Nature,* 323(6088), 533–536.

Searson DP (2015). GPTIPS 2: an open-source software platform for symbolic data mining. Chapter 22 in Handbook of Genetic Programming Application, New York, 551–573.

Shetty MS (2005). Concrete Technology, 17th ed. S. Chand and Company, New Delhi.

Sihag P, Sahar MK, Angelaki A (2019). Random forest, M5P and regression analysis to estimate the field unsaturated hydraulic conductivity. *Applied Water Science*, 9, 129.

Tran QV, Dang QV, Ho LS (2022). Evaluating compressive strength of concrete made with recycled concrete aggregates using machine learning approach. *Construction and Building Materials*, 343, 126578.

Zongjin Li (2011). Advanced Concrete Technology, 1st ed. John Wiley and Sons Inc., New Jersey.

Challenge Journal of Concrete Research Letters

Research Article

Experimental performance analysis of concrete-filled steel column to concrete-filled steel beam connections

Sadrettin Sancıoğlu [a,*], Abdulkerim İlgün [a], Serdar Çarbaş [b]

[a] *Department of Civil Engineering, KTO Karatay University, 42020 Konya, Türkiye*
[b] *Department of Civil Engineering, Karamanoğlu Mehmetbey University, 70200 Karaman, Türkiye*

ABSTRACT

Existing literature and practical engineering practice have comprehensively examined the behaviour of concrete-filled steel tubular (CFST) columns, CFST beams, and their associated connection systems involving either steel or reinforced concrete (RC) beams. Despite these advancements, limited research has focused on the direct beam–column interaction in fully CFST-to-CFST connection configurations. The absence of established design specifications and systematic experimental evidence has hindered the reliable adoption of such connections in structural applications. This feasibility study addresses this knowledge gap by conducting an integrated theoretical and experimental investigation into the structural performance of moment-resisting connections between CFST columns—locally strengthened with internal stiffening plates and configured with external bolted flange connections—and CFST beams of matching geometry. To provide a meaningful benchmark, a comparable hollow steel column–steel beam connection with identical cross-sectional dimensions and bolt arrangements was also evaluated. The experimental setup involved cyclic loading tests designed to capture load–rotation behaviour, quantify flexural stiffness, and identify critical limit states governing connection performance. Detailed measurements of moment–displacement response, local deformation patterns, and strain distribution were collected to assess connection rigidity, load-transfer mechanisms, and potential vulnerability to local buckling. The resulting data allowed for direct comparison between the proposed CFST-to-CFST connection configuration and the hollow steel reference specimen, enabling a clearer understanding of the composite action and confinement effects provided by the infilled concrete. The findings contribute foundational evidence for the feasibility of those moment connections and offer preliminary insights to support future analytical modelling, design recommendations, and full-scale implementation.

ARTICLE INFO

Article history:
Received – September 11, 2025
Revision requested – November 9, 2025
Revision received – November 14, 2025
Accepted – November 24, 2025

Keywords:
Concrete-filled steel tube
Hollow steel tube
Connection
Design code
Experimental analysis

Citation: Sancıoğlu S, İlgün A, Çarbaş S (2025). Experimental performance analysis of concrete-filled steel column to concrete-filled steel beam connections. *Challenge Journal of Concrete Research Letters*, 16(4), 215–224.

1. Introduction

Concrete has considerable compressive strength; however, it demonstrates restricted flexural resistance (Urtekin and Çelik 2025). Conversely, structural steel has enhanced bending capability due to its increased modulus of elasticity. The combination of these two distinct structural elements in a Concrete-Filled Steel Tube (CFST) system facilitates a composite action that proficiently unites the benefits of both materials, yielding enhanced overall structural performance (İlgün and Sancıoğlu 2023). Columns and beams may be implemented with CFST components. Concrete-filled steel elements exhibit a high axial compressive strength due to

* *Corresponding author*. Tel.: +90-444-12-51 ; E-mail address: sadrettin.sancioglu@karatay.edu.tr (S. Sancıoğlu)
ISSN: 2548-0928 / DOI: https://doi.org/10.20528/cjcrl.2025.04.004

the steel's ability to confine the concrete (Yıldız and Şermet 2025; Solak and Orhan 2023). Numerous literature studies have been conducted on concrete-filled steel stub columns to illustrate the cross-section effect and on concrete-filled long steel columns to illustrate the slenderness effect (Kandil et al. 2025; Al-Ani 2018; Ibañez et al. 2018; Liao et al. 2022; Na et al. 2018; Nakanishi et al. 1999; Schneider 1998). Concrete-filled steel beams exhibit a high flexural strength due to the fact that the concrete infill either prevents or delays local buckling. The effects of varying section widths/wall thicknesses, cross-sections, and materials on flexural strength have been demonstrated in literature studies (Abed et al. 2018; Chen et al. 2018; Han et al. 2006; İlgün and Sancıoğlu 2023; Kazemzadeh Azad et al. 2021; Lu and Kennedy 1994).

Recent literature indicates an increase in studies regarding connections between concrete-filled steel columns and steel beams, as well as those between concrete-filled steel columns and reinforced concrete beams. Several of these studies are mentioned as follows; the bolted connection (internal connection) of an H-section steel beam and a concrete-filled steel column was examined by Ye et al. (2021). In the investigation, they implemented two distinct categories of connections. The stiffening rib plate was passed through the column, brought to the opposite face, and welded in the first connection. The flange plates and shear plate were welded to the outside of the box cross-section. The rib plates and shear plates were welded to the column face in the second connection, while the flange plates were passed through the column, brought to the opposite face, and welded. Bolts were the only means of connecting the supports to the column. The investigation was implemented under both monotonic and cyclic loads conditions. The rigidity classification and ductility calculations of the connection were conducted based on the results obtained after monotonic loading, and load-displacement curves were obtained. The energy dissipation capacity of the connection was determined by obtaining moment-rotation curves based on the results obtained after cyclic loading. Wang et al. (2009) conducted an experimental study on a high-strength four-bolt moment-resisting internal beam-column connection subjected to cyclic loading. The study utilized square and rectangular concrete-filled steel columns, as well as H-section steel beams. The variable parameters of the experimental investigation were identified as column section type, column wall thickness, and end plate. The conducted experiments examined the failure mechanism, stiffness, and energy dissipation capacity of the beam-column connection. The experimental investigation determined that the moment-rotation relationship satisfied the essential requirements of international standards, and the strain dissipation and energy dissipation capacities were at the acceptable levels. The findings indicate that the high-strength four-bolt moment-resisting beam-column connection suggested in the study is suitable for application in moment-resisting frame systems. Chen et al. (2014) investigated the seismic performance of a through-beam connection connecting concrete-filled steel tubular (CFST) columns with reinforced concrete (RC) beams. Six specimens were testing under cyclic lateral loading to simulate seismic impacts, subsequently followed by axial compression tests. The findings indicated that the suggested connection had consistent hysteretic behaviour, excellent ductility, and significant energy dissipation capacity. Despite the decrease of stiffness and strength with repeated loading, the overall seismic performance was acceptable. The addition of a reinforcing circular beam adequately reduced the decrease in axial load capacity resulting from the discontinuity of the steel tube at the connection area. Parametric and finite element calculations demonstrated that the reinforcement ratio and axial compressive force significantly impact performance. The study shows that the through-beam connection offers dependable earthquake protection and is applicable in practical engineering with suitable details. Qu et al. (2023) proposed an assembly connection between an H-shaped steel beam and a CFST column and evaluated its seismic behaviour through experiments and finite element modelling. Parametric analyses showed that increasing the end-plate thickness and bolt diameter improves both load-carrying and energy dissipation capacities. The study also demonstrated effective interaction between the connector and concrete, confirming the feasibility of this assembly connection for engineering applications and providing a formula for its bending capacity. Özkılıç (2023) investigated the behaviour of unstiffened extended end-plate connections including thin plates and big bolts by experimental testing and comprehensive numerical analysis. Six specimens performed testing under cyclic and monotonic loads, with end-plate thickness selected as the primary experimental variable to ensure bending-controlled failure. A thorough numerical investigation of 156 finite element models examined the impact of geometric and connection characteristics. The findings indicate that thin end-plates exhibit considerable ductility and strength, although AISC 358-16 and EN1993-1-8 substantially underestimate the plastic moment capacity. Experimental and numerical capabilities exceeded code projections by factors of up to 3.93. A novel yield-line-based formula was introduced, decreasing the real-to-predicted moment capacity ratio to roughly 1.23–1.29, signifying significantly enhanced accuracy. The connections between concrete-filled steel columns and concrete-filled steel beams were investigated by Sancıoğlu (2025) analytically, numerically, and experimentally. Four different connection types were examined within the scope of the study. To enable comparison of moment-carrying performance, the same connection configurations were also tested using hollow steel columns and hollow steel beams. In total, eight specimens—four hollow column–hollow beam connections and four concrete-filled column–concrete-filled beam connections—were subjected to cyclic loading. Based on the experimental data obtained from the cyclic loading tests, the stiffness, moment–rotation behaviour, load–displacement responses, energy dissipation capacity, ductility ratios, performance levels, and failure modes of the connections were evaluated. The performance of each connection type was compared both internally and against the corresponding concrete-filled specimens. Additionally, the experimental results were simulated using the finite element–

based software ABAQUS and compared with the numerical findings. The results demonstrated that the connections composed of concrete-filled steel columns and concrete-filled steel beams exhibited higher load-carrying capacity than their hollow counterparts, achieved the plastic moment capacity specified in the Turkish Steel Structures Regulation (2018), and showed behaviour consistent with the numerical analyses.

As abovementioned in detail, the literature reviews and field applications involve concrete-filled steel columns, concrete-filled steel beams, connections between concrete-filled steel columns and steel beams, and connections between concrete-filled steel columns and reinforced concrete beams. Nonetheless, there are no investigations on the connection between concrete-filled steel columns and concrete-filled steel beams. This pre-study aims to both theoretically and experimentally examine the connection between concrete-filled steel columns with stiffening plates and bolts and concrete-filled steel beams. A hollow steel column-steel beam connection with identical cross-sectional parameters was also examined to compare the concrete-filled steel column and concrete-filled steel beam connections. The experimental investigation provided data for the analysis of moment-displacement curves and the failure modes of the connection.

2. Materials and Method

2.1. Materials

The concrete utilized in the concrete-filled steel columns and beams for the experimental studies was produced in the Structural Mechanics Laboratory of the Civil Engineering Department at KTO Karatay University, according to TS 802 (2016). Three categories of crushed rock aggregates, specifically 0–4 mm, 4–11.2 mm, and 11.2–16 mm, were utilized in concrete manufacturing. Portland cement 42.5 was utilized as the cementing agent. The quantity of additives was designated as 1% of the cement weight. The use of a resin additive resulted in a decrease in both cement and water quantities while preserving the water/cement ratio. Three cubic specimens measuring 150×150×150 mm were extracted from the manufactured concrete for strength evaluation. The specimens underwent water curing for 28 days in a controlled laboratory setting. The cube specimens placed in water for 28 days performed a uniaxial compressive strength test. A uniaxial compressive strength test was performed using a concrete testing press with a capacity of 2000 kN. The test loading rate was established as an average of 0.6 MPa/s, according to the minimum and maximum values specified in TS EN 12390-3 (2019). The mean compressive strength of the concrete specimens was 30.02 MPa. According to Section 12.2.3 of the Turkish Steel Structures Regulation (2018), the compressive strength of concrete used in composite members must fall within the range of 20 MPa to 70 MPa. Therefore, the concrete produced for this study satisfies the specified strength requirements and is deemed suitable for use. The steel cross-sectional dimensions of the columns and beams used in the study were 100×100×3 mm, the column length was 1500 mm, and the beam length was 1000 mm. These dimensions were chosen due to the cost, transportation, and testing difficulties associated with larger column and beam sections. Considering the actual size, the columns are 4500 mm long and the beams are 6000 mm long. Because the internal column-beam joint will be loaded at the centre of the column and the centre of the beam, the test specimens were scaled at a 1:3 ratio. Also, the wall thickness of the connection plates was 5 mm. Three coupon test specimens from each steel group were procured and evaluated according to with TS EN ISO 6892-1 (2020). The structural steel specimens performed tensile testing using a fully automated steel tensile machine with a capacity of 1000 kN. The average yield strength of the structural steel with a wall thickness of 3 mm was 290 MPa, whereas that of the 5 mm wall thickness structural steel was 265 MPa. Additionally, the 8 mm diameter bolts used in the connections had a yield strength of 680 MPa.

In this study, 8.8-grade and 150-mm long bolts were used between the upper and lower surfaces of the columns and beams to ensure load transfer and to address the discontinuity of concrete in the column–beam connection zone. Connection plates and rib plates were also employed in the connections. This connection design, which was originally developed for concrete-filled column–beam joints, was similarly applied to the steel column–beam joints to enable a direct comparison with the hollow steel column–beam connections. Since the established connection type was not previously defined in existing standards or codes, the limitations of the connection were determined based on the relevant criteria outlined in current design standards and regulations. The hole diameters for the M8 bolts used in the study were designed according to Table 13.8 of the principles of design, calculation, and construction of steel structures so-called Turkish Steel Structures Regulation (2018). According to this table, the standard hole diameter for M16 and M24 bolts is set at 2 mm larger than the bolt diameter. However, there is no specific value provided for M8 bolts. Therefore, the diameter of the holes for the M8 bolts was determined as 10 mm. Furthermore, according to Section 13.3.6 of the same regulation, the minimum centre-to-centre distance between standard circular holes, denoted as s, must not be less than three times the nominal bolt diameter, d. Based on this requirement, the minimum bolt spacing for M8 bolts was established as 24 mm. Through this approach, the study ensured that the connection design met the geometric and mechanical requirements defined by national standards, while enabling consistent comparison between different column–beam configurations, including concrete-filled, steel, and hollow steel connections. L-shaped plates were fastened to both the top and bottom flanges of the beam using bolts. Six rib plates were utilized in the L-shaped plates, with three positioned on the bottom and three on the top. The beam was fastened to the column using 12 bolts stretching from the top flange to the bottom flange of the column. The lower flange of the column was reinforced by a supporting connection plate to prevent local buckling during the torque of bolts. Furthermore, six holes

were created on each side of the column and three holes on each side of the beam to help distribute the shear force. Shear plates, extending from the column's lateral surfaces to the beam's lateral surfaces, were fastened to these holes. The connection was established utilizing bolts along the lateral surfaces of the column and beam. Fig. 1 presents specifications of the L-shaped plate connection and dimensions of the L-plate.

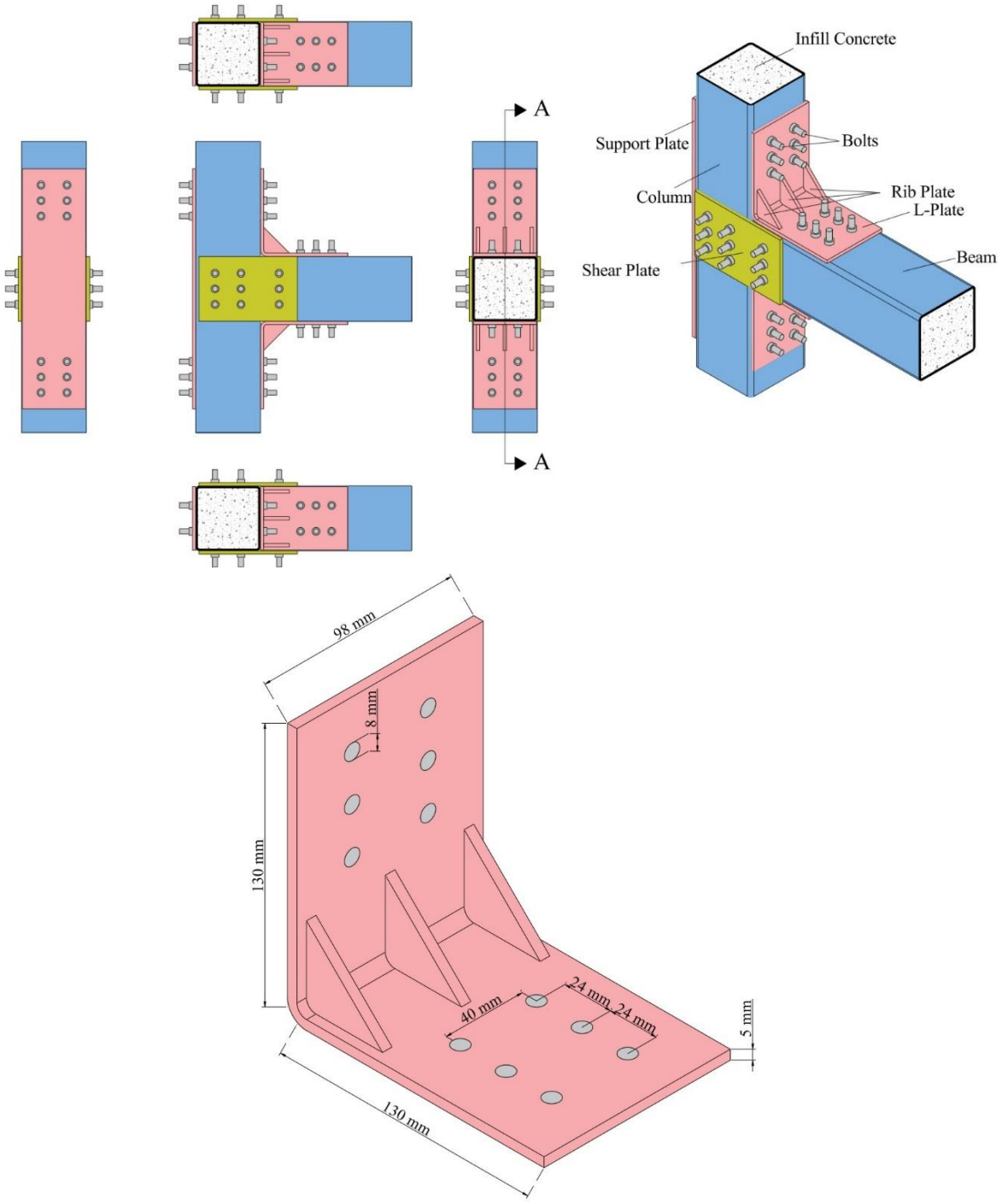

Fig. 1. L-shaped plate connection.

2.2. Method

2.2.1. Theoretical study

A square steel box profile with a cross-sectional property of 100×100×3 mm was selected as the beam section. Thin-walled steel beams must be classified for local buckling according to Turkish Steel Structures Regulation (2018) Section 5.4. The selected beam section is in the compact class. The bending moment strengths for the yield limit states of compact and box-section bending members are calculated according to Turkish Steel Structures Regulation (2018) Section 9.7.1. The bending moment strength for the yield limit state is obtained by multiplying the steel yield strength, F_y, by the plastic moment of strength, W_p. The calculation formula is given in Eq. (1).

$$M_n = M_p W_p \quad (1)$$

A square steel box profile with a cross-sectional property of 100×100×3 mm was selected as the beam section. Concrete-filled steel beams must be classified for local buckling according to Turkish Steel Structures Regulation (2018) Section 12.2.4. Accordingly, the selected beam section is classified as compact. Since the element meets the compact cross-section condition, the characteristic bending moment strength, M_n, was calculated according to Eq. (2).

$$M_n = M_p \quad (2)$$

According to Turkish Steel Structures Regulation (2018) Table 12.4, M_p was calculated according to M_B, where the axial force is taken as zero. M_B is obtained from the interaction diagram developed for composite elements. The calculation formula for M_B is given in Eq. (3). The nominal moment of strength for steel is given in Eq. (4), and for concrete is given in Eq. (5). The location of the neutral axis is given in Eq. (6). The value of the moment at point D in the interaction diagram developed for composite elements is calculated using Eq. (7). The moment of strength of the concrete within the box section is calculated using Eq. (8). To generate moment-displacement graphs, the load and displacement data obtained from the experimental study must be converted into moment and displacement values. Accordingly, moment values, M, were obtained by multiplying the load values given at the beam end, P, by the beam length, L (Fig. 2(c)). The calculation method is given in Eq. (9).

$$M_B = M_D - W_{sn} \cdot F_y - \frac{1}{2} W_{cn}(0.85 \cdot f_{ck}) \quad (3)$$

$$W_{sn} = 2 \cdot t \cdot h_n^2 \quad (4)$$

$$W_{cn} = b_i \cdot h_n^2 \quad (5)$$

$$h_n = \frac{0{,}85 \cdot f_{ck} \cdot A_c}{2[0.85 \cdot f_{ck} \cdot b_i + 4 \cdot t \cdot F_y]} \leq \frac{h_i}{2} \quad (6)$$

$$M_D = W_{px} \cdot F_y + \frac{W_c}{2} W_{cn}(0.85 \cdot f_{ck}) \quad (7)$$

$$W_c = \frac{b_i \cdot h_i^2}{4} - 0.192 \cdot r_i^3 \quad (8)$$

W_{px} = Plastic strength moment of box cross-section according to x-axis

$$M = P \cdot L \quad (9)$$

2.2.2. Experimental study

The experimental setup was established in the Structural Mechanics Laboratory of the Civil Engineering Department of the Faculty of Engineering and Natural Sciences at KTO Karatay University. The experimental setup will utilize hydraulic jacks with 300 and 600 kN load capacities for load application, load cells with 300 and 600 kN capacities for load measurement, linear variable displacement meters (LVDTs) for measuring displacements at column midpoints, beam top endpoint displacements, and beam bottom endpoint displacements. A 2×8-channel static data logger device will be used to collect data during the experiment. The experimental setup is shown in Figs. 2(a) and Fig. 2(b), while the moment-displacement relationship is illustrated in Fig. 2(c).

A review of literature studies reveals that in column-beam connection tests, the columns are subjected to an axial load corresponding to a certain percentage (25–30%) of their axial load-carrying capacity (Ye et al. 2021). In the test, the columns were subjected to an axial load corresponding to approximately 25% of the column's axial load-carrying capacity. This value was approximately 75 kN for hollow specimens and 120 kN for concrete-filled specimens. Cyclic loading was applied using a hydraulic press attached to the beam end. Loading was performed using displacement control according to the values recommended in FEMA-350 Section 3.9.1. The displacement-controlled loading protocol prepared according to FEMA-350 (2000) Section 3.9.1 is shown in Fig. 3.

3. Results and Discussion

3.1. Moment-displacement curves

The cyclic loading test was conducted to investigate the hysteretic behaviour and deformation characteristics of both hollow and concrete-filled beam specimens at their connection regions. During the initial twenty-eight loading cycles, the analysis of moment and displacement values indicated that the connection remained entirely within the elastic range. In this phase, the applied load was fully recoverable upon unloading, and no residual deformation was detected in either the beam or the column. This behaviour confirmed that both materials exhibited a stable elastic response under cyclic loading and unloading conditions. The structural integrity of the connection was thus maintained during the early cycles. After the twenty-eighth cycle, when the displacement reached –30 mm, local buckling was observed in the connection plate. The onset of local buckling occurred as the actuator reversed from the –30 mm displacement, at which point the moment dropped to zero. This sudden loss of load-carrying capacity signified a transition from the elastic to the plastic domain, where the connection began to experience permanent deformation. The formation of local buckling indicated the initiation of instability within the connection plate, which served as the primary locus of inelastic behaviour. Despite this, no permanent deformation was observed in the main body of the beam or column, implying that the damage was localized rather than global. Following the occurrence of local buckling, the moment–displacement behaviour exhibited a clear asymmetry.

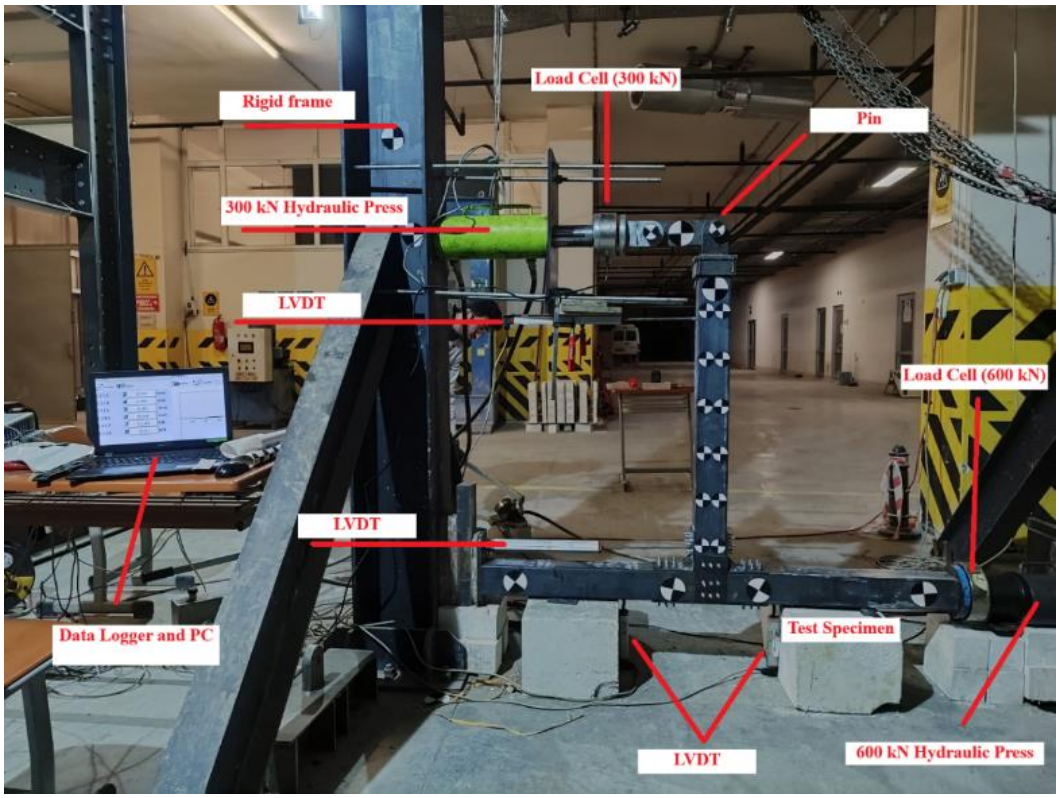

(a) Experimental setup

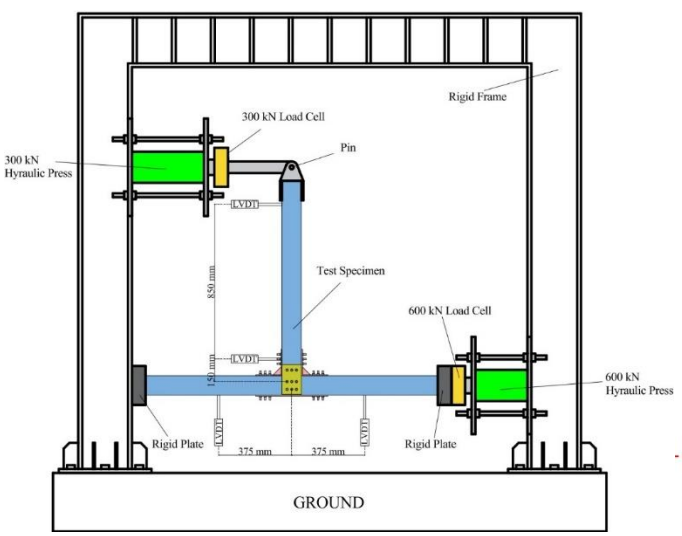

(b) Experimental setup (2D)

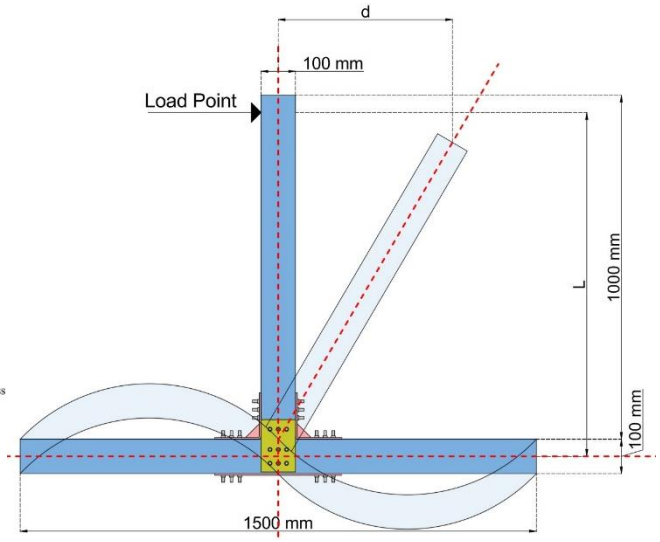

(c) Moment–displacement relationship

Fig. 2. Details of the experimental test setup.

The moments corresponding to equal displacements in the positive and negative directions differed, reflecting the degradation in stiffness and strength in the buckling direction. Such asymmetry is a characteristic feature of cyclic degradation, where the accumulation of plastic strains alters the structural response during subsequent moment reversals. For the hollow specimen, the maximum positive moment was recorded as 3.74 kNm at a displacement of 67.98 mm, while the maximum negative moment reached 5.01 kNm at 68.82 mm displacement. The discrepancy between these values was attributed to local buckling at the connection region, which reduced the moment-carrying capacity in the direction of deformation. This indicates that the hollow section exhibited a progressive stiffness reduction once local instability developed. Nevertheless, no permanent deformation or visible damage was detected in the column or beam, confirming that the failure mechanism was confined to the connection plate. In contrast, the concrete-filled specimen demonstrated a significantly improved performance.

The maximum positive moment reached 6.33 kNm at a displacement of 70.53 mm, and the maximum negative moment was 6.39 kNm at 72.28 mm displacement. The near-symmetry of these values suggests that local buckling in the concrete-filled specimen occurred simultane-

ously in both directions after the maximum moment had been attained. The concrete infill delayed the onset of local buckling and contributed to a more uniform and stable hysteretic response. Moreover, the presence of concrete enhanced the stiffness and energy dissipation capacity of the specimen by providing lateral confinement and delaying instability in the steel plate. When the performance of the two specimens is compared, the concrete-filled beam exhibited a 1.69 times higher moment capacity in the positive direction and 1.28 times higher in the negative direction compared to the hollow specimen (Table 1). This considerable improvement in strength and deformation capacity can be attributed to the composite action between the steel section and the concrete core. The infill effectively stabilized the local plate buckle and increased the ductility of the system under cyclic loading. As illustrated in Fig. 4, the moment–displacement curves of both specimens reveal distinct hysteresis loops. The hollow specimen showed a rapid reduction in stiffness and moment capacity following buckling, whereas the concrete-filled specimen maintained a stable response with wider hysteresis loops, indicating superior energy absorption. These findings confirm that concrete infill plays a critical role in enhancing both the ductility and cyclic load resistance of steel beam connections subjected to repeated lateral loading.

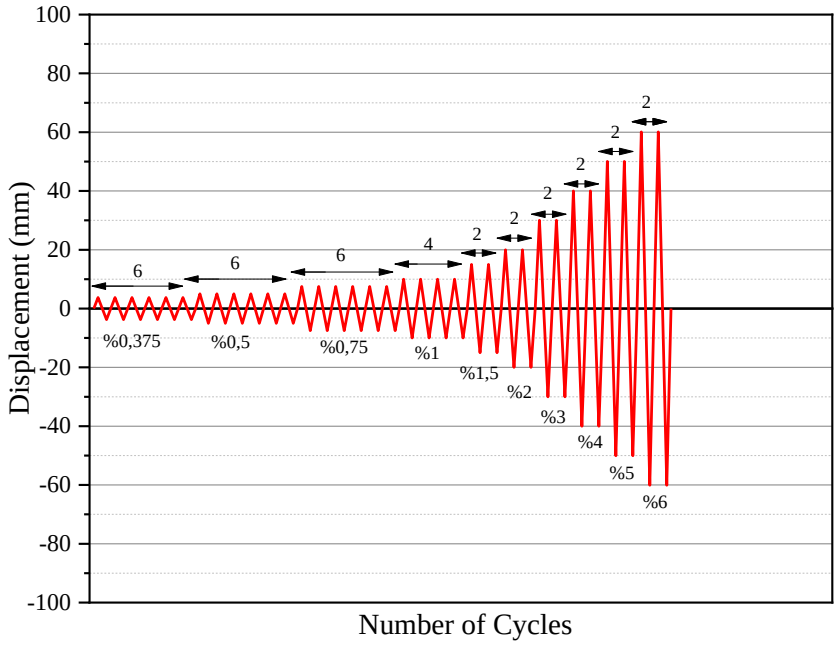

Fig. 3. Displacement-controlled loading protocol.

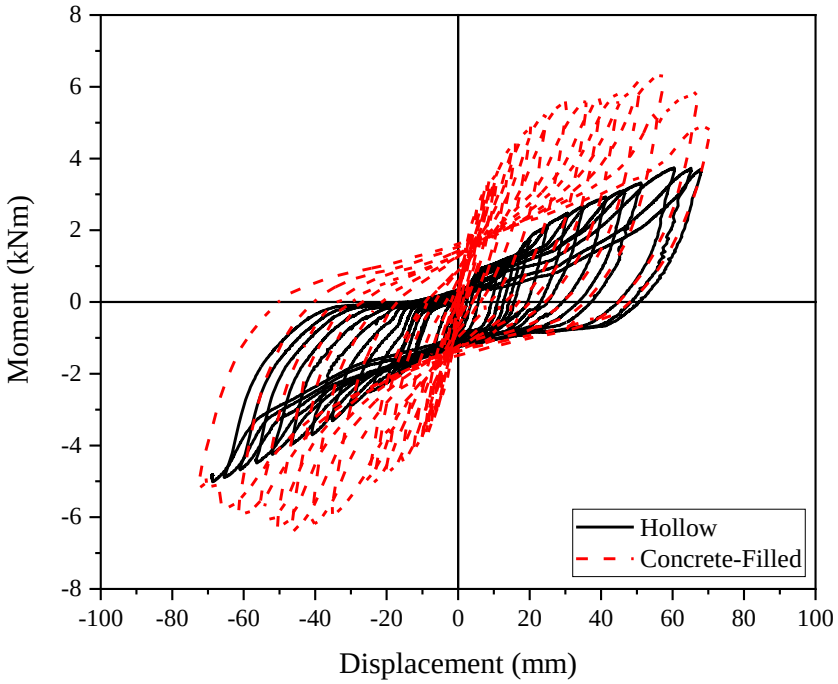

Fig. 4. Moment–displacement curves of the specimens.

Table 1. Comparison between theoretical and experimental results.

	Theoretical results		Experimental results		Experimental / Theoretical	
	Positive maximum moment (kNm)	Negative maximum moment (kNm)	Positive maximum moment (kNm)	Negative maximum moment (kNm)	Positive	Negative
Hollow	11.98	11.98	3.74	5.01	0.31	0.42
Concrete-Filled	13.35	13.35	6.33	6.39	0.47	0.48

3.2. Failure modes

Experimental observations revealed significant local buckling behaviour in both hollow and concrete-filled beam–column connection specimens. In the case of the hollow specimens, local buckling was observed at the connection plates on both the front and back sides of the specimens. This behaviour was primarily attributed to the interaction between the beam and the column during the moment transfer process. As the beam deformed under increasing moment, the column attempted to rotate at the joint, generating localized compressive stresses that exceeded the elastic limit of the connecting plates, thereby initiating local buckling. In the hollow specimens, the onset of local buckling was strongly influenced by the insufficient stiffness of the connection plates and the failure of the bolted joints in the near of the buckled region. These deficiencies caused the plates to lose their elastic response and undergo plastic deformation, significantly reducing the connection stiffness. Consequently, the beam was unable to attain its theoretical moment-bearing capacity, and no local buckling was observed in either the beam or the column members themselves. Instead, the failure was concentrated in the connection region, leading to premature failure before the beam could reach its full moment-carrying capacity.

This observation clearly indicates that the connection stiffness and detailing play a critical role in the overall structural response and moment-transfer efficiency of such assemblies. Conversely, in the concrete-filled specimens, local buckling was again observed in the connection plates at both the front and back sides. The mechanism of buckling formation was similar to that in the hollow specimens: interaction between the beam and column during moment transfer induced rotational movement and local compressive stresses in the connection region. However, the onset of buckling occurred at a later stage in the concrete-filled specimens compared to the hollow ones. This delay is attributed to the increased stiffness and confinement effect provided by the infilled concrete, which enhanced the local stability of the steel components and delayed the transition from elastic to plastic behaviour. Despite this improvement, the absence of bolted connections in the region where buckling developed, together with the insufficient thickness of the stiffening plates, caused the connection plates to lose elasticity and enter a plastic state. As a result, the beam again failed to achieve its full moment-carrying capacity, and no local buckling was observed in either the beam or the column. The failure mechanism was dominated by the local buckling and plastic deformation occurring at the connection, which hindered proper moment transfer and resulted in partial system failure. Although both specimen types of experienced connection failure due to local buckling, the delayed occurrence in the concrete-filled specimens indicates a superior energy absorption and ductility capacity characteristic of composite elements. The concrete infill increased the confinement of the steel section, thereby improving its resistance to local instability. Nevertheless, since the observed buckling occurred mainly in the connection region rather than along the beam itself, the connection configuration remained the weak point of the system. This suggests that the global performance of the structure was limited by the local instability of the joint region, rather than by the strength of the beam or column members. In summary, the experimental findings emphasize the necessity of improving connection stiffness, plate thickness, and bolt arrangement in order to delay or prevent local buckling and enhance moment transfer efficiency.

Although concrete-filled specimens demonstrated better performance through delayed buckling and improved stability, both connection types ultimately failed due to insufficient local strength in the connecting plates. Future designs should therefore focus on optimizing connection geometry and employing adequately stiffened connection plates to achieve higher moment-carrying capacity and greater structural resilience. Figs. 5(a) and 5(b) illustrate the failure modes observed in the connections of the hollow specimens after cyclic loading, showing the front and back faces, respectively. Figs. 5(c) and 5(d) present the corresponding failure modes for the concrete-filled specimens, also showing the front and back faces.

4. Conclusions

In this study, the connection between concrete-filled steel columns with stiffening plates and bolts and concrete-filled steel beams was investigated with theoretical studies and experimental tests. A total of two specimens were tested experimentally, one hollow test specimen and the other concrete-filled test specimen. Experimental results were compared with theoretical results obtained from code. The main results obtained from testing a limited number of test elements are listed below as so-called bullet points:

- Experimental data demonstrated that concrete-filled specimens had a significantly higher moment-carrying capacity compared to hollow specimens. This suggests that the concrete infill enhances the rigidity of

the connection components and encourages a more uniform stress distribution inside the cross-section. The concrete infill enhances stability in the connecting area by delaying local buckling.

- Upon comparing the theoretical analysis results with the results of the experiment, it was concluded that the investigated connection type can transmit a particular amount of moment; however, this transmission is inadequate for the design requirements. The connection geometry and weld specifications are believed to impose a constraint on the moment-carrying capacity.
- Moreover, it was determined that if the connection were utilized in its existing configuration, local buckling in the beam would occur in the connection region prior to the achievement of the beam's moment capacity. This suggests that the connection element demonstrates behaviour that may adversely impact its moment-bearing capacity and result in premature system failure. Consequently, it was determined that the connection specifications require enhancement, and supplementary measures must be implemented to augment the moment-carrying capability.

Future research seeks to duplicate the stiffening plate by increasing its size, modifying the concrete infill class, varying the steel cross-sections, varying the dimensions of the connection parts, varying the bolt class, and experimenting with other connection types.

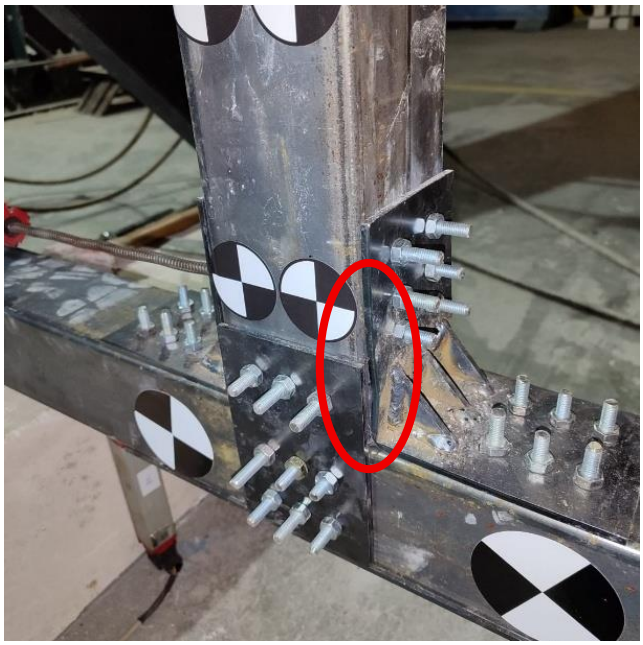

(a) Hollow connection (front)

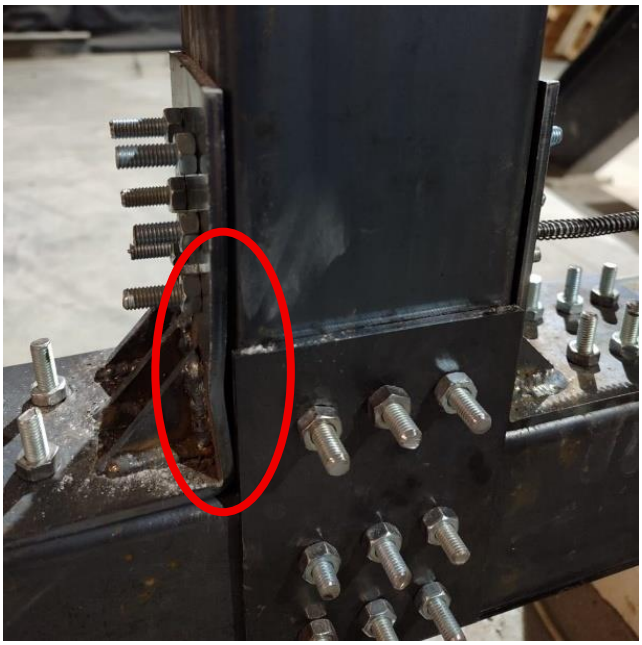

(b) Hollow connection (back)

(c) Concrete-filled connection (front)

(d) Concrete-filled connection (back)

Fig. 5. Failure modes in the connections of the hollow specimens after cyclic loading.

Acknowledgements

None declared.

Funding

This research was supported by Scientific Research Projects Commission of KTO Karatay University, Konya, Türkiye under grant number 10092430.

Conflict of Interest

The authors declared no potential conflicts of interest with respect to the research, authorship, and/or publication of this manuscript.

Author Contributions

All of the authors made substantial contributions to conception and design, or acquisition of data, or analysis and interpretation of data; were involved in drafting the manuscript or revising it critically for important intellectual content; and gave final approval of the version to be published.

Data Availability

The datasets created and/or analyzed during the current study are not publicly available, but are available from the corresponding author upon reasonable request.

REFERENCES

Abed FH, Abdelmageed YI, Ilgun A (2018). Flexural response of concrete-filled seamless steel tubes. *Journal of Constructional Steel Research*, 149, 53–63.

Al-Ani YR (2018). Finite element study to address the axial capacity of the circular concrete-filled steel tubular stub columns. *Thin-Walled Structures*, 126, 2–15.

Chen QJ, Cai J, Bradford MA, Liu X, Zuo ZL (2014). Seismic behaviour of a through-beam connection between concrete-filled steel tubular columns and reinforced concrete beams. *Engineering Structures*, 80, 24–39.

Chen Y, Feng R, Gong W (2018). Flexural behavior of concrete-filled aluminum alloy circular hollow section tubes. *Construction and Building Materials*, 165, 173–186.

FEMA-350 (2000). Recommended seismic design criteria for new steel moment-frame buildings. Federal Emergency Management Agency, Washington, DC, USA.

Han L-H, Lu H, Yao G-H, Liao F-Y (2006). Further study on the flexural behaviour of concrete-filled steel tubes. *Journal of Constructional Steel Research*, 62, 554–565.

Ibañez C, Hernández-Figueirido D, Piquer A (2018). Shape effect on axially loaded high strength CFST stub columns. *Journal of Constructional Steel Research*, 147, 247–256.

İlgün A, Sancıoğlu S (2023). Flexural behaviour of different CFSTs cross-section shapes with the same steel cross-sectional area. *Sādhanā*, 48, 53.

Kandil K, El-Shami M, Hekal G, ElGouhary O (2025). Behavior of multicell steel columns under impact loading. *Challenge Journal of Concrete Research Letters*, 16(2), 95-114.

Kazemzadeh Azad S, Li D, Uy B (2021). Compact and slender box concrete-filled stainless steel tubes under compression, bending, and combined loading. *Journal of Constructional Steel Research*, 184, 106813.

Liao JJ, Zeng JJ, Long YL, Cai J, Ouyang Y (2022). Behavior of square and rectangular concrete-filled steel tube (CFST) columns with horizontal reinforcing bars under eccentric compression. *Engineering Structures*, 271, 114899.

Lu YQ, Kennedy DJL (1994). The flexural behaviour of concrete-filled hollow structural sections. *Canadian Journal of Civil Engineering*, 21, 111–130.

Na L, Yiyan L, Shan L, Lan L (2018). Slenderness effects on concrete-filled steel tube columns confined with CFRP. *Journal of Constructional Steel Research*, 143, 110–118.

Nakanishi K, Kitada T, Nakai H (1999). Experimental study on ultimate strength and ductility of concrete filled steel columns under strong earthquake. *Journal of Constructional Steel Research*, 51, 297–319.

Özkılıç YO (2023). Cyclic and monotonic performance of unstiffened extended endplate connections having thin end-plates and large-bolts. *Engineering Structures*, 281, 115794.

Qu X, Xie Y, Sun G, Liu Q, Wang H (2023). Seismic behavior of assembly joint with CFST column and H-shaped steel beam. *KSCE Journal of Civil Engineering*, 27(2), 670–683.

Sancıoğlu S (2025). Experimental Investigation on Moment Carrying Capacity of Column – Beam Connections Consisting of Concrete-Filled Steel Composite Members. *Ph.D thesis*, KTO Karatay University, Konya, Türkiye.

Schneider SP (1998). Axially loaded concrete-filled steel tubes. *Journal of Structural Engineering*, 24, 1125–1138.

Solak K, Orhan S (2023). Axial compression behaviour of concrete-filled auxetic tubular short columns. *Challenge Journal of Concrete Research Letters*, 14(1), 1-9.

TS 802 (2016). Calculation principles of concrete mix design. Turkish Standards Institute, Ankara, Türkiye.

TS EN 12390-3 (2019). Testing hardened concrete – Part 3: Compressive strength of test specimens. Turkish Standards Institute, Ankara, Türkiye.

TS EN ISO 6892-1 (2020). Metallic materials – Tensile testing – Part 1: Method of test at room temperature. Turkish Standards Institute, Ankara, Türkiye.

Turkish Steel Structures Regulation (2018). Principles of design, calculation, and construction of steel structures. Republic of Türkiye Ministry of Environment, Urbanization, and Climate Change, Ankara, Türkiye.

Urtekin Y, Çelik Z (2025). Investigation of the effects of re-curing on mechanical properties of basalt-polypropylene hybrid fiber concretes after exposure to high temperature. *Challenge Journal of Structural Mechanics*, 11(1), 14-23.

Wang JF, Han LH, Uy B (2009). Hysteretic behaviour of flush end plate joints to concrete-filled steel tubular columns. *Journal of Constructional Steel Research*, 65, 1644–1663.

Ye Q, Wang Y, Wang Z, Lin Y, Shu C, Zhang F (2021). Experimental study of through diaphragm bolted joint between H-beam to CFST column. *Journal of Constructional Steel Research*, 182, 106647.

Yıldız Y, Şermet F (2025). Impact of composite columns on soft and weak storey irregularities in buildings without ground floor infill walls. *Challenge Journal of Structural Mechanics*, 11(2), 70-81.

Challenge Journal of Concrete Research Letters

Review

Evolutionary process and mechanical properties of polymers: A comprehensive review

Shahnizan Imran Mohd Nazri [a], Nur Farhayu Ariffin [a,*], Mohamad Firdaus Mohamad Borhan [a]

[a] *Faculty of Civil Engineering Technology, Universiti Malaysia Pahang Al-Sultan Abdullah, 26300 Kuantan, Pahang, Malaysia*

ABSTRACT

The growing demand for innovative construction materials has driven the exploration of polymer-based composites due to their enhanced mechanical performance and potential environmental benefits. However, a clear understanding of the historical development, classification, and structural behavior of polymers in construction remains limited. This review aims to bridge this gap by synthesizing current knowledge on the historical evolution, mechanical benefits, chemical benefits, drawbacks and real world applications of polymers in construction. The study focuses on key thermosetting resins such as polyester, epoxy, vinyl ester, and PET and assesses their mechanical properties relevant to structural applications. To address the lack of integrated insight in the literature, the review compiles and compares data from various primary sources. Mechanical properties such as tensile, compressive, and flexural strength are evaluated to determine the suitability of each polymer for construction use. The outcomes indicate that epoxy resins demonstrate superior tensile and flexural strength, while polyester and polyethylene terephthalate PET offer notable advantages in compressive resistance and sustainability. Overall, the findings provide a consolidated understanding of polymer development and performance, offering valuable guidance for researchers and engineers aiming to enhance material efficiency, durability, and environmental responsibility in the construction industry.

ARTICLE INFO

Article history:
Received – May 23, 2025
Revision requested – July 14, 2025
Revision received – July 24, 2025
Accepted – August 5, 2025

Keywords:
Polymer concrete
Polymer evolution
Advanced composite materials
Sustainability
Construction industry

Citation: Mohd Nazri SI, Ariffin NF, Mohamad Borhan MF (2025). Evolutionary process and mechanical properties of polymers: A comprehensive review. *Challenge Journal of Concrete Research Letters*, 16(4), 225–242.

1. Introduction

The rapid industrialization of the modern era has led to an increased demand for materials that are not only strong and lightweight but also flexible and durable. Historically, natural polymers such as rubber, wool, cotton, and silk were widely used to meet these needs. However, their limited availability, high costs, and inconsistent performance posed significant challenges. One of the primary concerns was the scarcity and expense of natural rubber, which prompted researchers to explore synthetic alternatives. This shift led to the rapid expansion of the polymer industry following World War II, resulting in the development of various synthetic plastics such as polyethylene, polystyrene, and polyvinyl chloride (PVC) (Feldman 2008). These materials quickly gained popularity due to their affordability, versatility, and broad applicability in industries ranging from packaging and household appliances to construction.

Polymers, in essence, are materials that can be molded into various shapes during manufacturing, making them essential structural components in a wide range of applications. They consist of one or more types of synthetic or chemically modified natural polymers, which are built from individual functional units known as monomers and combined with chemical additives (Seewoo et al. 2024). A monomer is a small molecule that bonds with others to form a larger structure, creating a polymer, a macromolecule composed of repeated subunits. The structural arrangement of polymers influences

* *Corresponding author*. E-mail address: farhayu@umpsa.edu.my (N. F. Ariffin)
ISSN: 2548-0928 / DOI: https://doi.org/10.20528/cjcrl.2025.04.005

their physical properties, such as strength, transparency, and flexibility. For instance, polymers containing ethylene and terephthalate can exist in different forms amorphous, semi-crystalline, or colorless depending on their molecular organization (Soni et al. 2024). The ability to manipulate polymer structure and composition has allowed for the development of materials with enhanced mechanical and chemical properties tailored to specific applications.

Due to their diverse properties, polymer materials are selected based on various factors, including strength, flexibility, resistance to corrosion, thermal stability, electrical conductivity, and cost. In addition to performance requirements, material selection is influenced by safety concerns such as the risks associated with monomers, their potential migration in food-contact plastics, and the presence of additives or microplastics (Seewoo et al. 2024). Commonly used polymers such as polyethylene, polypropylene, polystyrene, PVC, and nylon have been widely integrated into industrial and consumer applications, with ongoing research dedicated to improving their sustainability and performance (Salami et al. 2024).

In the construction industry, polymer concrete emerged as a solution to address the limitations of traditional concrete, particularly its susceptibility to cracking, low chemical resistance, and high permeability. The composition of polymer concrete plays a crucial role in determining its overall performance. Studies indicate that an optimal polymer content of 12–14% by weight enhances flexural strength (4 to 50 MPa) and increases compressive strength (40 to 150 MPa) (Ali and Ansari 2013). The integration of polymers into concrete mixtures gained significant attention in the 1950s, leading to the development of polymer-modified concrete, which offers improved flexibility, reduced permeability, and enhanced durability (Bulut and Şahin 2017; Waysal et al. 2023).

One of the primary advantages of polymer concrete is its ability to reduce material consumption while offering significantly enhanced performance compared to conventional cement concrete, as shown in Table 1. For example, polymer concrete exhibits much higher compressive strength (40–150 MPa) than traditional concrete (10–60 MPa), as well as superior flexural and tensile strengths. Additionally, it absorbs less water (0.5–3%) and demonstrates excellent chemical resistance, in contrast to the higher water absorption (4–10%) and poor-to-average chemical resistance of traditional concrete. These improved properties contribute to greater durability and making polymer concrete a more efficient and long-lasting construction material.

Table 1. Comparison of the properties of traditional and polymer concrete (Ali and Ansari 2013).

Properties	Traditional concrete	Polymer concrete
Compressive	10–60 MPa	40–150 MPa
Flexural strength	1.5–7 MPa	4–50 MPa
Tensile strength	0.6–3.0 MPa	4.0–20.0 MPa
Water absorption	4–10%	0.5–3%
Chemical resistance	Poor–Average	Very good–Excellent

In addition, polymer concrete demonstrates enhanced drainage properties, making it a preferred choice in applications requiring high permeability control. As illustrated in Fig. 1, these benefits stem from the material's unique pore structure, which influences water movement within the concrete matrix. In conventional concrete, refer Fig. 1(a), permeability is facilitated by interconnected voids between aggregate particles allowing water to flow freely. In contrast, polymer concrete exhibits a significantly lower permeability, as its polymer binder effectively fills or minimizes voids within the structure as shown in Fig. 1(b). As a result, water tends to accumulate on the surface rather than seeping through the material (Tabatabaeian et al. 2019). This reduced permeability plays a crucial role in preventing internal deterioration, minimizing chemical attacks, and enhancing resistance to moisture-related damage, thereby extending the lifespan and structural integrity of polymer concrete.

The composition of polymer concrete is another defining factor that differentiates it from traditional concrete types such as Portland cement concrete, polymer-modified concrete, and polymer-impregnated concrete. A critical component of polymer concrete is its aggregate system, which provides mechanical strength and influences the overall performance of the material. Aggregates are typically categorized into coarse aggregates (larger than 5 mm) and fine aggregates (smaller than 5 mm), both of which contribute to the material's stability and durability. In polymer concrete, aggregates and fillers generally account for 75–80% of the total volume, serving as a structural framework within the polymer matrix (Bedi et al. 2013). The choice of aggregate type, in addition to factors such as polymer selection, curing temperature, and dosage of key components, significantly affects the mechanical performance and long-term behavior of polymer concrete (Kumar 2016).

Although extensive research has been conducted on various types of polymers and their applications, there is still a lack of comprehensive reviews that link the history of polymer development to their structural advantages, limitations and evolving roles in the construction industry. Most of the existing literature tends to focus on isolated aspects such as material performance or environmental impact. Therefore, this review aims to bridge this

gap by synthesizing current knowledge on the historical evolution, mechanical benefits, chemical benefits, drawbacks and real world applications of polymers in construction. By offering an integrated perspective, this paper aims to support researchers, engineers, and policymakers in understanding the broader context and future potential of polymer-based materials in building and infrastructure development.

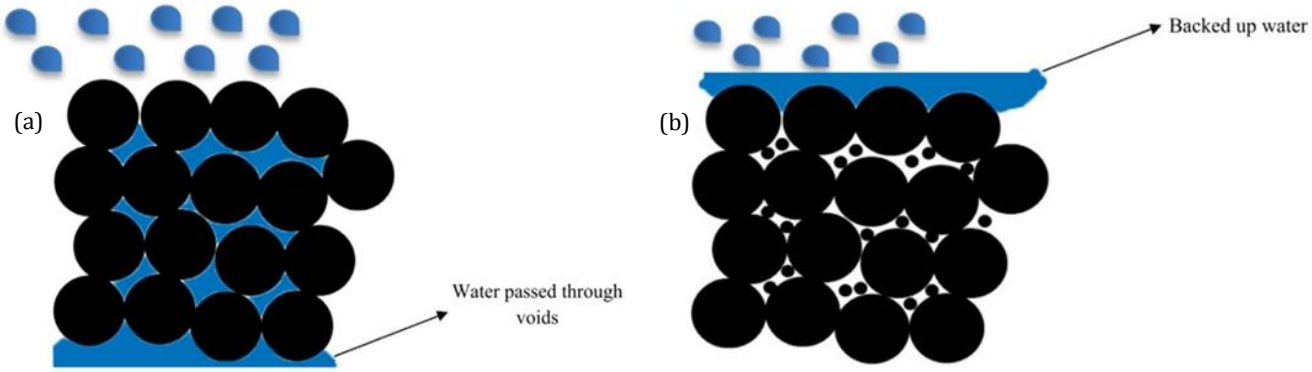

Fig. 1. The comparison of (a) conventional concrete and (b) polymer concrete (Tabatabaeian et al. 2019).

2. Development and Application of Polymer Concrete

The existence and production of polymers have been an integral part of scientific and industrial development for over a century. A significant milestone in polymer-based construction materials was achieved in 1923 when Cresson and Lefebure secured a patent for polymer-modified mortar, marking an early innovation in the field (Nodehi 2022). Since then, polymers have continued to gain attention for their versatility, durability, and diverse applications, making them an essential component in modern construction materials. Researchers play a critical role in optimizing the use, modification, and production of polymer-based materials to improve their performance, particularly for on-site construction applications.

The evolution of polymer composites in construction has been well-documented, with notable advancements shaping the industry over the decades. As highlighted in Nodehi (2022), the continuous refinement and development of polymer-based materials have resulted in substantial improvements in strength, durability, and sustainability. The progression of polymer concrete, from its early development stages to present applications, can be better understood through the timeline of key advancements (Fig. 2) and the historical evolution of composite materials (Table 2).

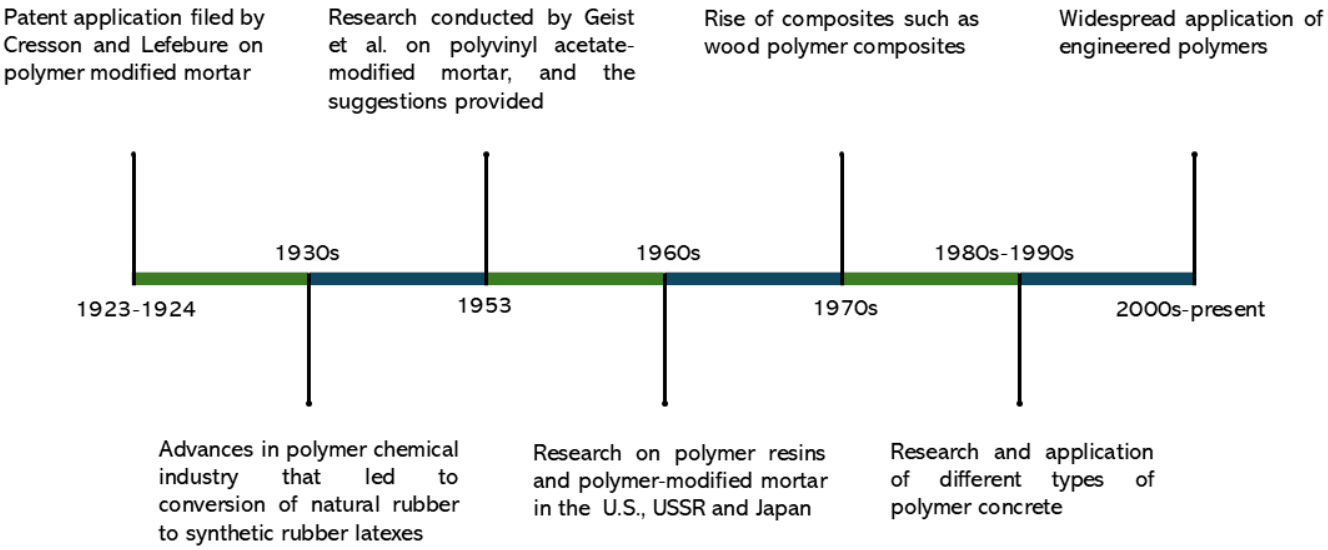

Fig. 2. Timeline of polymer concrete development (Nodehi 2022).

The historical development of polymer concrete reflects major advancements in both material science and practical applications. It started in the early 20th century. The milestone occurred in 1923–1924 when Cresson and Lefebure filed a patent for polymer-modified mortar. This innovation coincided with progress in polymer chemistry, particularly the shift from natural to synthetic rubber latexes, laying the groundwork for polymer use in cement-based materials. By the 1930s, the growing polymer industry enabled more structured ex-

perimentation in construction. In 1953, Geist et al. conducted a notable study on polyvinyl acetate-modified mortar. The highlight of the study is on how polymers could enhance bonding and flexibility in traditional systems. The 1960s saw expanded research in the U.S., USSR, and Japan on polymer resins and polymer-modified mortars, deepening the understanding of polymer cement interactions.

Table 2. Polymer composite history (Godara et al. 2021).

Time	Development of composite material
In 3400BCE	Man created plywood around 3400 BCE by adhering timber strips at different angles.
2181–2055BCE	Egyptians courted as early as 2181–2055 BCE by creating cartonnage out of layers of linen or papyrus wet in plaster.
Around 1500BCE	The earliest people used grass to strengthen pots, canoes, and dust bricks.
Around 1200 CE	The first composite bows were created by the Mongols using a mixture of bamboo, bone, horns, cattle tendons, silk, and wood that had been bound together with herbal pine resin.
1870s–1890s	New synthetic resins were able to change from a liquid to a solid state in a pass-connected molecular shape thanks to polymerization.
Early 1900s	Vinyl, polyester, polystyrene, and phenolic are examples of plastics that have evolved.
1930s	By introducing the first glass fibre, Owens Corning started the fibre giving a boost to polymer (FRP) business. Unsaturated polyester resins were patented in 1936.
1940s	The FRP company transitioned from research to practical manufacturing during World War II. A fully composite frame car had been created and tested by 1947.
Early 1950s	Large-scale filament winding, vacuum bag molding, and covered pultrusion are examples of sophisticated manufacturing techniques.
	The concept for the enormous rocket vehicles that drove space research in the 1960s and beyond was filament winding.
1960s	After a few years, carbon fibre composites were employed commercially after the original carbon fibre was patented in 1961.
	In the 1960s, the marine industry became the largest consumer of composite materials.
1970s–1980s	The automobile industry overtook the maritime industry as the biggest market for composite materials in the 1970s, and it continues to hold this position today.
1990–2000	By the middle of the 1990s, composites were widely used in production and manufacturing as a strong substitute for conventional materials. Every day, consumers come into contact with composite materials in the form of handles and exquisitely stained entryways at their homes. Composite materials were evaluated for high-energy and rigid applications during the development of the 787 Boeing Dreamliner in the mid-2000s.
Present day	The use of composite materials in the automobile, appliance, and consumer goods industries is continuously growing due to their growth. Furthermore, composites are only now beginning to find their way into nanotechnology. According to industry statistics, the global market for composite materials is expected to expand at a compound annual growth rate (CAGR) of 7.04% between 2016 and 2021, from USD 69.50 billion in 2015 to USD 105.26 billion by 2021.
The future	Governments, businesses, and academic institutions are becoming increasingly interested in the study of composite materials.
	This may put pressure on additional funding to help develop new fibres and resins. This might lead to more composite material uses in both new and existing sectors. Additionally, it is highly likely that environmentally friendly composite materials such as bio-based polymers and recycled plastics will become increasingly popular.

The 1970s began with improvement on hybrid materials such as wood polymer composites gained attention, signaling broader interest in combining polymers with conventional binders. A major shift occurred in the 1980s–1990s, when polymer concrete moved from experimental phases to structural applications, driven by its superior mechanical properties, durability, and resistance to corrosion particularly in harsh environments. Since the 2000s, the innovations in engineering polymers and advanced resins have further improved concrete performance, offering greater design flexibility and supporting sustainable construction practices. This evolution illustrates how developments in polymer chemistry have transformed concrete into a high-performance and multifunctional material suited for modern infrastructure needs.

Early examples of composite materials include plywood (circa 3400 BCE), cartonnage used by the Egyptians (2181–2055 BCE), and Mongolian composite bows (1200 CE), all of which incorporated natural fibers, resins, and adhesives to enhance structural performance. The emergence of synthetic resins in the late 19th century and early 20th century laid the foundation for the development of modern polymer composites, which eventually led to the widespread use of fiberglass-reinforced polymers (FRP) in the 1930s.

The mid-20th century marked a turning point, as polymer composites transitioned from laboratory research to commercial and industrial applications. During World War II, the development of lightweight, high-strength composites accelerated, leading to their use in military and aerospace applications. By the 1960s, the marine industry became the largest consumer of composite materials, followed by the automotive sector in the 1970s and 1980s. By the 1990s and early 2000s, polymer composites were widely used in production and manufacturing, serving as a strong substitute for conventional materials in various industries.

In the present day, the automotive, appliance, and consumer goods industries continue to drive the demand for composite materials. Moreover, nanotechnology advancements have further expanded their applications. According to industry statistics, the global market for composite materials has experienced consistent growth, with a compound annual growth rate (CAGR) of 7.04% from 2016 to 2021, increasing from USD 69.50 billion in 2015 to USD 105.26 billion in 2021 (Godara et al. 2021).

Looking to the future, governments, businesses, and academic institutions are expected to increase investments in polymer composite research, fostering the development of new fibers and resins. This could lead to broader applications across both existing and emerging industries. Additionally, the focus on environmentally friendly composite materials, such as bio-based polymers and recycled plastics, is expected to grow as sustainability concerns continue to shape industrial practices.

In Table 3, this structured timeline highlights the continuous improvements in polymer concrete reflecting both technological advancements and evolving industry demands. As polymer composites continue to evolve, their integration with emerging technologies, such as nanomaterials and artificial intelligence-driven material design, will further enhance their role in next-generation construction materials.

Table 3. Categorized polymer concrete evaluation process.

Properties	Unit	Polyester resin
Early development	1920s–1950s	• Initial research and experimentation with polymer-modified mortars. • Patent filing by Cresson and Lefebure (1923) for polymer-modified construction materials.
Emergence of polymer-modified concrete	1960s–1970s	• Increased commercial applications of fiberglass-reinforced polymers (FRP). • Use of polymer additives to improve concrete properties.
The advancements	1980s	• Integration of advanced fibre reinforcements such as carbon fibres and aramid (Kevlar). • Adoption of polymer concrete in high-performance infrastructure applications.
Eco-friendly developments	1990s–2000s	• Increased research into sustainable and recycled polymer composites. • Shift towards low-carbon and environmentally friendly polymer concrete formulations.
Modern innovations and trends	2010s–Present	• 3D printing technology enabling the fabrication of complex polymer concrete structures. • Development of bio-based and recyclable polymer binders for sustainable construction. • Expansion of polymer concrete applications in smart cities and green building practices.

2.1. Early development (1920s–1950s)

The early use of polymers in concrete can be traced back to the 1920s and 1930s, a period marked by significant advancements in the polymer chemical industry. During this time, natural rubber latexes were chemically modified to create synthetic rubber latexes and resin emulsions, which were subsequently used as polymeric modifiers in construction materials. These early innovations laid the foundation for further exploration in polymer-enhanced concrete (Nodehi 2022).

Although polymer-modified concrete gained traction in the 20th century, the origins of synthetic polymers date back even earlier. The first plastic material, derived from nitrocellulose, was developed by Parkes in 1862 and later refined by Hyatt in 1866 (Feldman 2008). However, a major breakthrough in polymer science occurred in 1907, when Belgian-American chemist Leo Baekeland invented Bakelite, the first fully synthetic plastic (Suyambulingam et al. 2025). This thermosetting polymer revolutionized materials science, leading to the rapid growth of plastics, rubbers, coatings, adhesives, and sealants as widely used materials in modern industries (Feldman 2008).

The advancement of polymer chemistry in the early 20th century led to the development of unsaturated polyester resin in 1930. Carleton Ellis discovered that the reaction between glycols and maleic anhydride could produce a polymer resin that, when catalyzed, hardened into an insoluble solid, paving the way for polymer-based composites (Ali and Ansari 2013). Around the same time, Baekeland's work on phenol-formaldehyde (PF) resins led to the synthesis of the first thermosetting polymer through a polycondensation process, which combined phenol and formaldehyde. Another early synthetic polymer, celluloid, was discovered by John Wesley Hyatt in 1869, marking the first commercially successful plastic made from cellulose, a natural polymer derived from plant fibers (Suyambulingam et al. 2025).

The success of phenol-formaldehyde resins prompted further research into other polycondensation-based polymers, leading to the development of urea-formaldehyde (UF) and melamine-formaldehyde (MF) resins. These amino resins, first identified by Tollens in 1884 and later

patented by John in 1918, became widely used in various industrial applications (Feldman 2008). Unlike phenoplasts, aminoplasts offer the advantage of being translucent or light-colored, making them suitable for diverse engineering applications. These early advancements in synthetic polymers paved the way for the creation of polymer composites, which later became integral to polymer-modified concrete (Suyambulingam et al. 2025).

The development of polymer-modified concrete was further facilitated by research into polyvinyl acetate (PVA) as a polymer modifier (Nodehi 2022). However, the discovery of vinyl chloride (VC) dates back even earlier, to 1835, when Liebig and Regnault first identified the compound (Feldman 2008). Its potential for polymerization was not fully understood until Baumann's 1878 study, which revealed that sunlight exposure could trigger VC polymerization, forming a white solid residue. This discovery laid the groundwork for polyvinyl chloride (PVC) production. Further advancements in the early 20th century led to the patenting of flexible PVC films by Ostramislenski in 1926 (Feldman 2008). Subsequent research showed that heating PVC with high-boiling-point liquids transformed it into a rubber-like material, leading to the development of phthalate-based plasticizers. By the 1930s, these materials were widely used in elastomeric applications, and large-scale commercial production of PVC began in 1935 (Feldman 2008).

World War II significantly accelerated the development and application of polymer composites, particularly due to material shortages and the urgent need for high-performance alternatives to rubber and metals (Suyambulingam et al. 2025). The war effort prompted innovations in synthetic rubber, electrical insulation, and high-strength composites, which later translated into civilian applications (Feldman 2008). One of the most crucial polymer advancements during the war was the development of epoxy resins (EP). Schlack, the inventor of nylon 6, synthesized the first epoxy resins in 1934 (Feldman 2008). These thermosetting polymers, derived from petroleum, exhibited outstanding mechanical, chemical, and adhesive properties. When reinforced with fibers, epoxy-based composites display remarkable strength, durability, and resistance to harsh environments, making them ideal for aerospace, automotive, and infrastructure applications (Suyambulingam et al. 2025).

By the end of World War II, polymer-based products had begun transitioning into civilian industries, marking the expansion of polymer composites into mainstream manufacturing. Developments in material science and production techniques enabled composites to be produced at lower costs and on larger scales, leading to their widespread use in consumer goods, transportation, and construction. The construction industry, in particular, recognized the potential of polymer-based materials, incorporating them into concrete formulations to improve performance, durability, and environmental resistance (Ali and Ansari 2013). By 1955, the building and construction sector had become the largest consumer of plastics, according to the Association of Plastics Manufacturers in Europe (APME). Today, the construction industry remains one of the top three global consumers of polymer-based materials, underscoring the growing reliance on polymer composites in structural applications (Ali and Ansari 2013).

2.2. Polymer-modified concrete (1960s–1970s)

Around The 1960s and 1970s marked a transformative period in the development of polymer-modified concrete (PMC), characterized by advancements in carbon fiber technology, thermosetting resins, and industry recognition. These innovations significantly improved the mechanical properties, durability, and performance of polymer concrete, leading to its widespread adoption in various engineering applications. The modern development of carbon fibers can be traced back to 1942, although their origins date as far back as 1879, when they were initially used as light bulb filaments (Feldman 2008). Derived from cellulosic precursors, the first commercially produced carbon filament was designed for incandescent lamp filaments. However, further research in 1959 and 1961 led to the development of high-strength and high-modulus carbon fibers from rayon and polyacrylonitrile (PAN), marking a breakthrough in high-performance reinforcement materials (Feldman 2008). Carbon fibers exhibit tensile strengths ranging from 3000 to 7000 MPa, significantly outperforming traditional reinforcement materials such as glass fibers and steel (Godara et al. 2021). Due to their remarkable strength-to-weight ratio, stiffness, and thermal stability, carbon fiber-reinforced composites became widely used in aircraft structures, including doors, wings, fuselage sections, and tail surfaces.

The introduction of thermosetting resins, such as epoxy, polyester, and phenolic resins, further enhanced the performance of polymer concrete. These resins improve adhesion between reinforcing fibers, allowing for the development of high-performance composite materials tailored for specialized applications (Suyambulingam et al. 2025). Glass fibers, another commonly used reinforcement material, typically exhibit tensile strengths between 2000 and 3500 MPa, making them suitable for lightweight yet durable structural components. The combination of carbon and glass fiber reinforcements with thermosetting resins enabled the production of advanced polymer composites with superior mechanical, chemical, and thermal resistance.

A significant milestone in polymer concrete research was the formal recognition of its importance by the American Concrete Institute (ACI) in 1971, with the establishment of ACI Committee 548 dedicated to polymer-modified concrete (Bedi et al. 2013). This institutional recognition accelerated research efforts, leading to the systematic study, standardization, and application of polymer-based concrete formulations. During this period, polymer concrete composites gained traction due to their versatile properties and ability to meet the increasing demand for high-strength, high-performance construction materials. Recent advancements have expanded the scope of polymer concrete composites, particularly through the use of industrial and agricultural waste in formulations, aligning with sustainability goals and environmentally friendly construction practices (Alhazmi et al. 2021).

2.3. Advancement in the 1980s

The 1980s marked a significant period of innovation in polymer composites, driven by the development of advanced fiber reinforcements such as aramid (Kevlar) and high-performance carbon fibers (Suyambulingam et al. 2025). These fibers offer exceptional strength-to-weight ratios, making them highly suitable for use in polymer-reinforced composites. Their lightweight nature, durability, and superior corrosion resistance enabled their application in civil engineering projects, including buildings, bridges, and infrastructure (Suyambulingam et al. 2025). The incorporation of advanced fiber reinforcements significantly enhanced the mechanical properties of polymer composites, making them adaptable for various applications. Several types of fibers were used during this period, including natural fibers (such as hemp and flax), glass fibers, carbon fibers, and aramid fibers. While synthetic fibers such as carbon and aramid fibers provided superior strength, stiffness, and fatigue resistance, natural fibers emerged as a cost-effective and environmentally friendly alternative in certain applications. The ability of these advanced fibers to withstand extreme conditions makes them suitable for high-performance applications in industries such as aerospace, automotive, and sporting goods.

The use of polymer concrete can be traced back to 1958 in the United States, where it was first utilized for building cladding applications (Fowler 1999). Unlike conventional concrete, polymer concrete eliminates the need for Portland cement and water, relying instead on aggregates bound by a polymer binder. As urbanization and large-scale infrastructure projects accelerated worldwide, the demand for cement-based materials surged, creating economic and environmental challenges, as illustrated in Fig. 3.

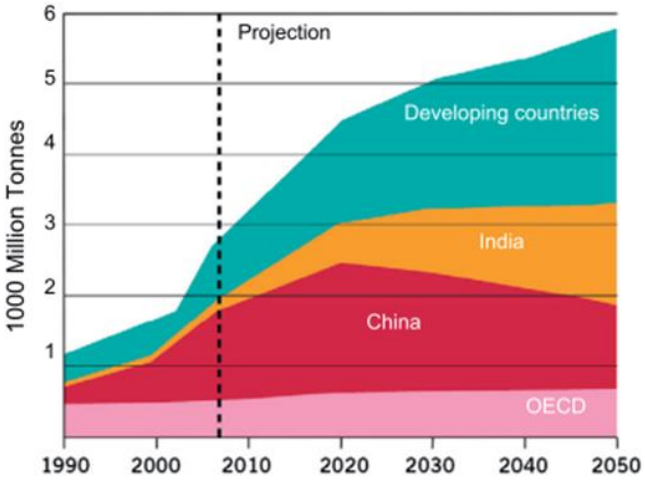

Fig. 3. The demand for cement varies by region and country (Fowler 1999).

The rising global cement demand from 1990 to 2050 underscores the urgent need for sustainable alternatives. Traditional cement production is associated with high energy consumption and CO_2 emissions, driving researchers to explore polymer concrete as a potentially eco-friendly substitute. Compared to Ordinary Portland Cement (OPC)-based materials, polymer-based mortar and concrete offer enhanced durability, reduced permeability, and resistance to environmental degradation (Nodehi 2022).

Following 1980, the development of high-performance polymers led to new polymer formulations capable of competing with traditional materials. Notable advancements included Metallocene polyolefins, Polyamide 4-6 (1987), Syndiotactic polystyrene (PS) (1989), Polyphthalamide (1991), Styrene–ethylene copolymer and Syndiotactic polypropylene (PP) (1992) (Feldman 2008). These innovations contributed to enhanced material properties, broadening the applications of polymer composites in construction, transportation, and high-performance engineering fields. The continued evolution of polymer concrete in the 1980s demonstrated its potential as a durable and sustainable alternative to traditional cement-based materials, paving the way for further advancements in the 1990s and beyond.

2.4. Eco-friendly developments (present)

Since the 2010s, advancements in polymer research and development have progressed significantly, with a strong emphasis on enhancing polymer properties, expanding their applications, and improving sustainability. Researchers and industries worldwide are working to overcome the limitations of conventional polymers, particularly in composite materials, while simultaneously minimizing their environmental impact (Oladele et al. 2023). These efforts aim to tackle contemporary challenges such as environmental sustainability, material performance, and resource efficiency. With continued progress in technology and research, new opportunities have emerged to improve the durability, recyclability, and overall eco-friendliness of polymer composites (Suyambulingam et al. 2025). However, despite these advancements, the limited understanding of these materials and their associated technologies has hindered their widespread adoption in many industries (Oladele et al. 2023).

In recent years, research and technological improvements have positioned polymer-based materials as a viable alternative to traditional construction materials, progressively replacing conventional concrete and cement-based composites. A key area of research focuses on waste management strategies for reducing plastic waste and its environmental impact. As illustrated in Fig. 4, a typical plastic waste dump highlights the growing environmental concerns caused by improper disposal of non-biodegradable materials. The image illustrates how plastic waste accumulates in the natural environment, leading to soil and water pollution, endangering wildlife and contributing to visual pollution. This type of unmanaged plastic pollution highlights the need to develop sustainable waste management strategies, such as recycling plastics into value-added building materials such as polymer concrete. Salami et al. (2024) had highlighted the feasibility of using waste plastic in concrete production, citing benefits such as localized material use, reduced greenhouse gas (GHG) emissions, and improved durabil-

ity. One of the primary concerns in traditional concrete production is the high carbon footprint of cement, which contributes significantly to global CO_2 emissions. As cement demand continues to rise, the addition of polymers to concrete presents both challenges and opportunities. While the incorporation of polymer materials can reduce dependence on cement, thus lowering emissions, certain polymer production processes may still contribute to GHG emissions (Salami et al. 2024).

To address these challenges, geopolymer concrete has emerged as a sustainable alternative, offering enhanced strength characteristics while maintaining a low carbon footprint and reduced consumption of natural resources (Alhazmi et al. 2021). Unlike traditional concrete, polymer concrete replaces cement hydrate binders with liquid resins or polymer binders, making it a more environmentally friendly construction material (Rochman et al. 2024).

Fig. 4. Plastic waste dumping site (Koirala et al. 2025).

The introduction of polymer composites into 3D printing has revolutionized manufacturing and construction processes, providing key benefits such as increased design flexibility, reduced material waste and production of lightweight yet high-strength components. Advancements in additive manufacturing (AM), commonly known as 3D printing, have played a pivotal role in expanding the applications of polymer composites. This technology enables the fabrication of complex composite structures with customized geometries and mechanical properties, offering unprecedented precision and material efficiency (Suyambulingam et al. 2025). The use of polymer composites in 3D printing gained momentum in the early 2010s, evolving from traditional polymer-based methods such as fused deposition modeling (FDM) and stereolithography (SLA) to more advanced techniques. A major breakthrough occurred in 2014 with the launch of the Mark One 3D printer by Markforged, which introduced continuous fiber reinforcement technology. Unlike conventional polymer-based 3D-printed materials, this innovation enabled the production of structural components with strength and durability comparable to conventional composites. Furthermore, the advantages of 3D printing go beyond its influence on the global market, offering substantial potential for environmental protection and supporting the growth of a globally sustainable economy (Alami et al. 2023).

3. Applications of Thermosetting Resins in Polymer Concrete

Polymer concrete (PC) is a high-performance construction material that has been in commercial use since the early 1960s (Rebeiz 1996). It is produced by adding small amounts of initiators and promoters to the resin, which triggers the curing or hardening process as shown in Fig. 5. The production process of polymer concrete using recycled PET. This process involves mixing a liquid component (unsaturated polyester resin), initiator, promoter, and solid aggregates, followed by curing to form the final material. This method highlights how recycled plastics can be used in sustainable construction. Polymer concrete was driven by the need to address the inherent limitations of traditional Portland cement concrete, which often suffered from issues such as cracking, high permeability, and low resistance to chemical exposure. Unlike conventional concrete, polymer concrete incorporates polymeric resins as a binder, which significantly enhances its mechanical strength, durability, and resistance to environmental degradation. The uses of polymer concrete largely depend on the physical and chemical properties of both the aggregates and the resin, with the resin's effectiveness also being influenced by how long it has been stored after production (Martínez-López et al. 2022).

3.1. Polyester resin

Polyester is a widely used class of polymers containing ester functional groups in their main chain, commonly found in coatings, textiles, and packaging. Due to its superior mechanical and chemical properties, affordability compared to epoxy resin, and widespread commercial availability, polyester resin is often the preferred choice for polymer concrete construction (Bulut and Şahin 2017). Polyester resins are synthesized through polycondensation reactions involving dicarboxylic acids and dihydroxy alcohols, forming durable thermosetting polymers (Tabatabaeian et al. 2019).

A study by Aravecchia et al. (2023) examined the use of recycled polyester (PE) resin powder as shown in Fig. 6(a), specifically identified as "PE/P/M BLACK RAL 9005," a waste product from the coating industry supplied by INVER S.p.A. PE resin is widely used for its excellent resistance to weathering and UV radiation. It has a density of 1380 kg/m^3, a fine particle size of about 3.5 µm and is hydrophilic, as shown by its contact angle of approximately 74.4°, shown in Fig. 6(b). Additionally, the chemical composition of PE resin was analyzed using X-ray Photoelectron Spectroscopy (XPS) and Energy-Dispersive X-Ray Spectroscopy (EDS), revealing that carbon, oxygen, and calcium are its primary constituents. These findings suggest that PE resin could chemically in-

teract with Ordinary Portland Cement (OPC) rather than merely acting as an inert aggregate, indicating its potential as a reactive component in polymer concrete formulations (Aravecchia et al. 2023).

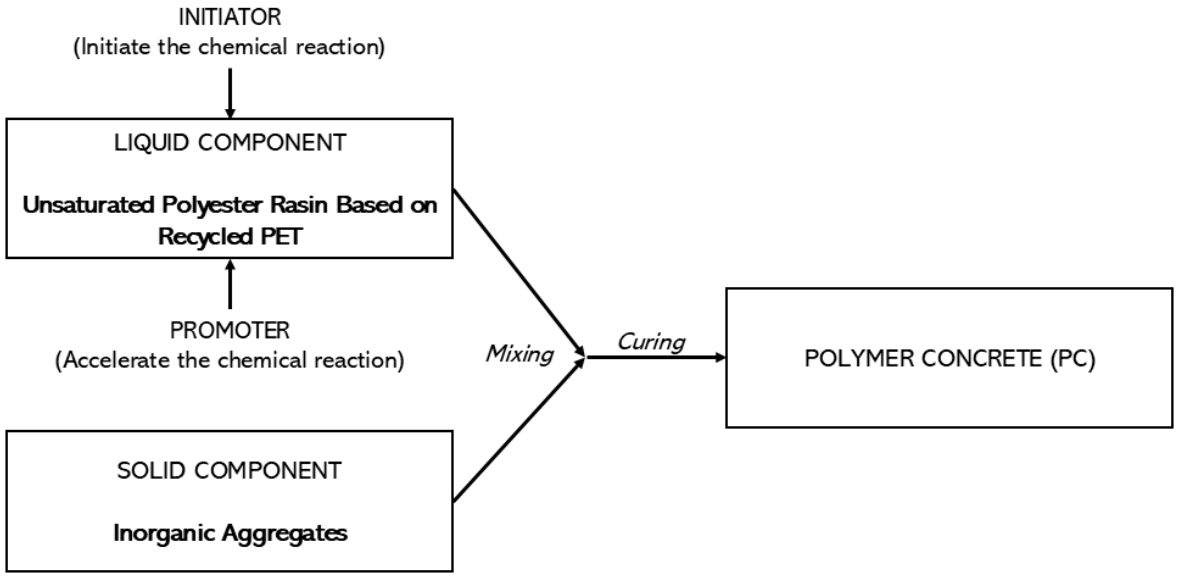

Fig. 5. The production of polymer concrete (Rebeiz 1996).

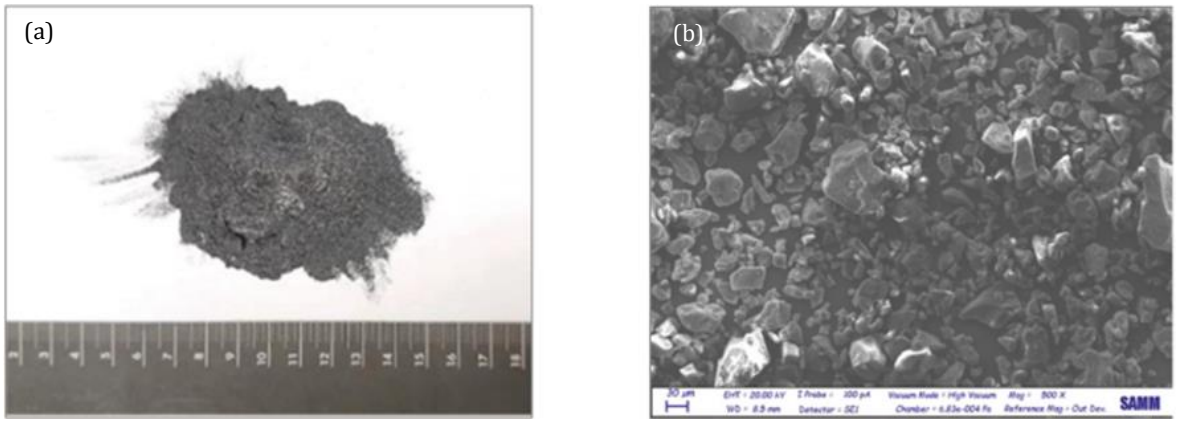

Fig. 6. (a) Polyester resin and (b) SEM image (Aravecchia et al. 2023).

Polyester resins are extensively used in gelcoat applications, with more than 85% of gelcoats incorporating unsaturated polyester (UP) resins. Research by (Akarken et al. 2025) explored formulations containing at least 42% unsaturated polyester resin, significantly exceeding conventional levels. While this higher resin content enhanced certain properties, it also complicated the modification process, potentially affecting durability, performance, and compatibility with other materials in gelcoat applications.

Advances in bio-based unsaturated polyester (UP) resins have also demonstrated promising results. A study by (Rubeš et al. 2024) found that bio-based UP resins exhibit mechanical properties comparable to traditional styrene-based formulations, including high flexural strength and compressive yield points. These findings highlight the potential of bio-based polyester resins as sustainable alternatives for applications requiring high durability and performance. Unsaturated polyester resins offer several notable advantages, including high chemical and mechanical resistance, robust weather resistance, cost-effectiveness and ease of handling and processing.

Additionally, unsaturated polyester resins can be easily reinforced with fibers, allowing for the development of lightweight and high-strength composite materials (Batista et al. 2021). Khallouqi et al. (2024) emphasized that polyester resins possess unique characteristics, such as insolubility, water resistance, optical transparency, and a density similar to human soft tissue (1.10–1.19 g/cm^3). These attributes, along with their moldability and wide availability, make polyester resins highly adaptable for various industrial applications.

Despite their widespread use, unsaturated polyester (UP) resins pose significant environmental challenges. At the end of their life cycle, these resins contribute to substantial resource waste and environmental degradation (An et al. 2024). One of the major environmental concerns is the high volatile organic compound (VOC) content in polyester-based insulating coatings, which typically contain 50–70% VOCs derived from organic

solvents (Choe et al. 2023). These emissions contribute to air pollution and ecological harm, necessitating the development of low-VOC or VOC-free alternatives.

Additionally, polymer derivatives of polyester such as polyethylene terephthalate (PET) offer strong mechanical properties and economic advantages but lack biodegradability. The accumulation of PET waste has become a pressing environmental issue, underscoring the urgent need for more sustainable material alternatives. Researchers are now exploring bio-based polyesters and recycling strategies to minimize environmental impact and promote circular economy principles in polymer resin applications.

3.2. Epoxy resin

Epoxy resin is a widely used thermosetting polymer, recognized for its exceptional mechanical properties and versatility in industries such as transportation, aerospace, construction, and packaging (Zhang et al. 2024). Its key advantages include high corrosion resistance, superior electrical insulation, excellent chemical stability, and strong adhesion, making it a preferred material for structural reinforcement and protective coatings.

Epoxy resins are synthesized through a coupling reaction between epichlorohydrin and compounds containing at least two active hydrogen atoms (Kumar 2016). During synthesis, dehydrohalogenation occurs in an intermediate stage, resulting in the formation of epoxy groups that define the resin's properties (Fig. 7). Compared to other thermosetting polymers, epoxy resins exhibit superior strength, resilience, and low shrinkage, making them ideal for offshore, coastal, and high-performance construction applications (Verma et al. 2020). Their resistance to harsh environments enhances the longevity of structures, particularly in marine and industrial settings (Fame et al. 2024).

Additionally, epoxy systems are extensively used in protective coatings due to their strong adhesion to various surfaces, along with excellent thermal, mechanical, and anti-corrosive properties. One of the major advantages of epoxy resins is their recyclability, making them a more sustainable option compared to conventional thermosetting materials (Tsyklinskaya et al. 2024).

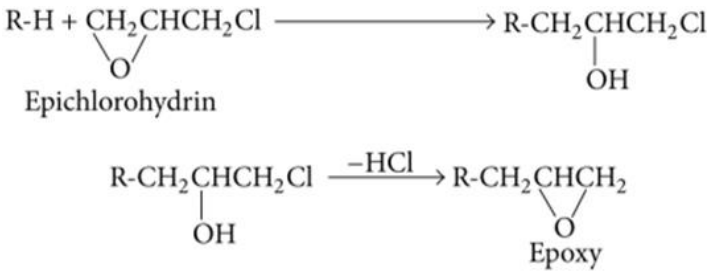

Fig. 7. Epoxy preparation (Kumar 2016).

The combination of epoxy and concrete significantly enhances the mechanical and chemical performance of the material. When used as a binder, sealer, or coating, epoxy improves concrete durability, impermeability, and structural integrity. Compared to polyester concrete, epoxy-modified concrete demonstrates superior performance; however, the addition of microfillers can elevate polyester concrete's properties to a comparable level (Kumar 2016).

A study by Fei et al. (2024) examined the mechanical properties of epoxy polymer concrete, using specialized equipment such as the YAW 4206 compression tester and Instron 3365 universal testing machine. The research assessed compressive, flexural, interfacial flexural, and tensile strength at curing intervals of 3, 7, and 28 days. Results demonstrated that epoxy-based concrete exhibited superior mechanical strength and enhanced corrosion resistance compared to traditional epoxy concrete formulations. However, to improve process efficiency and industrial applicability, reducing the curing time of epoxy resins remains a critical area of research (Kumar 2016).

As summarized in Verma et al. (2020), the studies by Wang et al. (1999) and Wang et al. (2011) reported the mechanical and physical properties of polyester and epoxy resins, highlighting their respective strengths and limitations, as shown in Table 4. Epoxy resins generally offer higher tensile and flexural strength, lower shrinkage, and improved heat resistance, making it ideal for high-performance applications. These qualities make it well-suited for high-performance and demanding applications. On the other hand, polyester resin provides higher compressive strength and greater surface hardness, making it more suitable for structural applications that involve compressive forces. Both resins have their own strengths depending on how and where they are used.

3.3. Polyethylene terephthalate (PET)

Polyethylene terephthalate (PET) is one of the most widely used plastics globally in production (Fig. 8) of beverage containers and synthetic fibers. In fact, PET accounts for over 80% of all chemical fiber production worldwide (Waysal et al. 2023). As summarized in Table 5 by Aravecchia et al. (2023), primary studies by Azhdarpour et al. (2016), and Silva et al. (2005) highlight that the extensive use of PET has made it the most common form of plastic waste. This widespread disposal underscores the urgency of developing sustainable strategies to repurpose PET waste, particularly in the construction sector. An innovative approach is to incorporate PET into concrete mixtures, which not only helps reduce environmental pollution but also enhances the performance of the material.

Table 4. Typical thermosetting resins and their mechanical and physical characteristics (Verma et al. 2020).

Properties	Unit	Polyester resin	Epoxy resin
Elongation at break	%	5	5
Heat distortion temperature	°C	60–100	120
Tensile strength	MPa	42–71	~85
Density.	g/cm³	1.10–1.46	1.11–1.23
Compressive strength	MPa	92–190	~11
Tensile elastic modulus	GPa	2.1–4.5	~3.2
Flexural strength	MPa	60–120	~130
Linear expansion coefficient	10^{-6}/°C	80–100	60
Water absorption (24h)	%	0.15–0.60	0.14
Rockwell hardness (6.35 mm, 100 kg)	–	115	100
Shrinkage rate	%	4–6	1–2

Table 5. Properties, primary production and waste generation of the most widespread polymers (Aravecchia et al. 2023)

Polymer	Id	Recycled	Category	ρ (kg/m³)	f_t (MPa)	E (GPa)	Production (million tons)	Generated waste (million tons)
Polyvinyl chloride	PVC	Occasionally	Thermoplastic	1300–1580	50–60	2.7–3.0	38	15
Polyurethane	PUR	No	Thermosetting	–	–	–	27	16
Polystyrene	PS	No	Thermoplastic	1040–1050	30–55	3.1–3.3	25	17
Polypropylene	PP	Occasionally	Thermoplastic	900–910	25–40	1.3–1.8	68	55
Polyethylene terephthalate	PET	Yes	Thermoplastic	1270–1390	55–80	2.1–3.1	33	32
Low density polyethylene	LDPE	No	Thermoplastic	910–930	8–31	0.2	64	57
High density polyethylene	HDPE	Yes	Thermoplastic	950–960	22–31	1.08	52	40
Polyphtalamide	PP&A	Occasionally	Thermoplastic	–	–	–	59	42

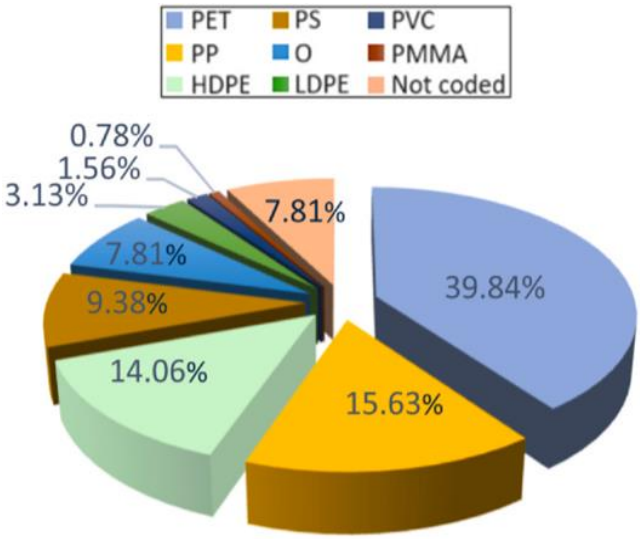

Fig. 8. Common usage of plastic packing materials (Mehdar 2024).

PET is a unique chemical structure were synthesized from terephthalic acid (H_2BDC) and ethylene glycol (EG) which results in a durable and chemically stable polymer, as shown in Fig. 9 (Wang et al. 2024). Its molecular formula, $(C_{10}H_8O_4)_n$, indicates a repeating ester unit that contributes to its strong physical and chemical properties (Fig. 10).

These characteristics include excellent thermal stability, high flexibility, strong corrosion resistance, wear resistance, and chemical inertness. Additionally, PET is lightweight, retains gases effectively, and can withstand high temperatures, making it not only ideal for packaging applications but also suitable for use in construction materials (Waysal et al. 2023). The integration of PET into concrete has demonstrated encouraging results. For instance, (Wattanavichien and Iwanami 2024) observed that replacing 20% of coarse aggregate with PET improved drying shrinkage and abrasion resistance. Remarkably, the PET-modified concrete recorded a compressive strength of 80 MPa, highlighting its potential for

high-performance structural applications. PET-enhanced concrete also shows high resistance to aggressive chemicals such as sodium chloride and sodium hydroxide, contributing to its long-term durability (Wattanavichien and Iwanami 2024).

Beyond mechanical improvements, PET offers environmental advantages to the world. Research by Pacheco-Torgal et al. (2012) revealed that using PET waste as a partial aggregate substitute not only enhances concrete workability but also reduces reliance on natural aggregates and mitigates landfill use. Furthermore, PET waste can be converted into carbon nanomaterials, presenting an innovative route for both plastic waste reduction and carbon sequestration (Soni et al. 2024). In broader terms, other commonly used plastics in construction and packaging include Polyvinyl Chloride (PVC), High-Density Polyethylene (HDPE), Polypropylene (PP), Low-Density Polyethylene (LDPE), Polystyrene (PS), and Polymethyl Methacrylate (PMMA) (Mehdar 2024). However, PET stands out due to its balance of sustainability, mechanical strength, and chemical stability.

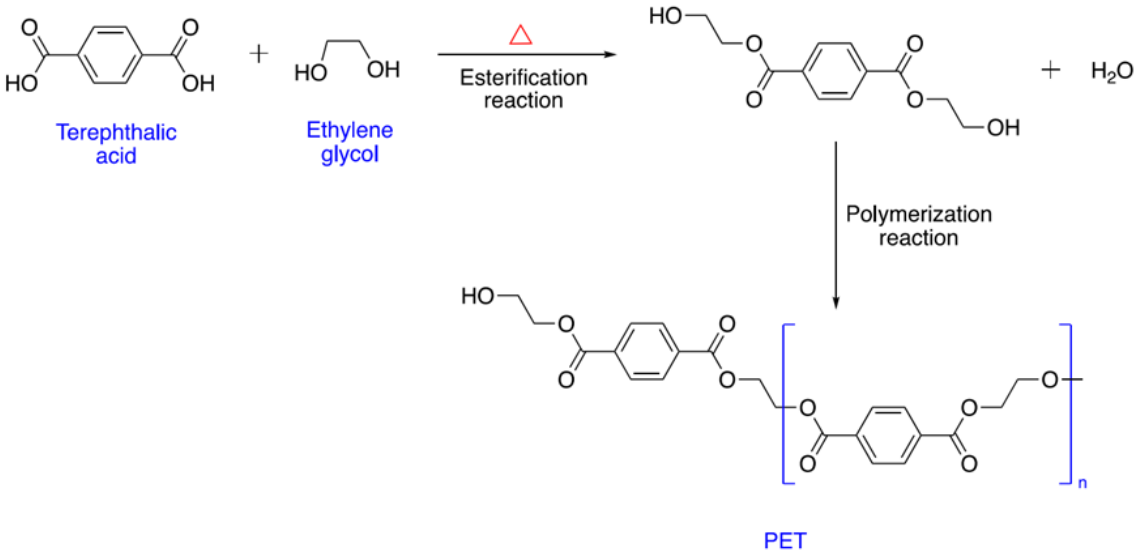

Fig. 9. Result of polymerization of terephthalic acid (H_2BDC) and ethylene glycol (EG) in the formation of the polymer PET plastic (Surucu 2025).

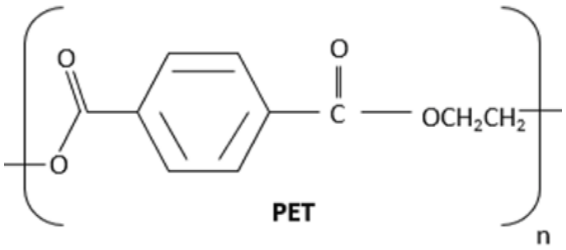

Fig. 10. Molecular structure of polyethylene terephthalate chemical formula: $(C_{10}H_8O_4)_n$ (Surucu 2025).

With global cement demand on the rise, researchers are increasingly turning to plastic waste as an eco-friendly, cost-effective, and sustainable alternative to traditional concrete materials (Z. Wang et al. 2024). One promising approach involves converting PET waste into composite materials for use in construction and road infrastructure projects (Heidari-Rarani et al. 2023). According to (Pacheco-Torgal et al. 2012), using PET waste as aggregate not only lessens dependence on natural resources and reduces landfill usage but also improves concrete workability, making it easier to mix and apply on-site. Additionally, concrete enhanced with PET demonstrates strong resistance to environmental chemicals like sodium chloride and sodium hydroxide by increasing its durability and lifespan in harsh conditions (Wattanavichien and Iwanami 2024). Together, these insights highlight PET's potential as a versatile additive that addresses plastic waste while promoting more resilient and sustainable construction practices.

However, in recent years PET is one of the widely used polymers in 3D printing (Alami et al. 2023). It is particularly valued for its dimensional stability and durability, making it suitable for functional parts and prototypes. PET, along with its modified form polyethylene terephthalate glycol (PETG) is commonly used in sectors such as automotive, electronics, and healthcare, where strength and reliability are essential. Its widespread availability and cost-effectiveness also contribute to its popularity in additive manufacturing.

3.4. Vinyl ester

Among thermosetting polymers, certain materials stand out due to their exceptional performance characteristics. Epoxy and vinyl ester (VE) resins are particularly notable for their excellent adhesion, mechanical strength, chemical resistance, and thermal stability (Fame et al. 2024). Once catalyzed, these resins undergo an irreversible curing process, meaning they cannot return to their original state, unlike thermoplastic materials that rely on temperature-based curing (Rochman et al. 2024).

Compared to epoxy resins, vinyl ester resins are advanced thermosetting polymers that exhibit superior

chemical resistance, mechanical strength, and durability, making them a promising choice for composite materials (Rayati et al. 2025). Vinyl ester is synthesized by combining styrene and a condensation product of methacrylic acid with epoxy resin, and its curing process is facilitated through the addition of catalysts (Thomason and Xypolias 2024). One of the key advantages of vinyl ester resins is their low viscosity, which enhances workability in polymer concrete applications, making them easier to handle and process (Rochman et al. 2024).

To improve performance, cost efficiency, and sustainability, researchers have developed modified vinyl ester formulations. A study by Fei et al. (2024) explored modifications such as the incorporation of soybean oil-based resins and carbon sphere (CS) fillers, leading to improved mechanical properties and environmental benefits. Additionally, Venu et al. (2024) demonstrated that adding cenosphere particles of varying sizes further enhanced the mechanical strength and thermal stability of vinyl ester resins.

Vinyl ester resins are composed of bisphenol-A diglycidyl dimethacrylate epoxy and styrene. The general chemical structure of vinyl ester methacrylate and the atomistic models for n = 1 (VE1) and n = 2 (VE2) are shown in Fig. 11 (a)-(b)-(c)-(d)-(e), along with the molecular structure of styrene. These structural properties contribute to the high-performance characteristics of vinyl ester resins, particularly in composite applications.

The physical and mechanical properties of vinyl ester resin have been widely studied, particularly in its application for glass fiber-reinforced polymer (GFRP) bars. Benmokrane et al. (2017) conducted an evaluation comparing vinyl ester, isophthalic polyester, and epoxy resins, assessing their flexibility, mechanical strength, and durability. Table 6 summarizes the typical properties of these thermosetting resin systems. When compared to other resins, vinyl ester resin used in GFRP bars demonstrates moderate resistance to temperature-induced flexibility. However, it is not as strong as epoxy resin, which offers superior mechanical performance and rigidity. Despite this, vinyl ester's chemical resistance and cost-effectiveness make it a viable alternative in specific applications where corrosion resistance and durability are critical.

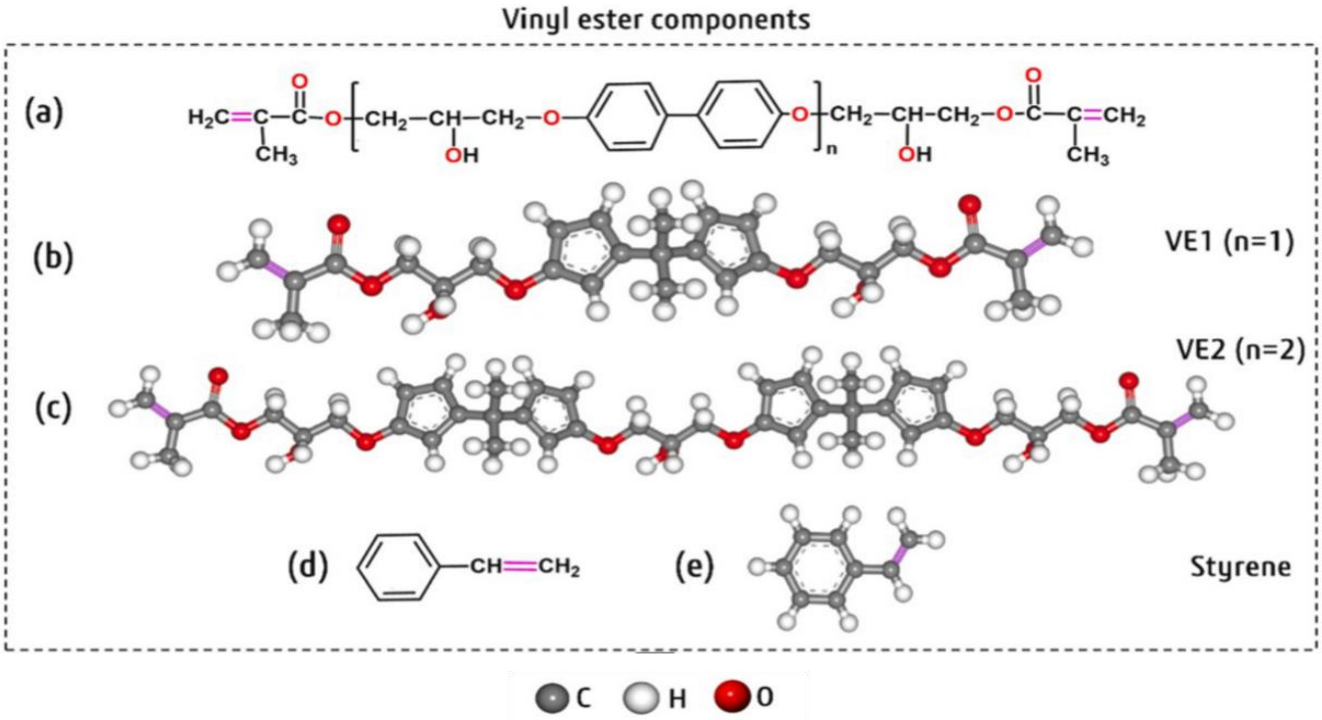

Fig. 11. Vinyl ester crosslinking steps: (a) Bisphenol-A diglycidyl dimethacrylate (VE) general chemical formula; (b) VE1 atomistic model; (c) VE2 atomistic model; (d) Styrene chemical formula; (e) Styrene atomistic mode (Fame et al. 2024).

Table 6. Typical characteristics of thermosetting resins (Benmokrane et al. 2017).

Properties	Unit	Polyester	Vinyl ester	Epoxy
Glass transition temperature (Tg)	℃	100	110	120
Tensile modulus	GPa	4.0	3.5	3.0
Tensile strength	MPa	65	82	90
Elongation	%	2/5	6.0	8.0
Property	Unit	Polyester	Vinyl ester	Epoxy

4. Comparison of Mechanical Properties of Polymers

The mechanical properties of polymer concrete vary significantly based on its preparation conditions. There were several factors influence the data including binder content, aggregate size distribution, micro-filler type and amount, and curing conditions, play a crucial role in determining overall performance (Bedi et al. 2013). These factors directly impact key mechanical properties such as compressive strength, flexural strength, and tensile strength, as summarized in. Table 7 presents a comparative analysis of four key polymer materials polyester resin, epoxy, polyethylene terephthalate (PET), and vinyl ester by evaluating their compressive strength, flexural strength, and tensile strength based on data from multiple studies. The variations in these properties highlight the differences in mechanical performance, durability, and suitability for specific construction applications.

Table 7. Compressive strength, flexural strength and tensile strength comparison of polymer materials.

Polymer	Compressive strength (MPa)	Flexural strength (MPa)	Tensile strength (MPa)	Publication
Polyester resin	–	–	40–70	(Nodehi 2022)
	–	–	65	(Benmokrane et al. 2017)
	–	–	55	(Bulut and Şahin 2017)
	120	–	70	(Tabatabaeian et al. 2019)
	92–190	60–120	42–71	(Verma et al. 2020)
	89	110	68	(Kumar 2016)
	–	120	64	(van Zyl and Kruger 2025)
Epoxy	–	–	60–125	(Nodehi 2022)
	–	–	90	(Benmokrane et al. 2017)
	70	–	36	(Tabatabaeian et al. 2019)
	11	130	85	(Verma et al. 2020)
	22–95	–	–	(Gulabbhai et al. 2025)
	51–66	22.5	7.67–12.1	(Kumar 2016)
	–	40–80	–	(Luo et al. 2024)
	59–78	–	36–47	(Byron et al. 2021)
Polyethylene terephthalate (PET)	–	–	47	(Nodehi 2022)
	80	–	–	(Wattanavichien and Iwanami 2024)
	26	–	–	(Safinia and Alkalbani 2016)
	40–50	6–10	–	(Grigoriadis et al. 2023)
	30.3	3.44	–	(Umasabor and Daniel 2020)
	–	–	140	(Sarwar et al. 2024)
	29–42	5.25–6.6	98.8	(Yılmaz and Nayır 2024)
Vinyl ester	–	–	70–84	(Nodehi 2022)
	–	–	82	(Benmokrane et al. 2017)
	89	–	–	(Gulabbhai et al. 2025)
	70	64.62	80	(Venu et al. 2024)
	–	115	15–95	(van Zyl and Kruger 2025)
	41–104	144	82	(Rochman et al. 2024)

Note: '–' indicates that data were not provided in the publication.

Polyester resin exhibits a wide range of compressive strength values, with studies reporting values between 92 MPa and 190 MPa (Verma et al. 2020). This range suggests that different formulations and modifications can significantly impact polyester resin's compressive performance. However, it generally has moderate tensile strength, ranging from 40 MPa to 70 MPa (Nodehi 2022). Polyester resin's flexural strength varies significantly, with reports of 60 MPa to 120 MPa (Verma et al. 2020). Tensile strength has received more research attention in polyester resin likely because it is critical for understanding how well polymer composites resist cracking and stretching. In contrast, there is relatively less research on compressive and flexural strength. This imbalance suggests that while polyester resins generally offer a well-rounded mechanical performance for structural use, the variation in reported values may be due to differences in mix design, curing methods, and material composition.

Epoxy resin consistently demonstrates high mechanical properties, particularly in tensile and flexural strength. The tensile strength of epoxy resin varies between 60 MPa and 125 MPa, making it one of the strongest polymer resins in this comparison (Nodehi 2022). Its flexural strength is also impressive, reaching up to 130 MPa (Verma et al. 2020). However, compressive strength values vary widely, from as low as 11 MPa to as high as 95 MPa, depending on the formulation and testing conditions (Gulabbhai et al. 2025). It's well known for its strong bonding ability and resistance to chemicals, which helps explain why it often shows higher flexural strength. This high variability suggests that epoxy resin can be modified to optimize performance for different applications. When it comes to tensile strength, epoxy composites have received a lot of attention because they hold up well under pulling forces and help prevent cracking. This makes them especially useful in areas where the material needs to stay intact under tension like in bridges, aircraft parts or protective layers.

PET is notable for its high tensile strength, reaching up to 140 MPa (Sarwar et al. 2024). However, its compressive strength is relatively moderate, ranging from 26 MPa to 80 MPa (Wattanavichien and Iwanami 2024). Similarly, PET's flexural strength values are lower, varying between 3 MPa and 10 MPa, which limits its use in applications requiring high bending resistance (Grigoriadis et al. 2023). The limited research on the tensile strength of PET-modified concrete is likely due to its common use in compression-focused applications. Compared to other polymers, PET tends to have lower tensile performance, and tensile testing in concrete research is generally more complex. However, this presents an opportunity for future studies to explore PET potential in tension-dominated structural applications. Despite these limitations, PET remains attractive for sustainable construction applications due to its lightweight nature, recyclability, and chemical resistance. Studies have demonstrated that incorporating PET as a replacement for traditional aggregates can enhance drying shrinkage resistance, abrasion resistance, and durability, making it a viable alternative in eco-friendly concrete formulations.

Vinyl ester resin provides a good balance between tensile and flexural strength, with tensile strength values ranging from 70 MPa to 84 MPa (Nodehi 2022) and flexural strength reaching up to 144 MPa (Rochman et al. 2024). It offers moderate compressive strength, typically ranging from 41 MPa to 104 MPa (Rochman et al. 2024). Vinyl ester resins are widely used in chemically aggressive environments, such as marine, industrial, and infrastructure applications, due to their superior resistance to chemical degradation and moisture absorption. However, they exhibit lower temperature resistance and mechanical stiffness compared to epoxy resins, which may limit their applicability in high-heat or high-load environments. Its high strength-to-weight ratio and excellent thermal stability, it is widely used in industries such as marine, aerospace, and construction. These qualities help materials last longer and perform better, even when exposed to heavy mechanical stress and harsh chemicals.

The selection of polymer material for construction and composite applications depends on its specific mechanical properties and environmental resistance requirements. Epoxy resin is the best choice for applications requiring high mechanical performance, particularly in high-strength structural components. Vinyl ester resin provides a balance between strength and chemical resistance, making it suitable for corrosive environments. Polyester resin is a cost-effective solution with moderate mechanical properties, making it suitable for general-purpose applications. PET-based polymer concrete presents a sustainable alternative, particularly for lightweight and eco-friendly applications, although its lower flexural and compressive strengths must be considered.

To better understand the performance differences between polyester resin, epoxy, polyethylene terephthalate (PET), and vinyl ester in polymer concrete applications, mechanical strength values from various studies are compared. In addition, Fig. 12 illustrates experimental setups for compressive strength, tensile strength, and flexural strength testing, which are commonly conducted to evaluate the structural performance of these materials

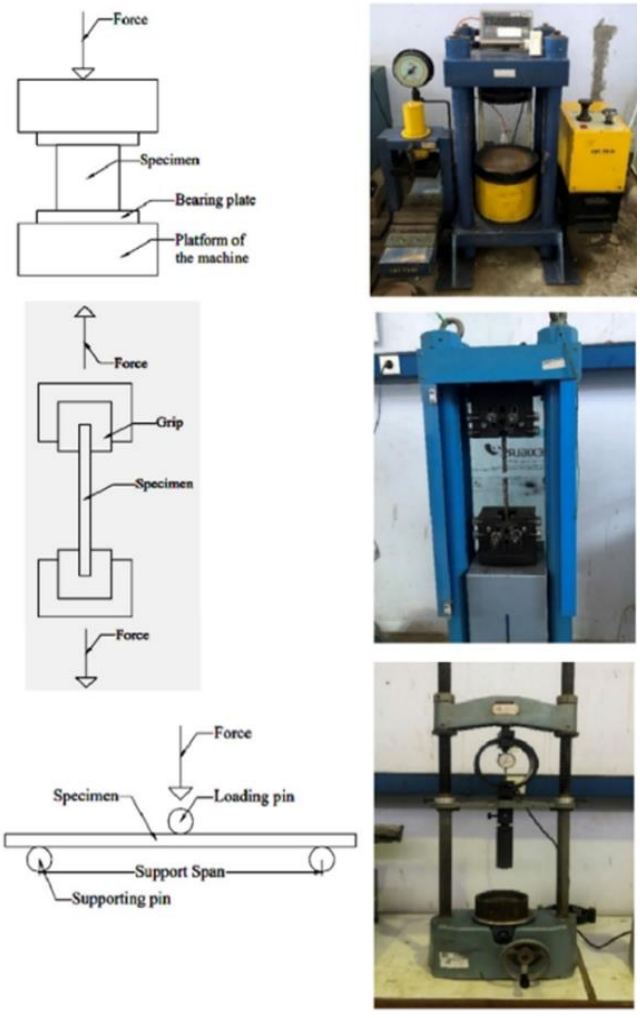

Fig. 12. Testing equipment for polymer concrete (Rochman et al. 2024).

5. Conclusions

Polymer concrete has evolved significantly since its initial development in the 1920s, with major advancements seen during its widespread adoption in the 1980s. Innovations in polymer resin formulations, fiber reinforcement technologies, and composite manufacturing have transformed polymer concrete into a high-performance material with improved mechanical strength, corrosion resistance, and long-term durability. The integration of thermosetting resins such as polyester, epoxy, vinyl ester and advanced fibers like aramid, carbon, and glass has expanded its use across infrastructure, aerospace, and industrial sectors.

This review has provided a comprehensive overview of the evolution, classification, and mechanical performance of these key polymer materials. Among them, epoxy demonstrates superior tensile and flexural strength, while polyester and polyethylene terephthalate (PET) offer notable benefits in compressive strength and sustainability. PET, in particular, shows great promise due to its potential for plastic waste reutilization, supporting both environmental and economic goals. However, research gaps persist, especially regarding the tensile behavior and long-term durability of PET in load-bearing applications.

Emerging technologies such as 3D printing have further enhanced the potential for precision-engineered polymer concrete, while the use of recycled materials and bio-based resins promotes resource efficiency and circular economy principles. Despite these advances, challenges remain, including the need for optimized curing methods, improved binder–aggregate compatibility, better workability, and standardized testing procedures. Addressing these limitations will require coordinated efforts among researchers, industry professionals, and policymakers. By overcoming current barriers, polymer concrete can achieve broader adoption and contribute meaningfully to next-generation, sustainable construction and infrastructure solutions.

Despite the comprehensive review of polymer concrete advancements, several research gaps remain, presenting opportunities for future exploration. The following recommendations outline key areas of focus to enhance the performance, sustainability, and applicability of polymer concrete in modern construction:

- The further research is needed to determine the ideal polymer-to-aggregate ratio for different types of polymer concrete. Achieving the optimal balance can help minimize material waste, enhance mechanical strength, improve workability, and increase cost-effectiveness.
- Studies should also consider the influence of microfillers and fiber reinforcements on polymer concrete formulations.

Acknowledgements

None declared.

Funding

This research was supported by Universiti Malaysia Pahang Al-Sultan Abdullah under grant number RDU230301.

Conflict of Interest

The authors declared no potential conflicts of interest with respect to the research, authorship, and/or publication of this manuscript.

Author Contributions

All of the authors made substantial contributions to conception and design, or acquisition of data, or analysis and interpretation of data; were involved in drafting the manuscript or revising it critically for important intellectual content; and gave final approval of the version to be published.

Data Availability

The datasets created and/or analyzed during the current study are not publicly available, but are available from the corresponding author upon reasonable request.

References

Akarken G, Cengiz U, Ozturk N, Balkaner C (2025). Self-cleaning superhydrophobic polyester resin production for gel coat applications. *Progress in Organic Coatings*, 198, 108884.

Alami AH, Ghani Olabi A, Alashkar A, Alasad S, Aljaghoub H, Rezk H, Abdelkareem MA (2023). Additive manufacturing in the aerospace and automotive industries: Recent trends and role in achieving sustainable development goals. *Ain Shams Engineering Journal*, 14(11), 102516.

Alhazmi H, Shah SAR, Anwar MK, Raza A, Ullah MK, Iqbal F (2021). Utilization of polymer concrete composites for a circular economy: A comparative review for assessment of recycling and waste utilization. *Polymers*, 13(13), 2135.

Ali A, Ansari AA (2013). Polymer concrete as innovative material for development of sustainable architecture. *2nd International Conference on Emerging Trends in Engineering & Technology,* Teerthanker Mahaveer University, Moradabad, India.

Aravecchia N, Bañuls-Ciscar J, Caverzan A, Ceccone G, Cuenca E, Ferrara L, Grigoriadis K, Negro P, Rodriquens M (2023). On the feasibility of using Polyester (PE) waste particles from metal coating industry as a secondary raw materials in concrete. *Cleaner Materials*, 9, 100193.

Azhdarpour AM, Nikoudel MR, Taheri M (2016). The effect of using polyethylene terephthalate particles on physical and strength-related properties of concrete; a laboratory evaluation. *Construction and Building Materials*, 109, 55–62.

Batista WGS, Costa BLS, Aum PTP, Oliveira YH, Freitas JCO (2021). Evaluation of reused polyester resin from PET bottles for application as a potential barrier material. *Journal of Petroleum Science and Engineering*, 205, 108776.

Bedi R, Chandra R, Singh SP (2013). Mechanical properties of polymer concrete. *Journal of Composites*, 2013(8), 1–12.

Benmokrane B, Ali AH, Mohamed HM, ElSafty A, Manalo A (2017). Laboratory assessment and durability performance of vinyl-ester, polyester, and epoxy glass-FRP bars for concrete structures. *Composites Part B: Engineering*, 114, 163–174.

Bulut HA, Şahin R (2017). A study on mechanical properties of polymer concrete containing electronic plastic waste. *Composite Structures*, 178, 50–62.

Byron D, Pacheli Heitman A, Neves J, de Souza PP, de Oliveira Patricio PS (2021). Evaluation of properties of polymer concrete based on epoxy resin and functionalized carbon nanotubes. *Construction and Building Materials*, 309, 125155.

Choe YA, Pak RB, Kim Sil, Ju KS (2023). Preparation and characterization of water-reducible polyester resin based on waste PET for insulation varnish. *RSC Advances*, 13(49), 34637–34645.

Fame CM, Ueda T, Ntjam Minkeng MA, Wu C (2024). Durability of epoxy and vinyl ester polymers in wet, seawater, and seawater sea sand concrete environments: Molecular dynamics simulations. *Construction and Building Materials*, 451, 138645.

Fei M, Luo C, Zheng X, Fu T, Ling K, Chen H, Liu W, Qiu R (2024). High-performance pervious concrete using cost-effective modified vinyl ester as binder. *Construction and Building Materials*, 414, 134908.

Feldman D (2008). Polymer history. *Designed Monomers and Polymers*, 11, 1–15.

Fowler DW (1999). Polymers in concrete: a vision for the 21st century. *Cement and Concrete Composites*, 21(5–6), 449–452.

Godara SS, Yadav A, Goswami B, Rana RS (2021). Review on history and characterization of polymer composite materials. *Materials Today: Proceedings*, 44(Part 1), 2674–2677.

Grigoriadis K, Bañuls-Ciscar J, Caverzan A, Negro P, Senaldi C, Ceccone G (2023). Use of irradiated PET plastic waste for partially replacing cement in concrete? *Waste Management*, 170, 193–203.

Gulabbhai DP, Kruger D, Hira MK (2025). Testing the performance of vinyl ester and polyester polymer concrete following exposure to artificially induced climatic environments. *Springer Proceedings in Materials*, 61, 539–546.

Heidari-Rarani M, Asdollah-Tabar M, Mirkhalaf M (2023). Experimental investigation and micromechanics-based damage modeling of tensile failure of polymer concrete reinforced with recycled PET bottles. *Engineering Failure Analysis*, 148, 107197.

Khallouqi A, Halimi A, El rhazouani O (2024). Evaluating polyester resin as a viable substitute for PMMA in computed tomography dosimetry phantoms. *Nuclear Engineering and Technology*, 56(9), 3758–3763.

Koirala S, Hirachan B, Chhetri SG, Gyawali TR (2025). Utilizing residual waste particles from polyethylene terephthalate (PET) waste pellet production in cement mortar. *International Journal of Sustainable Engineering*, 18(1), 1–13.

Kumar R (2016). A review on epoxy and polyester based polymer concrete and exploration of polyfurfuryl alcohol as polymer concrete. *Journal of Polymers*, 2016, 1–13.

Luo T, Zhao Y, Fu K, Cui X, Chen B (2024). High-efficiency manufacturing of epoxy resins through two-point initiation of frontal polymerization. *Chemical Engineering Journal*, 496, 154148.

Martínez-López Á, Martínez-Barrera G, Vigueras-Santiago E, Martínez-López M, Gencel O (2022). Mechanical improvement of polymer concrete by using aged polyester resin, nanosilica and gamma rays. *Journal of Building Engineering*, 58, 105083.

Mehdar YTH (2024). Investigating the Impact of temperature and storage time on antimony release from polyethylene terephthalate (PET) plastic used for bottled drinking water. *Desalination and Water Treatment*, 319, 100474.

Nodehi M (2022). Epoxy, polyester and vinyl ester based polymer concrete: a review. *Innovative Infrastructure Solutions*, 7, 64.

Oladele IO, Onuh LN, Siengchin S, Sanjay MR, Adelani SO (2023). Modern applications of polymer composites in structural industries: a review of philosophies, product development, and graphical applications. *Applied Science and Engineering Progress*, 17(1), 6884.

Pacheco-Torgal F, Ding Y, Jalali S (2012). Properties and durability of concrete containing polymeric wastes (tyre rubber and polyethylene terephthalate bottles): An overview. *Construction and Building Materials*, 30, 714–724.

Rayati S, Ghadami A, Ehsani M, Hasanbeik NY, Ghafourihayeasl E, Rahdar A, Fathi-karkan S, Pandey S (2025). Enhanced mechanical and thermal properties of epoxy vinyl ester nanocomposites through hybridization with functionalized graphene oxide and nanoglass flakes. *Inorganic Chemistry Communications*, 172, 113642.

Rebeiz KS (1996). Precast use of polymer concrete using unsaturated polyester resin based on recycled PET waste. *Construction and Building Materials*, 10(3), 215–220.

Rochman T, Sumardi Susilo SH, Wardhana HA (2024). Vinyl-ester-based polymer concrete incorporating high volume fly ash under tensile, compressive, and flexural loads. *Journal of King Saud University - Engineering Sciences*, 36(3), 153–163.

Rubeš D, Vinklárek J, Podzimek Š, Honzíček J (2024). Bio-based unsaturated polyester resin from post-consumer PET. *RSC Advances*, 14(12), 8536–8547.

Safinia S, Alkalbani A (2016). Use of recycled plastic water bottles in concrete blocks. *Procedia Engineering*, 164, 214–221.

Salami BA, Bahraq AA, Haq MM ul, Ojelade OA, Taiwo R, Wahab S, Adewumi AA, Ibrahim M (2024). Polymer-enhanced concrete: A comprehensive review of innovations and pathways for resilient and sustainable materials. *Next Materials*, 4, 100225.

Sarwar S, Molla SR, Das S, Tammim L, Ahmed FF, Akter S (2024). Algal deterioration of PET (polyethylene terephthalate) plastic bottle in combination with physical and chemical pretreatments: A macrocosm study. *Environmental and Sustainability Indicators*, 21, 100329.

Seewoo BJ, Wong EVS, Mulders YR, Goodes LM, Eroglu E, Brunner M, Gozt A, Toshniwal P, Symeonides C, Dunlop SA (2024). Impacts associated with the plastic polymers polycarbonate, polystyrene, polyvinyl chloride, and polybutadiene across their life cycle: A review. *Heliyon*, *10*(12), e32912.

Silva DA, Betioli AM, Gleize PJP, Roman HR, Gómez LA, Ribeiro JLD (2005). Degradation of recycled PET fibers in Portland cement-based materials. *Cement and Concrete Research*, 35(9), 1741–1746.

Soni V, Dinh DA, Poonia K, Kumar R, Singh P, Ponnusamy VK, Selvasembian R, Singh A, Chaudhary V, Thakur S, Nguyen LH, Phan Thi LA, Nguyen VH, Raizada P (2024). Upcycling of polyethylene terephthalate (PET) plastic wastes into carbon-based nanomaterials: Current status and future perspectives. In *European Polymer Journal,* 215, 113249.

Surucu O (2025). Electrochemical analysis of PET microplastics and detection of elements in PET bottles. *Microchemical Journal*, 208, 112422.

Suyambulingam I, Sahayaraj Arockiasamy F, Divakaran D, Rangappa SM, Siengchin S (2025). Introduction to polymer composites-Historical aspects and building blocks. In: Sustainable Fillers/Plasticizers for Polymer Composites. Woodhead Publishing, Elsevier.

Tabatabaeian M, Khaloo A, Khaloo H (2019). An innovative high performance pervious concrete with polyester and epoxy resins. *Construction and Building Materials*, 228, 116820.

Thomason J, Xypolias G (2024). Investigation of the effects of scale and cure environment on the properties of vinyl ester polymer. *Polymer*, 307, 127344.

Tsyklinskaya AM, Polivanovskaia DA, Grammatikova NE, Zhavoronok ES, Birin KP, Senchikhin IN (2024). Biocidal polymer coatings based on porphyrin-modified epoxy-amine networks. *Reactive and Functional Polymers*, 205, 106099.

Umasabor RI, Daniel SC (2020). The effect of using polyethylene terephthalate as an additive on the flexural and compressive strength of concrete. *Heliyon,* 6(8), e04700.

van Zyl FW, Kruger D (2025). The use of polymer concrete as a cost-effective and durable alternative for rapid pothole repair in asphalt surfaces. *Springer Proceedings in Materials*, 61, 374–383.

Venu H, Anand Chairman C, Ravichandran M, Sieh Kiong T, Kannan S, Razali NM, Fouly A (2024). Analysis of mechanical properties of basalt fabric reinforced fly ash filled vinyl ester composites using multi criteria decision making technique. *Thermal Science and Engineering Progress*, 54, 102869.

Verma C, Olasunkanmi LO, Akpan ED, Quraishi MA, Dagdag O, El Gouri M, Sherif ESM, Ebenso EE (2020). Epoxy resins as anticorrosive polymeric materials: A review. *Reactive and Functional Polymers*, 156, 104741.

Wang CY, Chu HY, Wang CC (2024). Converting waste PET plastics to high value-added MOFs-based functional materials: A state of the art review. *Coordination Chemistry Reviews*, 518, 216106.

Wang RM, Zheng SR, Zheng YP (2011). Polymer Matrix Composites and Technology. Woodhead Publishing, Elsevier.

Wang TS, Parng JK, Shau MD (1999). The synthesis and properties of new epoxy resin containing phosphorus and nitrogen groups for flame retardancy. *Journal of Applied Polymer Science*, 74(2), 413–421.

Wang Z, Phua ZH, Chan WP, Lisak G (2024). Evaluating fresh and hardened properties of mortar composite with different types of modified polyethylene terephthalate (PET) materials as additives: Modification effects, surface properties, shape factors. *Chemosphere*, 367, 143567.

Wattanavichien P, Iwanami M (2024). Investigation of the mechanical, microstructure, and durability properties of concrete with fine uniform and non-uniform polyethylene terephthalate (PET) aggregates. *Cleaner Materials*, 13, 100267.

Waysal S, Patil YD, Dholkiya BZ, Bhoi AM (2023). Employing copper slag and pet polymer in self-compacting concrete. *Materials Today: Proceedings*, 93, 515–521.

Yılmaz Y, Nayır S (2024). Machine learning based prediction of compressive and flexural strength of recycled plastic waste aggregate concrete. *Structures*, 69, 107363.

Zhang K, Fu P, Wang Y, Chang Q, Yang W, You Z, Huang J, Nie X, Chen J (2024). Tung oil-based modifier strengthening and toughening epoxy resin by sacrificial bond. *Industrial Crops and Products*, 222, 120116.